Synthesis and Characterization of Nanostructured Carbon Supported Pt-based Electrocatalysts

by

Xi Geng

A Thesis

Submitted to the Faculty

of the

WORCESTER POLYTECHNIC INSTITUTE

In partial fulfillment of the requirements for the

Degree of Master of Science

in

Materials Science and Engineering

January 2012

Approved by:

ABSTRACT

Fuel cell, as an alternative green power source for automobiles and portable electronics, has attracted worldwide attention due to its desirable properties such as high energy density and low greenhouse gas emission. Despite great progress in the past decades, several challenges still remain as obstacles for the large-scale commercialization. Among them, the high cost of Pt-based electrode material is considered as a major barrier, while the life span or stability of electrode catalysts is another concern since the electrocatalysts can be easily poisoned during the fuel cell operation. In order to overcome these issues, nanostructured carbon materials, especially carbon nanotubes (CNTs), are studied as catalyst support. In addition, recent research also suggests that the coupling of a second metal element with Pt can effectively protect the electrocatalysts from being poisoned and thus improve their long-term durability.

The objective of the present work was to demonstrate an efficient synthetic method for the preparation of CNTs supported binary PtM (M=Ru, Sn) electrocatalysts. In this project, a polymer wrapping technique along with an in-situ polyol reduction strategy was adopted to decorate well-dispersed binary PtM nanoparticles on the surface of modified-CNTs. The unique nanostructures as well as the excellent catalytic activities of the as-prepared nanohybirds were investigated through a diversity of physiochemical and electrochemical characterization techniques. This fabrication method provided a simple and convenient route to assemble Pt-based catalyst on carbon substrates, which is useful for the further development of high-performance fuel cell catalysts.

ACKNOWLEDGEMENTS

First and foremost, I would like to express my sincere appreciation and gratitude to my advisor, Professor Jianyu Liang. Her enthusiasm to research and dedication to work inspire me throughout two years of graduate study in WPI.

I cordially thank my committee members, Professor Richard D. Sisson, Jr. and Professor Ravindra Datta for sharing their insightful visions on my research projects during the past two and a half academic years.

I also would like to acknowledge Dr. Boquan Li for his assistance on lab work and Ms. Rita Shilansky for her help in our daily life.

My sincere thanks also goes to my friends and colleagues in the Materials Science and Engineering program who make my years at WPI a joyful experience.

Finally, I would like to extend my deepest gratitude to my family for their continuous encouragement and unconditional support.

TABLE OF CONTENTS

CHAPTER I INTRODUCTION

Rising energy demands, depletion of fossil fuel, and deteriorate environmental pollution has urged mankind to pursue highly-efficient energy conversion devices with low emission. Fuel cell has attracted much attention as a green power supply for automobiles and portable electronic devices due to the high energy density, ease of handling and low operation temperature [1-5].

In the past decades, great achievements have been made to advance the fuel cell technology. Nevertheless, the commercialization of fuel cells is still hindered by the high cost of Platinum-based electrocatalyst [6]. According to the US Department of Energy, the amount of Pt should be reduced to below 0.03mg cm^{-2} in a single stack fuel cell to meet the requirement for the applications in automobile [7]. Besides, Pt is also known to be poisoned by the adsorbed intermediates such as CO during the fuel cell operation, which may lead to severe long-term performance degradation [8, 9].

To increase the utilization efficiency of noble metal catalysts and inhibit the CO poisoning effect, recent research work has been directed towards two major aspects (i) exploiting nanostructured carbon substrates for the high dispersion of nano-size Pt catalysts and (ii) alloying Pt with another metal to mitigate catalyst poisoning

Research Objectives

The goal of this research work is to develop nanocomposite catalysts with high catalytic activity and good stability for fuel cells. During graduate study, my research primarily focuses on the synthesis and characterization of polyelectrolyte modified carbon nanotubes (CNT) supported Pt-based bimetallic electrocatalysts.

Thesis Organization

The main content of this thesis is divided into five sections. Motivations and objective are stated in the first chapter. Recent progress on the synthesis and characterization of nanostructured carbon supported Pt-based electrocatalyst is comprehensively reviewed in the Chapter 2. In addition, the influences of carbon

support and binary catalysts on the electrocatalytic performance are also reviewed in Chapter 2. In the third chapter, the experimental and characterization techniques are described. Two manuscripts submitted to peer-reviewed journals in the field of materials science and electrochemistry are presented in Chapter 4. Finally, conclusions from the current experimental results and a brief introduction of future perspectives towards the development of high-performance electrocatalysts are included in the last chapter.

Reference

[1] Appleby, A.J.; Foulkes, F.R.; Fuel Cell Handbook, Van Norstand Reinhold, New York, NY, **1989**.

[2] Cao, L.; Sun, G., Li, H.; Xin, Q. Electrochem. Commun. **2007**, *9*, 2541-2546.

[3] Godoi, D.R.M.; Perez, J.; Villullas, H.M. *J. Power Sources* **2010**, *195*, 3394-3401

[4] Ocampo, A.L.; Miranda-Hernández, M.; Morgado, J.; Montoya, J.A.; Sebastian, P.J. *J. Power. Sources* **2006**, *160*, 915-924.

[5] Paoletti, C.; Cemmia, A.; Leonardo Giorgi, L.; Giorgi, R.; Pilloni, L.; Serra, E.; Pasquali, M. *J. Power Sources* **2008**, *183*, 84-91.

[6] Litster, S.; Mclean, G. *J. Power Sources* **2004**, *130*, 61-76.

[7] Yu, X.; Ye, S. *J. Power Sources* **2007**, *172*, 133-144.

[8] Gottesfeld, S.; Pafford, J. *J. Electrochem. Soc.* **1988**, *135*, 2651-2652.

[9] Beden, B.; Lamy, C.; Bewick, A.; Kumimatsu, K.; *J Electroanal. Chem.* **1981**, *121*, 343-347.

CHAPTER II LITERATURE REVIEW

2.1 Introduction

2.1.1 Fundamentals and operating principles of Fuel Cell

In principle, fuel cell is an electrochemical device which is fed by small molecular fuels at the anode, and oxygen at the cathode [1]. So far, various types of fuel cells including hydrogen-fuelled proton exchange membrane fuel cells (PEMFCs) [2], direct methanol fuel cells (DMFCs) [3,4], direct ethanol fuel cells (DEFCs) [5,6], etc., have been developed. During the operation, fuel such as hydrogen or methanol is oxidized at the anode and both the protons and electrons are released. The generated protons will pass through a thin layer of proton exchange membrane (PEM) and react with oxygen in the cathode, whereas the electrons are blocked by PEM and travel through the external electric circuit to provide energy output (Fig. 2.1).

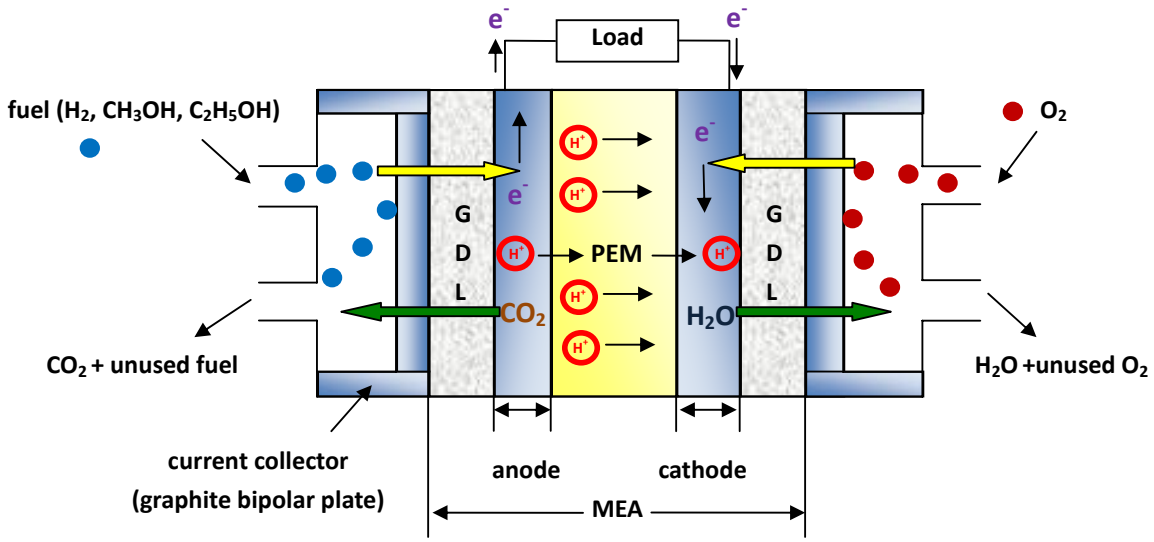

Fig. 2.1 Schematic illustration of fuel cell operation

2.1.2 The Membrane-electrode-assembly

As shown in the Fig.1, the key component of a single stack fuel cell is a multilayered membrane-electrode-assembly (MEA) consisting of a proton exchange membrane (PEM), gas diffusion layers (GDL) and catalyst layers (anode and cathode). Each component is normally fabricated individually and then assembled together by

hot pressing technique.

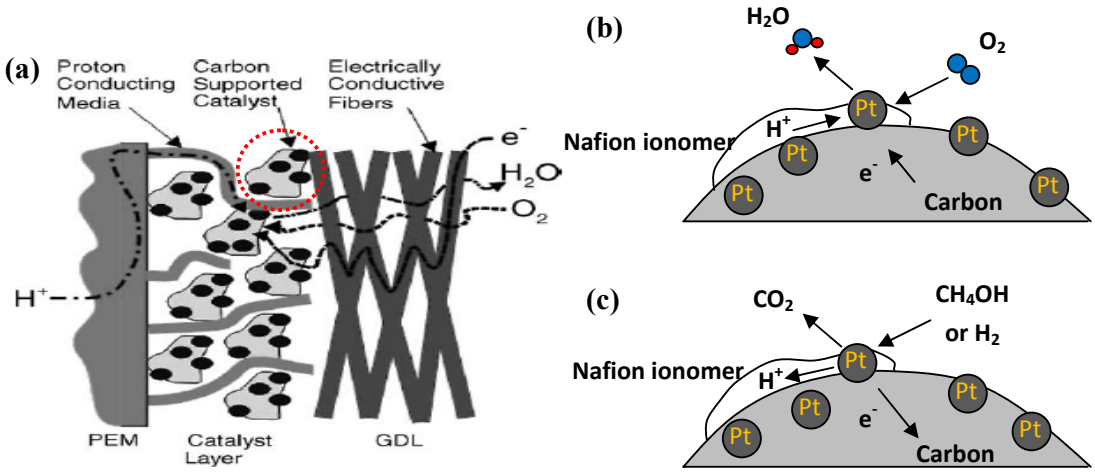

Fig. 2.2 (a)Transport of protons, electrons and mass in a MEA of PEMFCs [1] catalyst-electrolyte-reactant triple phase boundaries for (b)cathode and (c)anode [7].

A functional MEA should correctly balance three major transport processes as shown in Fig.2.2. The PEM provides medium for protons to pass through but prevents the crossover of electrons and reactants. The GDLs are typically constructed using porous carbon matrix, with a thickness in the range of 100-300μm. GDLs ensure the effective diffusion of reactants and products into and out of the catalyst layer and also serve as electron transfer channels. Catalyst layer, also referred as the active layer, is where the following half cell reactions take place:

Anode reaction: $H_2 \Leftrightarrow 2H^+ + 2e^-$ (for Hydrogen-fuelled PEMFC) (1)

$CH_3OH + H_2O \Leftrightarrow CO_2 + 6H^+ + 6e^-$ (for DMFC) (2)

$C_2H_5OH + 3H_2O \Leftrightarrow 2CO_2 + 12H^+ + 12e^-$ (for DEFC) (3)

Cathode reaction: $nO_2 + 4nH^+ + 4ne^- \Leftrightarrow 2nH_2O$ (4)

The catalyst layers need to be designed to facilitate high rate of electrochemical reactions and minimize the catalyst loading for desirable power output. The general criteria for catalyst layer include large triple-phase interface, continuous proton and electron transfer passages and facile mass transport channels. Catalyst layer can be fabricated by applying the catalyst ink onto GDLs or directly coating the catalyst

slurry onto proton conducing membrane [7]. In both approaches, the objective is to place the catalyst particles within close proximity of the membrane. The catalyst ink is conventionally prepared by mixing carbon supported Pt or Pt-based alloy with Nafion ionomer as binder and proton conducting media.

2.1.3 Nano-structured carbon supported Pt-based alloy electrocatalysts

To date, platinum is recognized as the most active catalyst for electrooxidation of H_2 and alcohol. However, high cost of Pt still restricts the large-scale commercialization of fuel cells. To increase Pt utilization, one practical strategy is to explore novel catalyst support for high dispersion of nano-scale Pt particles [1].

In recent decades, a series of new nanostructured carbon materials such as carbon nano tubes (CNTs) [8, 9, 10], carbon nano fibers (CNFs) [11], carbon aero gel [12] and mesoporous carbon [4，13] were extensively investigated as promising catalyst support, among which carbon nanotubes (CNTs) are the most well-known candidates. Since the discovery of carbon nanotubes (CNTs) in 1991 [14], enormous efforts have been dedicated to the studies on the fabrication and application of these new carbon allotropes. Due to the characteristics such as hollow geometric structure, large specific surface areas, high electronic conductivity and good chemical stability, CNTs has intrigued much attention as the support materials of Pt-based catalyst [15, 16].

Besides the high cost issue, it is also noted that Pt is easily poisoned by the impurity CO or carbonaceous species produced during the electrocatalysis of small organic molecules [17, 18]. This negative effect will substantially reduces the catalytic activity and diminish the long-term durability of Pt. Fortunately, previous research has demonstrated that this poisoning phenomenon could be significantly mitigated by the introduction of the second metal element such as Ru or Sn into the electrocatalyst system [19, 20]. Thus, a lot of research work has now been conducted on the development of nanostructured carbon supported Pt or Pt alloy catalyst.

In the following sections, a comprehensive review of current research activities concentrated on the nanocarbon supported Pt-based nanocomposites is provided. The synthetic approaches that have been exploited to achieve Pt/nanocarbon hybrid are elaborated in the section 2.2. An overview of conventional physicochemical and

electrochemical characterization techniques is given in 2.3. Following is the discussion that involves the influence of carbon support on the morphology and catalytic performance of novel Pt/C nanomaterials. In section 2.5, the promoting effect of secondary metal element, Ru and Sn in particular, on the catalytic performance of Pt-based catalyst is briefly covered.

2.2 Synthetic methods for nanocarbon supported Pt-based electrocatalysts

Table 2.1 Comparison of primary techniques for the synthesis of Pt/C catalysts

Techniques	***Experimental condition***	***Features***	
		Advantages	***Disadvantages***
Electroless [19, 22, 66]	chemical reduction using reducing agent or under H_2 atmosphere	facile and straightforward small particle size	Time consuming impurity
Electrochemical [120, 124]	electrochemical reduction by applying potentiostatic or galvanostatic excitation	rapid reaction rate good loading control diverse morphology	large particle size broad size distribution
Irradiation-assisted [64,105,144]	synthesis under irradiation source such as microwave, Co^{60} (γ radiation), ultraviolet and ultrasonication	uniform size high dispersion pure novel morphology	need specific irradiation reactor
PVD [12,153]	evaporation of target metal via plasma, electron or ion beam bombard	uniform size precise loading control high Pt utilization	loose adhesion between Pt and carbon substrate; high cost of instrumentation

Pt NPs can be immobilized onto the nanocarbon to construct novel hybrid electrocatalyst. As clearly seen from a large number of publications, great efforts have been made on the fabrication of nanostructured carbon supported Pt-based catalyst. So far, a diversity of synthetic strategies can be generally categorized as follows: electroless preparation [8-11, 16, 21-119], electrochemical synthesis [15, 120-133],

irradiation assisted fabrication [64, 105, 112, 134-152], and physical vapor deposition [12, 153-166] (Fig.2.3). A comparison of different fabrication techniques is given in Table 2.1.

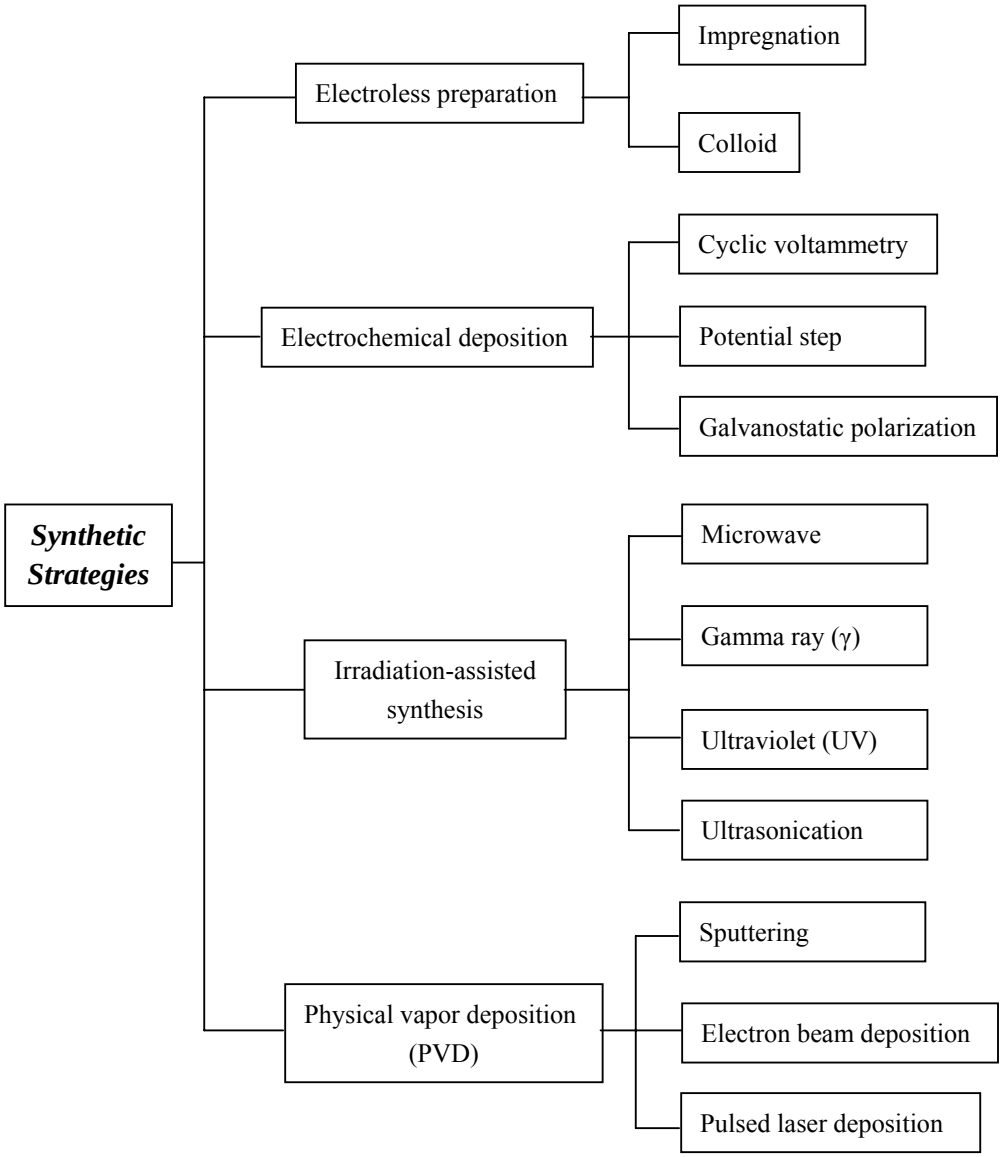

Fig. 2.3 Synthetic strategies for the preparation of Pt/C electrocatalyst

2.2.1 Electroless preparation

Electroless preparation including impregnation and colloidal approaches are cost-effective and straightforward techniques (Fig. 2.4).

2.2.1.1 Impregnation method [21-25]

In a conventional two-step impregnation route reported by Shao et al. [22], CNTs was first mixed with Pt precursor (H_2PtCl_6) under vigorous stirring. The obtained

mixture was then incubated at 100°C overnight, followed by reducing the sample in a flow of hydrogen gas at 300°C for 2 hours.

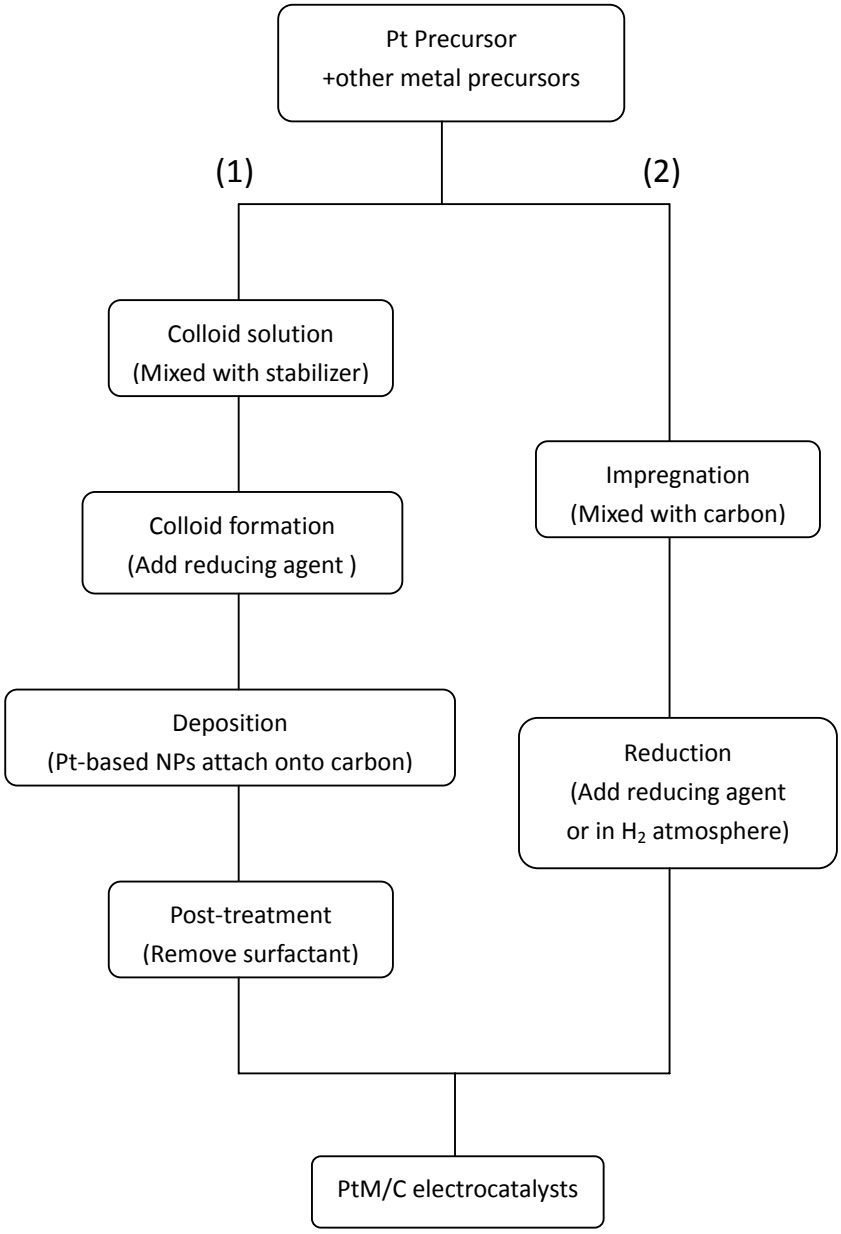

Fig. 2.4 Electroless preparation of carbon supported Pt-based electrocatalyst (1) colloidal method (2) impregnation method

A few studies have shown that the morphology and the electrocatalytic performance of the catalyst are strongly dependent on the preparation method and reducing agents in the electroless approach (Table 2.2). Up to date, a variety of

reducing agents have been employed for the synthesis of Pt nanomaterials, including H_2 [22,13,26-38], sodium borohydride ($NaBH_4$) [8, 9, 16, 21, 44-51, 52-59], ethylene glycol (EG) [19,60-94,134,136,138], formaldehyde (HCHO) [94-96], formic acid (HCOOH) [98-100], glycerol [101], N,N-dimethylformamide (DMF)[102], glucose [103,104], hydrazine[11, 105, 106], sodium dodecyl sulfate (SDS) [107, 108], ascorbic acid (AA) [86,109], glacical acetic acid [109, 110], etc. Among them, $NaBH_4$ is most commonly used for the synthesis of carbon supported Pt and Pt-based PtRu binary catalysts according to the following reactions:

$$2PtCl_6^{2-} + BH_4^- + 4H_2O \rightarrow 2Pt + B(OH)_4^- + 8H^+ + 12Cl^- \quad (5)$$

$$8Ru^{3+} + 3BH_4^- + 12H_2O \rightarrow 8Ru + 3B(OH)_4^- + 24H^+ \quad (6)$$

Table 2.2 Comparison on preparation method for the synthesis of PtRu/CNTs [112].

Preparation method	Morphology			Performance on methanol oxidation
	Size	Density	Dispersion	
Modified EG	○	○	○	○
EG	○	○	△	△
H_2	○	△	○	△
HCOOH	×	○	×	×
HCHO	×	○	×	×
$NaBH_4$	△	○	×	△
Raney Ni	△	△	△	△
Electrodeposition	×	○	×	△

○: Good △: Fair ×: Poor

EG polyol reduction method has also been widely used for the preparation of noble metal NPs, owing to the multifunction of EG simultaneously serving as solvent, reducing agent and stabilizer. The reaction mechanism between EG and Pt/Ru metal ions can be shown as equation (7-9). For this reaction pathway to take place, the –OH groups of EG interact with Pt/Ru precursor ions, resulting in the oxidation of hydroxyl group to aldehydes, glycolic and oxalic acid [112].

$$CH_2OH - CH_2OH \rightarrow CH_3CHO + H_2O \quad (7)$$

$$4CH_3CHO + Pt^{4+} \rightarrow Pt + 4H^+ + 2CH_3COCOCH_3 \quad (8)$$

$$6CH_3CHO + 2Ru^{3+} \rightarrow 2Ru + 6H^+ + 3CH_3COCOCH_3 \quad (9)$$

One research group reported the synthesis of Pt/CNT composites using either HCHO or EG as reduction agent [94]. Morphology study showed that Pt nanoclusters prepared by HCHO method have a strong tendency to form agglomeration (Fig. 2.5). In contrast, Pt NPs prepared by EG are in the range of 2 to 5nm with fairly narrow distribution. Similar results have been reported by Chien et al. [113], who found modified EG the most effective technique for the preparation of PtRu/CNTs electrocatalyst towards methanol oxidation (table 2.2).

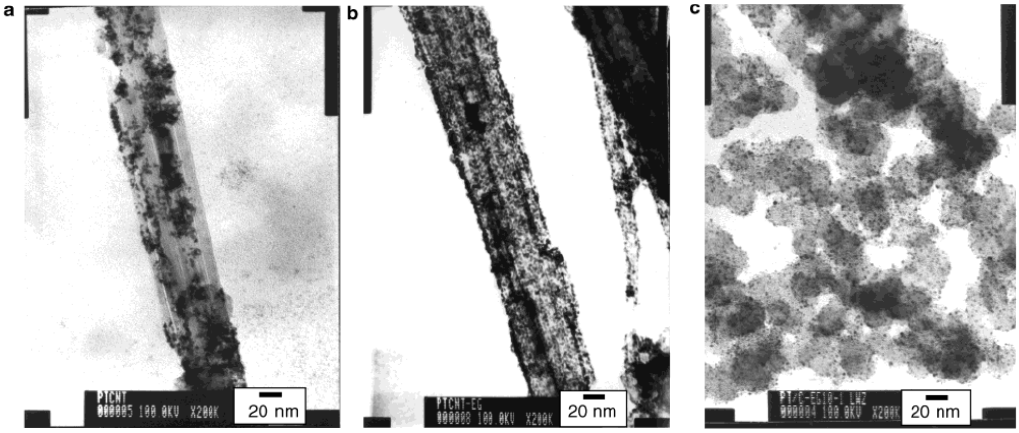

Fig. 2.5 TEM images of (a) Pt/MWCNTs (prepared by HCHO) (b) Pt/MWCNTs (prepared by EG) (c) Pt/XC-72 (prepared by EG) [94]

Even though impregnation method is very popular for preparing nanocomposite, one major drawback is the difficulty to precisely control the particle size and distribution. However, a highly dispersed Pt based NPs can still be obtained in some cases using appropriate synthetic strategies [114].

For example, a modified impregnation method for the synthesis of PtRu/CNTs was presented by Shao et al. [115]. Prior to the deposition of Pt NPs, the CNTs was first oxidized in a mixture of 8M H_2SO_4/8M HNO_3. After adding H_2PtCl_6 and $RuCl_3$ precursors, the PH value of the solution was adjusted to 12 with $NH_3 \cdot H_2O$. Under such circumstance, the PtRu precursors were co-precipitated and attached onto the CNTs in the form of $(NH_4)_2PtCl_6$ and $Ru(OH)_3$. By introducing this intermediate step, severe aggregation of PtRu NPs is suppressed during the reduction process.

In addition, a surfactant-regulated preparation technique was developed by Lee et al. to attach Pt NPs on CNTs in the presence of sodium dodecyl sulphate (SDS)

micelle [108]. In a typical experiment, CNTs was first dispersed in a SDS aqueous solution and refluxed in an oil bath to release the 1-dodecanol from the SDS amphiphiles. During the deposition procedure, H_2PtCl_6 was slowly reduced to ultrafine Pt NPs (1-3nm) by the released 1-dodecanol in the micellar core, while 1-dodecanol was further oxidized and esterified to stabilize the Pt NPs on CNTs.

2.2.1.2 Colloidal method

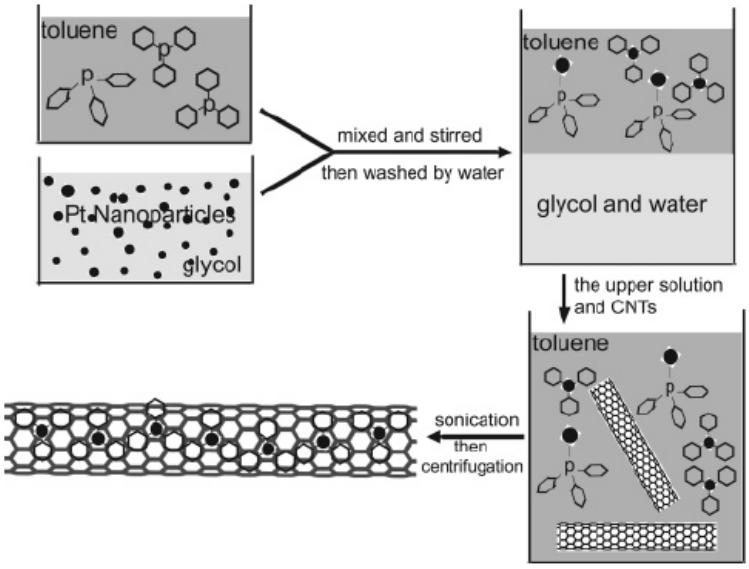

Fig. 2.6 Schematic illustration of synthesis of Pt-PPh_3/CNTs nanocomposite [66].

Colloidal approach [16, 19, 66, 108, 117-119] as an alternative electroless method, usually involves the preparation and stabilization of Pt colloid with ligand or capping reagent at the initial step. For example, Mu el al. reported a novel process to prepare well-dispersed Pt NPs on CNTs [66]. As shown in the schematics (Fig.2.6), Pt colloid was first prepared using EG method and stabilized by triphenylphosphine (PPh_3) in the toluene solution. Then the functionalized Pt NPs was transferred to the CNTs suspension and uniformly decorated onto the CNTs surface with the aid of ultrasonication. Unlike impregnation method, tedious post heat-treatment is often required to remove the insulating surfactant such as PPh_3 interlinker coated on the Pt/CNTs.

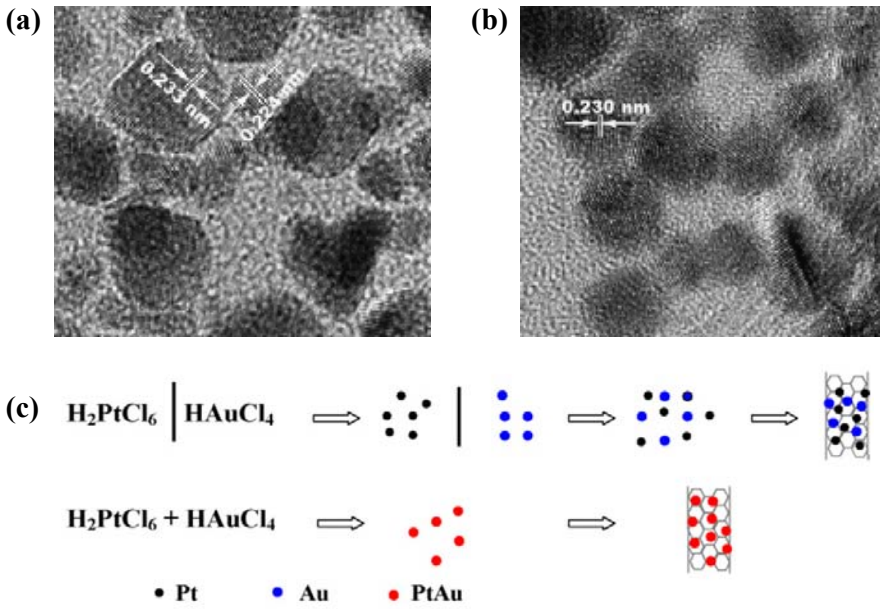

Fig. 2.7 HRTEM images of (a) Pt/Au colloid (b) PtAu alloy colloid and (c) Schematic illustration for preparation of Pt/Au/CNTs and PtAu/CNTs catalysts [118].

In another example, bimetallic alloy-like PtAu/CNTs and separate-phase Pt/Au/CNTs were fabricated using colloidal technique [118]. As illustrated in Fig., both PtAu nanoalloy and Pt/Au NPs were prepared using KBH_4 and trisodium citrate as the reducing and stabilizing agents, respectively. The particles with the d-spacing of 0.233 nm and 0.224 nm are ascribed to Au (1 1 1) and Pt (1 1 1), indicating that Pt NPs were separated by the adjacent Au NPs (Fig.2.7 (a)). In contrast, the narrowly distributed NPs with interplanar distance of 0.230nm was shown on Fig.2.7(b), corresponding to PtAu nanoalloy. In the next step, the NPs were deposited onto CNTs by combining an aqueous solution of metal colloid with CNT suspension (Fig.2.7 (c)).

2.2.2 Electrochemical deposition

Electrochemical deposition is a practical and powerful method for preparing a broad range of Pt-based electrocatalyst. Unlike the time-consuming chemical reduction process, the Pt NPs could be formed very fast upon electrodeposition of metal salt, and thus exhibiting higher purity and good adhesion to the CNT surface [121]. Additionally, one another advantage of electrodeposition is its ease in controlling the composition and catalyst loading by varying the reaction condition, such as concentration, voltage, current density and duration time, etc. The typical

experimental setup involves the use of a three-electrode electrochemical cell, where the electrolyte serves as the Pt source and nanocarbon coated glassy carbon or graphite plate serves as the working electrode. So far, various electrochemical techniques including cyclic voltammetry [120, 126], potential step [122,125,129-131], galvanostatic pulse [123, 133], chronoamperometric (potentiostatic) [124, 127], electrophoresis [132], etc. have been adopted for the fabrication of Pt-based electrocatalyst (Fig.2.8).

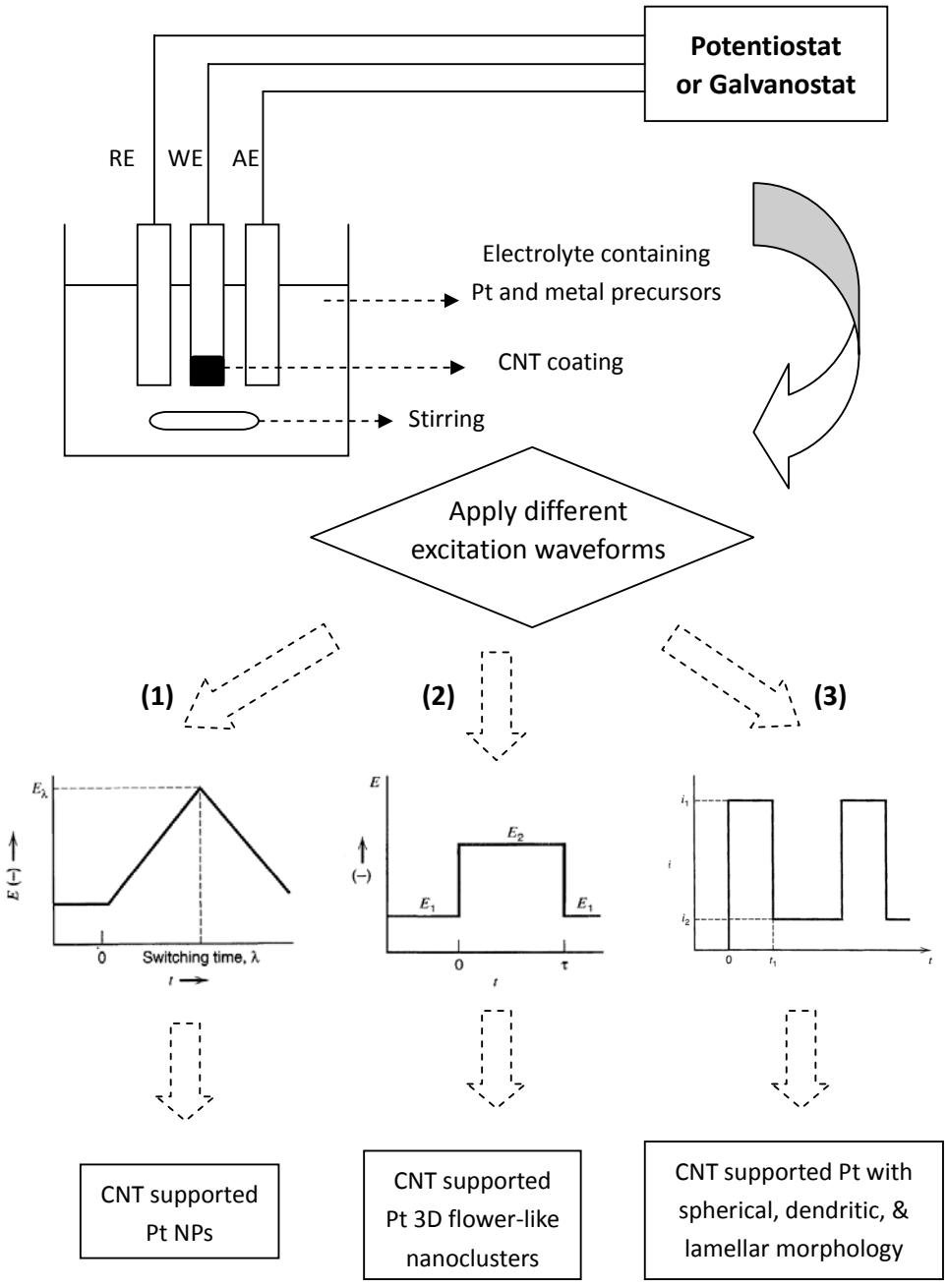

Fig. 2.8 Schematics illustration of electrochemical synthesis of Pt/CNT via (1) cyclic voltammetry (2) potential step (3) galvanostatic pulse technique. (WE, AE, RE denoted as working, auxiliary and reference electrode, respectively)

Among a variety of electrodeposition techniques, cyclic voltammetry (CV) is most widely used to prepare Pt/CNTs nanocomposite. For example, Zhao et al. developed a three-step CV process to deposit Pt NPs on MWCNTs [120]. The initial step involved the generation of functional groups on MWCNTs through electrochemical treatment, which was followed by performing CV in a solution containing 2M K_2PtCl_4 (II) and 0.1 M K_2SO_4. The formed Pt(IV) complex intermediate was eventually reduced to Pt(0) by cycling the CNT-coated electrode in a 0.1 M H_2SO_4 solution. The author pointed out that high dispersion of Pt NPs on MWCNTs could be achieved with the increase of the cycle numbers.

The potential step approach has also been employed to deposit Pt nanoparticles onto the tips and sidewalls of MWCNTs. In a typical experiment conducted by Cui et al. [122], the loosely grown MWCNTs were first attached onto the glassy carbon electrode using conductive silver paint. Then the electrodeposition of Pt NPs was carried out by applying potential steps from 0.5 to -0.7V (vs Ag/AgCl) with a three-electrode arrangement. The potential step width and cycle numbers was altered to control the morphology of products. The authors demonstrated that repeated potential steps (200 times) with fixed width (10s) could result in snowflake-like Pt NPs, which displayed large specific surface area and high electrocatalytic activity toward oxygen reduction reaction (ORR). In another example, the 3D flowerlike Pt nano-clusters were deposited on CNTs using a three-step electrochemical process [125]. It was interesting to observe that the morphology of the resulting Pt NPs was closely associated with the electrodeposition method. By applying potential-step, flowerlike Pt nanoclusters ranging from 1 to 20 nm was obtained, whereas the cyclic voltammetry technique normally produced finely dispersed Pt NPs. Furthermore, the authors claimed that the Pt NPs prepared with a pulse width of 0.001s exhibited the largest electrochemical surface area, and accordingly the highest electrocatalytic activity.

Galvanostatic polarization, as another electrochemical synthetic approach has been described by Paoletti et al. [123]. Through single and multiple pulse galvanostatic polarizations in 1M sulphuric acid + 5mM hexachloroplatinic acid solution, nanostructured Pt electrocatalyst with uniform distribution was deposited onto carbon black and CNTs. As shown in the SEM images (Fig.2.9), the product morphology was highly dependent on the electrodeposition parameters. Three distinct shapes including spherical, dendritic and lamellar structures were achieved simply by changing the charge density values. It was also revealed that the morphology of NPs had significant influence on the catalytic activity towards methanol oxidation, among which globular shaped particles exhibited best electrocatalytic performance.

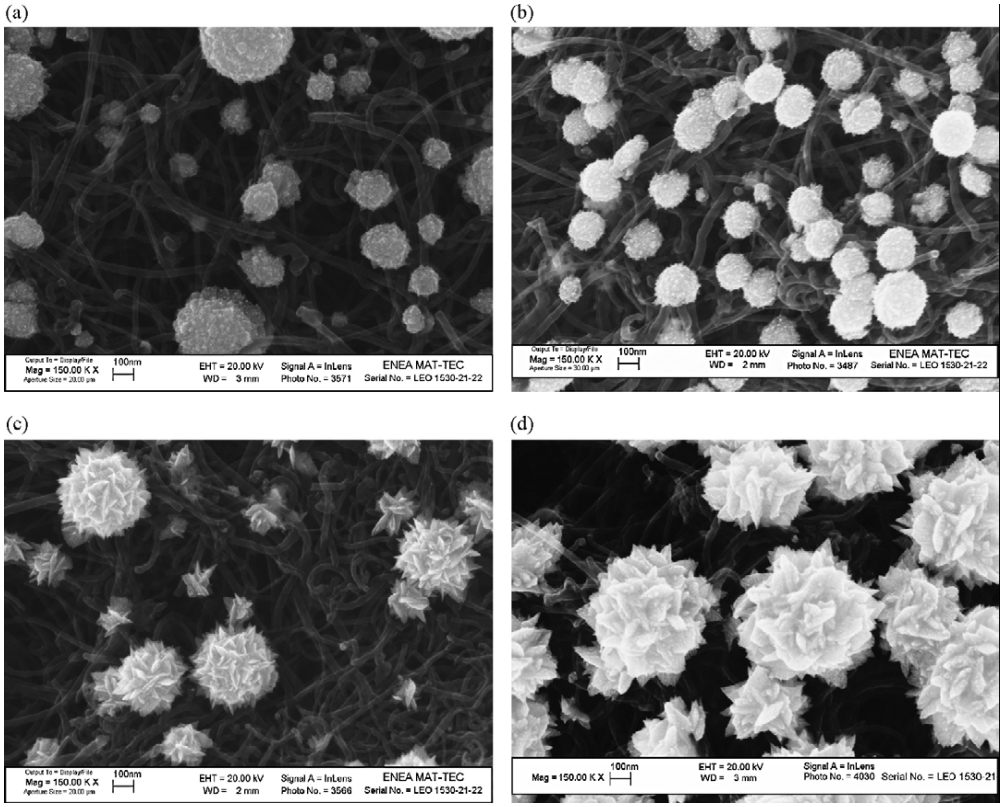

Fig. 2.9 SEM images of Pt nanoparticles deposited on CNTs with charge density values of (a) 120, (b) 180, (c) 240, and (d) 360 mC cm^{-2} [123].

2.2.3 Irradiation-assisted techniques

Microwave [105,112,134-143], γ ray [144-147], ultraviolet (UV) [148-151], and ultrasonic [64,152] irradiation have been employed to assist preparation of Pt-based electrocatalyst.

It is recognized that the rapid heating capacity of microwave could accelerate the precursor reduction and the crystal nucleation rate. Besides, the homogeneous microwave heating process could also alleviate the local temperature and concentration gradients, and thus promote the formation of narrow distributed noble metal NPs [134-136].

Liu et al. achieved remarkably uniform dispersion of Pt particles (3-5nm) on both the Vulcan carbon and CNTs through microwave-assisted polyol reduction process [134]. In their follow-up studies, bimetallic PtRu and PtSn electrocatalysts with outstanding catalytic performance were also synthesized on the carbon support with the aid of microwave irradiation [137, 138]. Analogous procedures were exploited by Deivaraj el al. to prepare PtNi/C nanocomposite [105]. During the synthesis process, a solution containing Vulcan carbon, metal precursors and poly(N-vinyl-2-pyyrolidone) (PVP) stabilizer was placed in the microwave reactor (100W) and heated for 10min. The as-prepared PtNi nanoparticles exhibited a relatively narrow size distribution ranging from 3-6nm.

Unlike conventional chemical method using reducing agent, the dissolved metallic ions M^{n+} are reduced by solvated electrons in the γ radiolysis technique:

$$M^{n+} + ne^{-} \rightarrow M^{0} \quad (10)$$

Due to the presence of very negative redox potential, γ-irradiation enables the ease of reducing metal precursor to zero valent state and it also eliminates the effects of the surrounding molecules and hence produces ultrapure and stable products [144].

In one recent report, Wang et al. utilized γ-irradiation to facilitate the fabrication of Pt NPs on MWCNTs [144]. A mixture of MWCNTs, chloroplatonic acid was first ultrasonicated and purged with N_2, and a solution of 2-propanol and sodium salt sulfonate was added as a hydroxyl radical scavenger and surfactant, respectively. The suspension was then irradiated using ^{60}Co source with a dose rate of 2kGy h^{-1}, in which the radicals produced from radiolysis of water promoted the reduction of the metal ions to nano-sized crystals. Similar γ-induced technique was developed by Yang et al. to anchor binary PtRu NPs on polymer-grafted MWCNTs [145].

Compared with commercial E-TEK Pt/C, the as-prepared catalyst exhibited significant enhancement on catalytic activity of methanol oxidation.

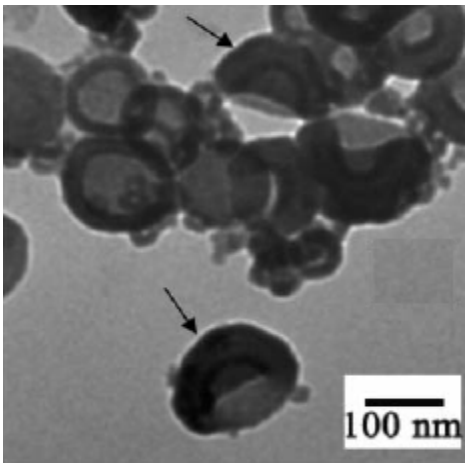

Fig. 2.10 Crown-shaped Pt NPs Pt@hC [149].

UV-assisted photocatalytic route has also been proposed for the synthesis of Pt/C nanocomposite [148]. By simultaneous photoreduction of Pt(IV) ions and photooxidative polymerization of phenol on titanium oxide (TiO_2), Pt@TiO_2 core-shell structures was constructed. Subsequent carbonization of the external polymer layer and removal of TiO_2 cores yielded the hollow Pt@C porous structure. The physical properties including the thickness and porosity of the carbon shell can be further tuned by changing the photo-irradiation time. In addition, UV photoreduction methodology has also been reported to regulate the formation of shape-controlled nanostructure. As shown in Fig.2.10, crown-shaped Pt NPs with a shell of 10-30nm in thickness were synthesized using an modified UV irradiation method, in which NH_2 terminal dendrimer aggregates were added serving as both the template and stabilizers [149].

Recently, Nagao et al. [152] developed a specially designed reactor to impregnate PtRu NPs on ultrasonically dispersed carbon support through reduction of Pt and Ru ions with $NaBH_4$. They claimed that monodispersed PtRu NPs were prepared on the carbon support with ultrasonic irradiation, while aggregated NPs were observed in the non-irradiated sample. Electrochemical measurement further revealed higher methanol oxidation current for the catalyst prepared under ultrasonic irradiation. In addition, the promoting effect of ultrasonic irradiation was confirmed by Xing's

research group [64]. Pt NPs with a size less than 5nm were homogeneously synthesized on sonochemically treated CNTs via EG reduction method.

2.2.4 Physical vapor deposition (PVD)

Physical vapor deposition has been explored as an alternative synthesis approach to decorate Pt-based electrocatalyst on carbon substrate. A wide range of PVD fabrication methods include sputtering [153-163], pulse laser ablation [12, 164], electron beam deposition [165, 166], etc.

Sputtering relies on the argon plasma to bombard the target, followed by the deposition of target material on different kinds of substrates. For example, a Pt/CNTs/Carbon-paper (CP) composite electrode was integrated through a combination of chemical vapor deposition (CVD) and sputter-coating method [160]. The CNTs was first in-situ grown onto the carbon paper using a CVD process under optimized temperature and gas flow rate. After the growth of CNTs, the obtained CNTs/CP hybrid membrane was placed in a radio frequency magnetron sputtering system. The sputter-coated Pt/CNT/CP electrode has shown a marked improvement in terms of catalytic activity and stability through polarization and accelerated degradation tests. In situ cyclic voltammetry measurements further confirmed a higher Pt utilization and a better corrosion resistance of Pt/CNT/CP electrode.

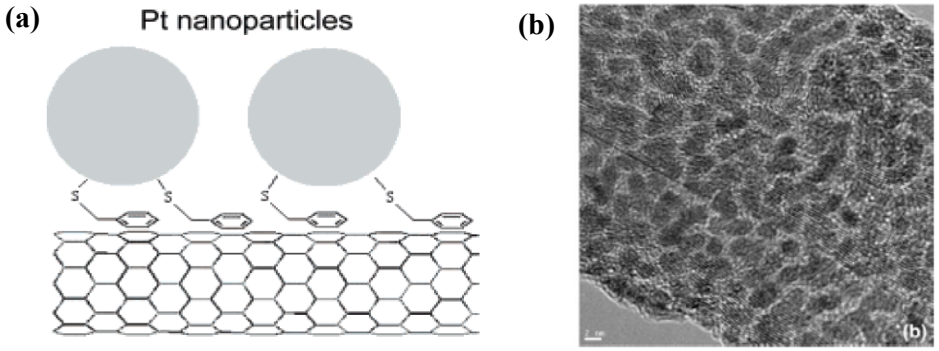

Fig. 2.11 (a) schematic illustration of Pt attached onto SH functionalized CNTs and (b)HRTEM images of Pt/CNT fabricated by EBD techniques [165].

Electron beam deposition (EBD) involves the evaporation of a target material using electron-bombardment, which is generated from a hot filament and focused with a magnetic field. The work of Yang et al. [165] provided an excellent example for the potential use of EBD to prepare Pt/CNTs electrocatalyst. As shown in the TEM image

(Fig.2.11 (b)), a nominal 1nm-thick layer of Pt NPs were homogeneously deposited onto the noncovalent modified CNTs using an electron-beam evaporator (0.15nm/min, $2*10^{-8}$ torr). On the basis of XPS investigation, the high dispersion and firm adhesion could be explained by the strong interaction between Pt NPs and mercaptan (SH) group on the surface of functionalized-CNTs.

Pulsed laser deposition (PLD) is similar to the EBD described above but utilizes a high-power pulsed laser instead of electron beam. The laser pulse is absorbed by the target to vaporize the substance and create a plasma plume. The plasma containing various species will deposit on a substrate and grow into thin film. The synthesis of bimetallic PtSn electrocatalyst with different composition has been demonstrated by Bommersbach and coworkers [12]. During the PLD synthesis, the pressure of the chamber was found to be correlated with the structure and morphology of the resulting nanoparticles. It was assumed that the increase in background pressure could reduce the kinetic energy and surface mobility of the deposited species, thereby favoring the formation of PtSn NPs with high alloying degree.

2.3 Characterization methodology

2.3.1 Physicochemical characterization

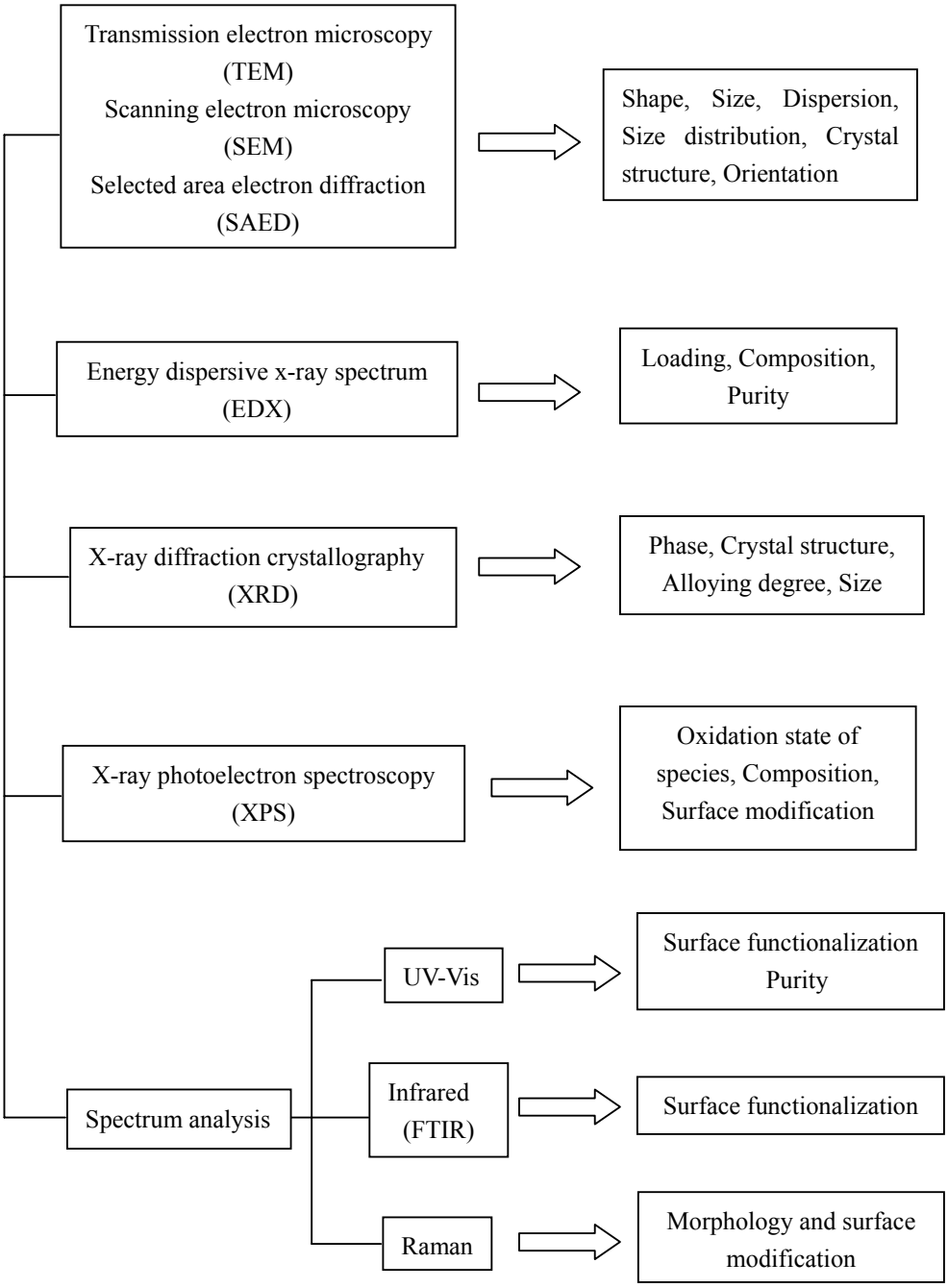

Fig. 2.12 Physicochemical characterization methods

2.3.1.1 Electron microscopy analysis

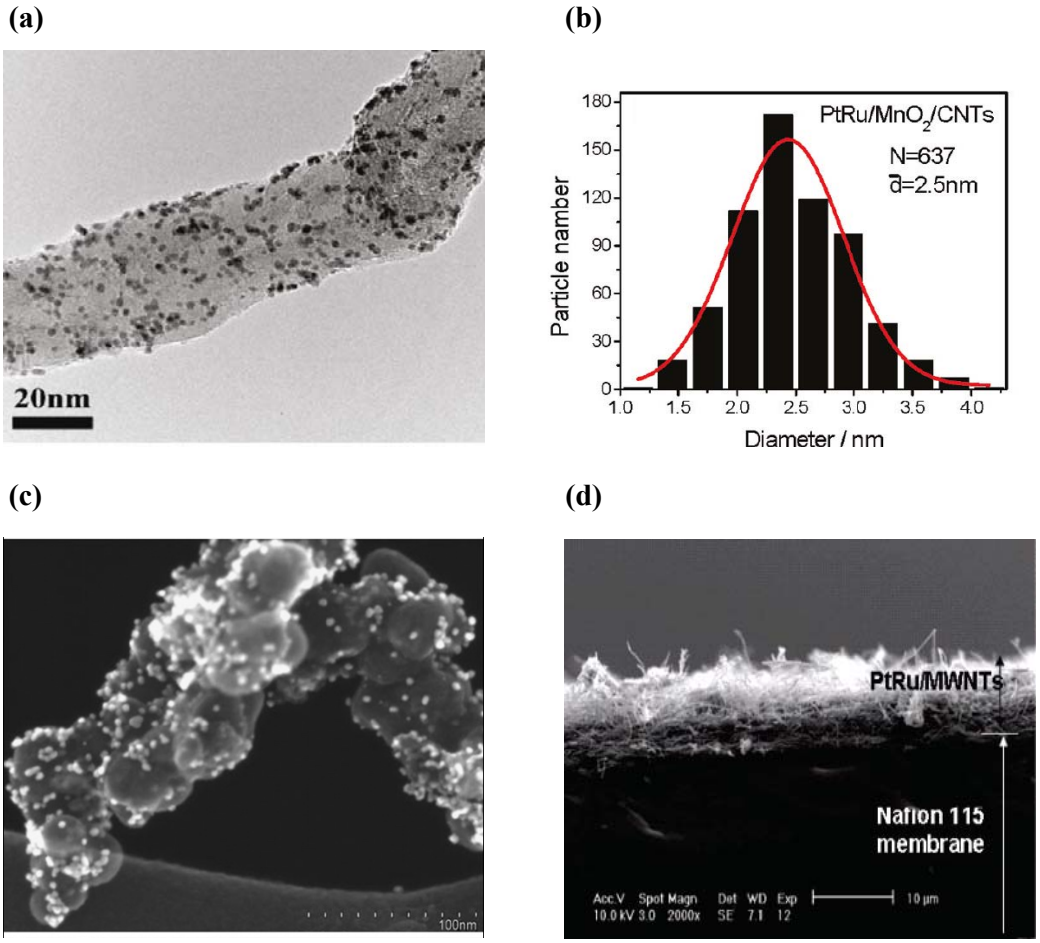

Fig. 2.13 (a, b)TEM image of PtRu-MnO_2/CNTs and corresponding PtRu size histograms [85]. (c)High-Resolution-SEM image of Pt/CNTs [167] (d) Cross-sectional SEM images of partially oriented PtRu/MWCNTs catalyst layer [71].

The morphology of the Pt-based nanomaterials including shape, size and dispersion of NPs can be directly observed on SEM and TEM (Fig.2.13a,c). Besides, it is convenient to plot the size distribution profile and calculate the mean particle size as well as the standard deviation using image processing software such as image-J (Fig. 2.13b). Sometimes, paranormal and cross-sectional images of electron microscope can also provide important information about the orientation and interfacial properties of Pt/C electrocatalyst (Fig. 2.13d).

As reported in a number of research papers, SAED and high resolution TEM (HRTEM) are very powerful tools to analyze the crystalline structure of nanomaterials. As shown in Fig.2.15(a), typical polycrystalline Pt NPs display electron diffraction

ring patterns, in which each ring can be indexed to a specific crystal plane. For Pt-based fcc structure, the lattice parameter of a single NP can be calculated using the following equation:

$$d = \frac{a}{\sqrt{h^2 + k^2 + l^2}} \tag{11}$$

where a=lattice parameter, a_{Pt}=0.392nm, h/k/l=miller index, d=interplanar spacing of (h,k,l) planes. Here, the interplanar spacing can be precisely measuring based on the lattice fringe of HRTEM images. The d spacing of NPs in the Fig. 2.14 (b) is 0.228nm corresponding to Pt(111) [85], while the d spacing (0.22nm) in Fig.2.14 (c) is slightly smaller than 0.23nm for Pt(111), indicating the lattice contraction caused by the formation of PtCo solid solution [87].

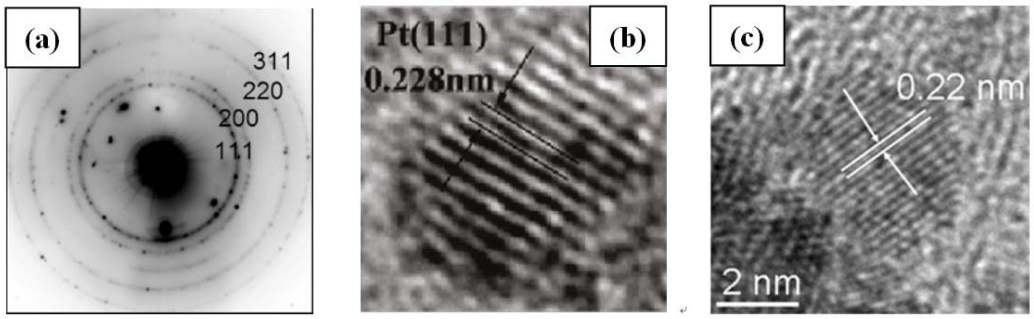

Fig. 2.14 (a) SAED pattern of cubic Pt NPs. [168]; (b) HRTEM images of Pt/MnO_2/CNT [85] and (c) Pt_3Co/CN_xT [87].

2.3.1.2 EDX analysis

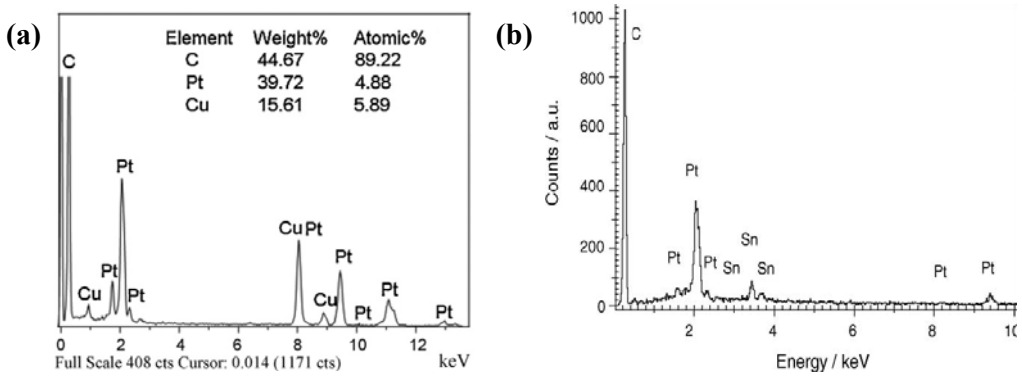

Fig. 2.15 EDX spectrum of (a) Pt/DWCNTs [169] and (b)$Pt_{75}Sn_{25}$/C nanocomposite [98]

Even though precise atomic concentration of each element can hardly be extracted from EDX spectrum, average composition including the overall metal

loading as well as the ratio between Pt and secondary metal can be obtained. As shown in the Fig.2.15, the existence of Pt or PtSn was confirmed through the featured peaks in the EDX spectrum. Element mapping with EDS can reflect the distribution of the elements on the surface. When the EDX detector works under scanning TEM mode, its resolution can reach up to nanometer scale. After scanning a certain distance, no obvious segregation of composition was found on the sample of PtRu/C (Fig.2.16). It was manifested that the PtRu alloy was formed rather than the separate Pt, Ru phase. In some other cases, EDX analysis may also provide evidence for the presence of impurities or the surface functionalization on the substrate, if the corresponding peaks other than carbon or metal element are present in the spectra.

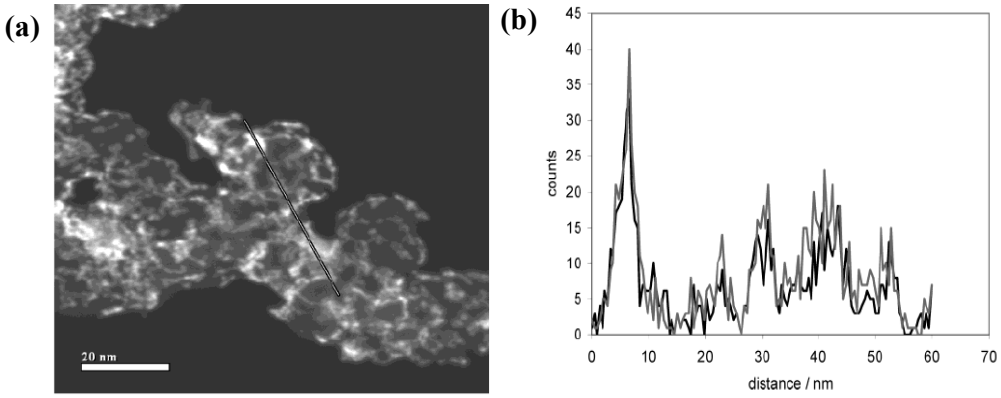

Fig. 2.16 Dark field image of PtRu/C and STEM spectrum [19]

2.3.1.2 XRD analysis

The crystalline structure of the carbon supported Pt-based nanomaterials can be easily determined through XRD analysis. Fig.2.17 shows a typical XRD pattern for Pt/CNTs, in which four characteristic peaks at around 39.7°, 46.2°, 67.4°, 81.2° correspond to fcc Pt (111), (200), (220), (311) planes. And hexagonal graphite (002), (100), (004), (110) reflections display in the XRD diffractogram at around 26.5°, 42.4°, 54.7°, 77.4°, respectively [94].

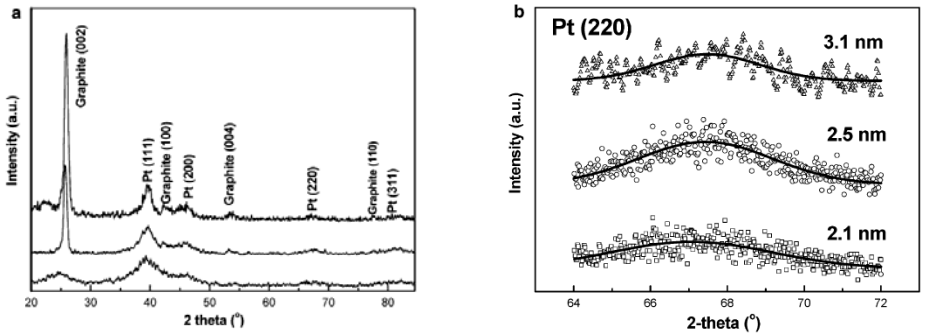

Fig. 2.17 (a) Powder XRD patterns of Pt/MWCNTs (via HCHO method), Pt/MWCNTs (via EG method), Pt/XC72 (via EG method) and (b) detailed Pt(220) peak [94].

According to the isolated (220) peak, the mean particle size of NPs can be estimated using scherrer equation:

$$d = \frac{0.9\lambda_{K\alpha}}{B_{2\theta}.Cos\theta} \tag{12}$$

where d is the average particle size of Pt NPs(nm), $\lambda_{K\alpha}$ is wavelength of X-Ray (Cu $\lambda_{K\alpha}$= 0.15406nm), θ is the peak angle, and $B_{2\theta}$ is the full width half maximum in radians [94, 100].

For the carbon supported PtRu binary electrocatalyst, the fcc Pt diffraction peaks may positively shift to the high angle value due to the incorporation of smaller Ru atoms in fcc Pt crystal. On the contrary, negative shift was observed on the X-ray diffractogram for PtSn/CNTs samples. The obvious peak line displacement indicates the formation of Pt-based nanoalloy (Fig. 2.18).

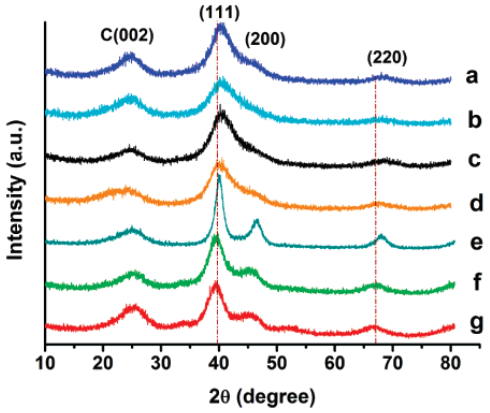

Fig. 2.18 XRD patterns of the (a)$Pt_{0.495}Ru_{0.505}$/C (b)$Pt_{0.467}Ru_{0.495}Sn_{0.038}$/C (c) $Pt_{0.472}Ru_{0.413}Sn_{0.115}$/C (d)$Pt_{0.504}Ru_{0.354}Sn_{0.142}$/C(e)$Pt_{0.537}Ru_{0.243}Sn_{0.22}$/C (f) $Pt_{0.487}Ru_{0.152}Sn_{0.361}$/C and (g)$Pt_{0.526}Sn_{0.474}$/C [170].

Furthermore, the alloying degree of bimetallic PtM nanomaterials can be calculated using the following equation:

$$Alloying\ degree = (a - a_{Pt})/(a_{PtM} - a_{Pt}) \tag{13}$$

$$a_{PtM} = a_{Pt} - cx_M \tag{14}$$

$$a = \frac{\lambda}{2sin\theta}\sqrt{h^2 + k^2 + l^2} \tag{15}$$

where a is the experimental lattice parameter obtained from XRD pattern, a_{Pt} is the lattice parameter of carbon supported pure Pt (0.39155nm), c is a constant obtained from the lattice parameters of unsupported Pt and PtM alloy, x_M is the nominal atomic fraction of the second metal [171,172]. Despite absence of single crystalline phase of second metal in XRD pattern, the alloying degree is always less than unity under conventional circumstance. It could be inferred that the amorphous M phase may also exist in the PtM/C sample.

2.3.1.3 XPS analysis

XPS measurements are usually performed to analyze the atomic fraction of metallic and oxide components in the Pt-based nanomaterials. As shown in the Pt 4f spectrum (Fig.2.19), the more intense duplets at 71.1eV (Pt $4f_{7/2}$) and 74.4eV (Pt $4f_{5/2}$) were attributed to metallic Pt^0, while the less intense duplets at 72.2eV and 75.8eV is assigned to Pt(II) in PtO or $Pt(OH)_2$. By comparing the relative intensities of the peaks, the amount of dominant metallic Pt(0) species can be calculated. Since the Ru $3d_{3/2}$ overlaps with C 1s, Ru $3p_{3/2}$ spectrum was deconvoluted for the accurate determination of Ru oxidation states [103]. As shown in the Fig. 2.19(b), the peaks at 462.5eV and 465.8eV were credited to Ru(0), and Ru(IV). Based on the relative heights of the two peaks, the majority Ru species were found to present in the Ru(0) metallic states.

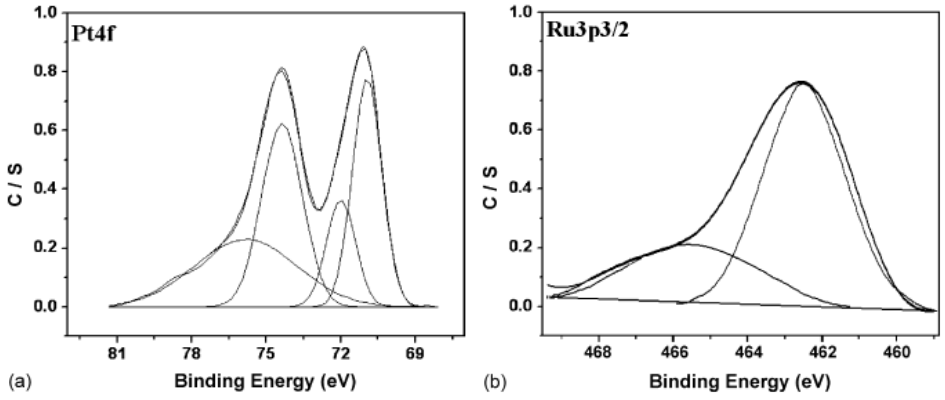

Fig. 2.19 Regional XPS spectra of (a) Pt 4f and (b) Ru3p for the PtRu/C catalyst [101].

XPS is also very useful to detect remaining impurities and verify the surface functionalization. For example, the S2p spectrum of thiol-stabilized Pt colloid was examined by Liu et al. to confirm the successful modification of Pt surface with –SH functional group [117].

2.3.1.4 Raman spectrum analysis

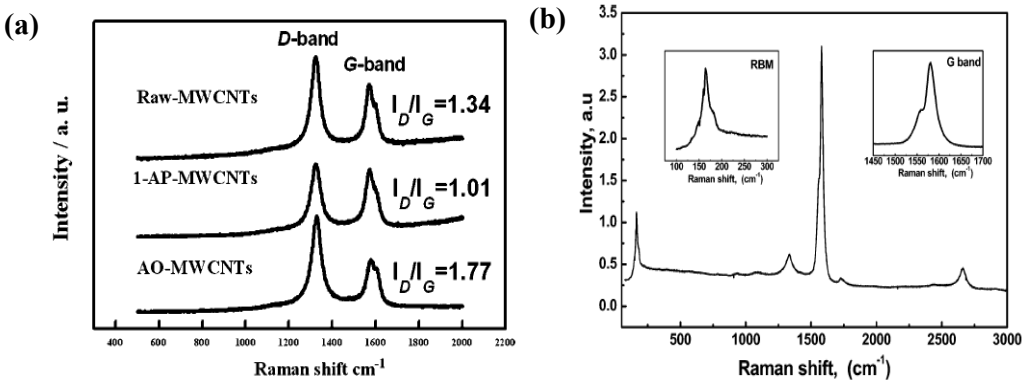

Fig. 2.20 Raman spectra of (a) pristine MWCNTs, 1-AP modified MWCNTs, acid oxidized MWCNTs [83] and (b) SWCNTs [132].

The Raman spectrum was commonly used to study the surface functionalization of nanostructured carbon. Wang et al. employed 1-aminopyrene (1-AP) to modify the inert CNT surface for the improved PtRu dispersion [83]. As shown in the Fig. 2.20(a), both pristine and functionalized CNTs show similar scattering pattern. The peak near 1330cm^{-1} is referred to the disordered graphite structure (D-band), which can be attributed to pentagons, heptagonal, the pentagon-heptagon pairs, or line defects [134]. The other peak at around 1570cm^{-1} corresponds to the sp^2-hybrized carbon atoms, which reflects the ordered graphite structure (G-band). In a general sense, the ratio of I_D/I_G can be considered an indicator of graphitic structure perfection. The smaller I_D/I_G value of 1.01 for 1-AP-CNTs implied the original defect sites on CNTs were partially covered by 1-AP molecules. In contrast, the oxidized CNTs with a large I_D/I_G value of 1.77 suggested the detrimental effect of acid oxidation treatment on the graphite structure of CNTs.

Furthermore, it was found that the frequency of the ring breathing mode (RBM) in Raman spectrum is inversely proportional to the diameter of CNTs. For a single nanotubes [69],

$$\omega_r = 224/d \text{ cm}^{-1} \quad (16)$$

where ω_r is the frequency of RBM. For bundles, the relationship between frequency and diameter can be expressed as

$$\omega_r = 223.5/d + 12.5 \text{ cm}^{-1}. \quad (17)$$

Thus, the Raman spectrum can also be used to distinguish different kinds of CNTs and evaluate the dispersion state of CNTs. As shown the Fig.2.20 (b), the profile and frequency of RBM, G lines are consistent with the characteristic signatures of SWNTs, which has very small d and I_D/I_G ratio [132].

2.3.1.5 UV-Vis an FTIR spectrum analysis

Both the UV-vis and FTIR spectrum are typically used to elucidate the surface functionalization of CNT. In order to provide anchoring sites for the homogeneous dispersion of Pt NPs, 1-aminopyrene (1-AP) was noncovalent coated onto the pristine CNT [83]. As shown in the Fig., the peaks at ca. 285 and 365 nm correspond to the characteristic 1-AP adsorption. Since the pristine CNTs present a featureless spectrum (Fig.2.21(a), dotted line), the existence of peak at 290nm in 1-AP modified CNTs (Fig.2.21(a), solid line), strongly suggested the noncovalent binding of 1-AP molecules on the pristine CNT surfaces. It is worth noting that the absorption bands become broader, as a result of π-π interactions between the pyrenyl group of 1-AP and six-membered rings of CNT sidewalls (dashed line, Fig. 2.21 a).

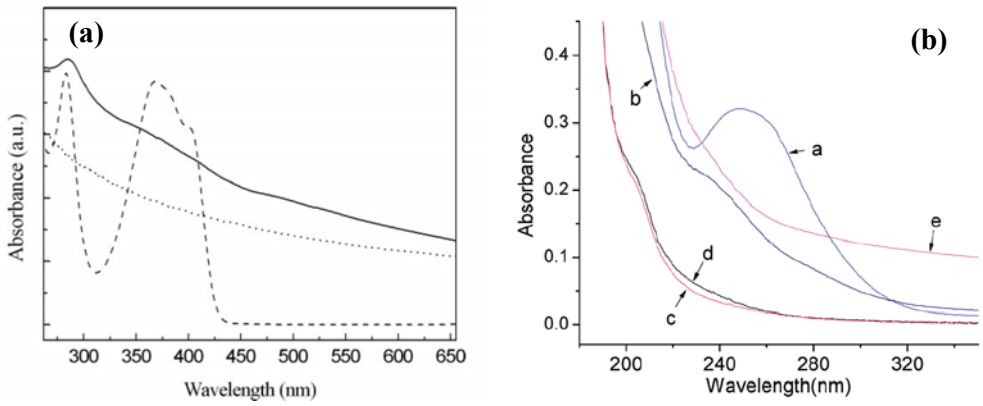

Fig. 2.21 UV-Vis adsorption spectra of (a) pristine CNTs (dotted line), 1-aminopyrene (dashed line), and 1-AP-CNTs (solid line) in THF suspension [83]. (b) Variation of UV-vis absorption spectra during the photoreduction of H_2PtCl_6 [151]

In addition, UV-vis spectrum has been reported to monitor the extent of reaction during the synthesis of Pt NPs. For instance, Bai et al. developed a Polyethyleneimine (PEI)-mediated method to prepare monodispersed Pt NPs via UV photoreduction [151]. As shown in the Fig., the original H_2PtCl_6 aqueous solution displays a strong absorption band in 250 nm (Fig. 2.21 b-(a)). After mixing with PEI, this peak was replaced by a new shoulder peak at 235 nm because of ligand-to-metal charge transfer (Fig. 2.21b-(b)). After only 5 min of UV irradiation, the characteristic PEI/$PtCl_6^{2-}$ complex peak at 235 nm totally disappears, and another shoulder peak at 210 nm appears (Fig. b-(c)). This phenomenon can be explained by the rapid kinetics of reducing Pt^{4+} to Pt^{2+}. Due to the slow reaction rate, it will take over one day to eventually reduce the Pt^{2+} to Pt^0 (Fig. 2.22 b-(b-e)).

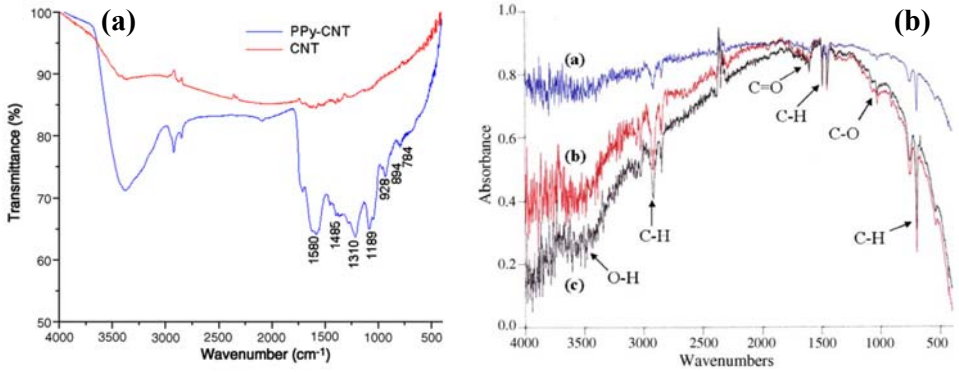

Fig. 2.22 FTIR spectra of (a) PPy-MWCNTs [95] and (b) O-CNT [113].

Recently, conducting polymer composite (Polypyrrole/CNT) was fabricated as PtRu catalyst support for the enhanced electrocatalysis of methanol. The successful in-situ polymerization of Polypyrrole (PPy) on CNT was readily confirmed by the FTIR analysis [95]. Fig. 2.22(a) shows the FTIR spectrum of PPy-CNTs, in which the adsorption bands at 1580 and 1485cm^{-1} are assigned to the 2, 5 substituted pyrrole group and polypyrrole ring vibration. The peak at 1310 cm^{-1}, 1189cm^{-1} corresponds to the =C-H in plane vibration and C-N stretching vibration. The rest peaks including peaks at 784, 894, 928 cm^{-1} all confirmed the coverage of PPy on the CNT surface. Similarly, the oxidization of CNTs through strong acid treatment was also verified by FTIR spectrum. As shown in the Fig. 2.22(b), featured C-H, C=O, O-H adsorption bands displayed in the spectrum of oxidized-CNT sample. These generated carbonyl

and hydroxyl groups on CNTs surface are assumed to improve the adhesion between Pt NPs and CNTs sidewalls [113].

2.3.2 Electrochemical investigation

Conventional electrochemical investigation techniques included the cyclic voltammetry (CV), CO stripping, chronoamperometry (CA), accelerated durability test (ADT), electrochemical impedance spectrum (EIS), polarization which are summarized as follows (Fig. 2.23).

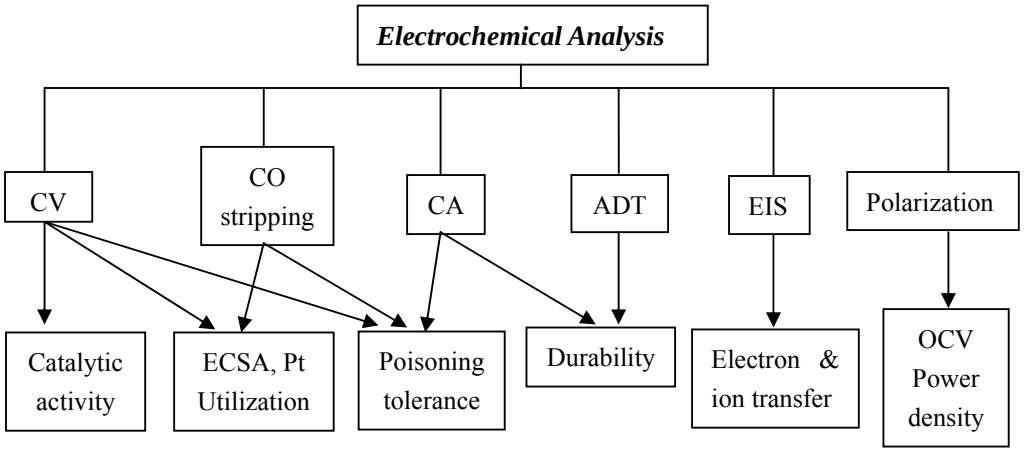

Fig. 2.23 Typical electrochemical investigation techniques (OCV: open circuit voltage.)

2.3.2.1 Hydrogen adsorption/desorption

It is generally believed that a large electrochemical surface area (ECSA) means more active Pt sites are available for electrode reaction. Thus ECSA is hence one of the most important parameters for charactering a fuel cell electrode. Adsorption and desorption of underpotentially deposited hydrogen in a stationary voltammograms is conventionally used to evaluate the ECSA of the Pt catalyst, which can be expressed as :

$$Pt + H^+ + e^- \leftrightarrow Pt - H_{ads} \quad (18)$$

Fig. 2.24 shows a typical H electrosorption voltammetric profile for the Pt/CNT catalyst in 1M H_2SO_4. Characteristic peak in the hatched area are attributed to atomic hydrogen desorption on the Pt surface and ECSA can be determined by:

$$ECSA = \frac{Q}{q^0 \times M_{Pt}} \tag{19}$$

where q^0 is the charge for monolayer hydrogen adsorption on Pt, q^0=210μC·cm^{-2}, a value generally admitted for polycrystalline Pt electrodes [174], M_{Pt} is the mass of the Pt loading, Q is the charge for the hydrogen desorption (μC). Q can be obtained by integrating the area under the potential window for H desorption peak after subtracting the charge from the double-layer region.

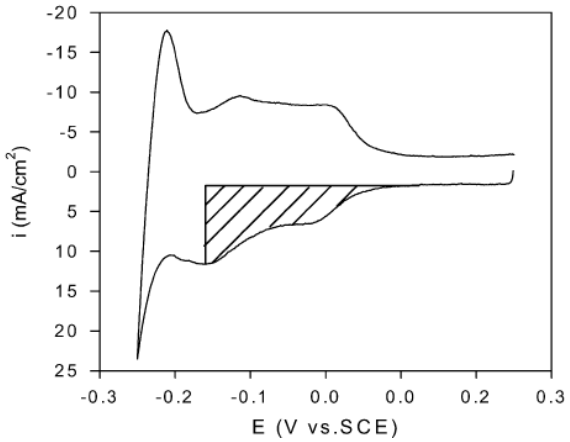

Fig. 2.24 Cyclic voltammetry of microwave synthesized Pt/CNT catalyst in 1M H_2SO_4 with a scan rate of 50mv/s [134]. (The hatched area represents the amount of charge for the electrosorption of H on Pt).

Moreover, the theoretical electrochemical surface area or geometrical specific surface areas (S_{geom}) can be derived using the following equation:

$$S_{geom} = \frac{6000}{\rho d} \tag{20}$$

where d (nm) is the mean particle diameter, ρ (g/cm^3) is the density of NPs [85, 175]. A comparison of $ECSA$ with S_{geom} can tell how many surface atoms are electrochemical active, i.e., make contribution to the electrode reaction. Therefore, the ratio of $ECSA/S_{geom}$ is considered a measure of Pt utilization efficiency [64].

2.3.2.2 Catalytic activity towards alcohol oxidation

The electrocatalytic activity of Pt-based catalyst towards methanol oxidation reaction (MOR) or ethanol oxidation reaction (EOR) are conventionally elucidated by cyclic voltammetry in an acidic solution ($HClO_4$ or H_2SO_4), containing the target

substance.

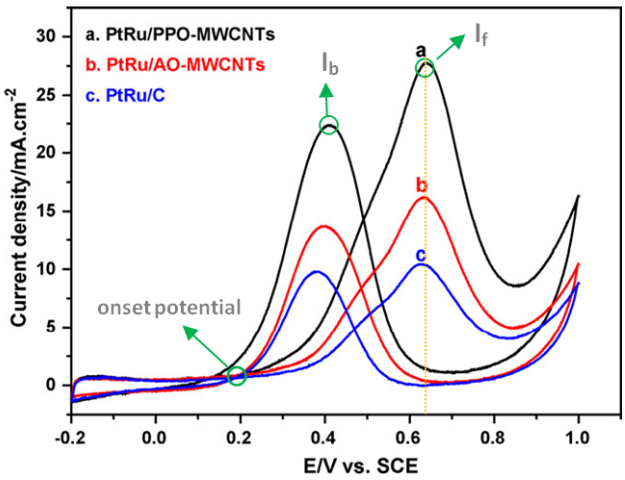

Fig. 2.25 Cyclic voltammograms of methanol oxidation on PtRu/PPO-MWCNTs (a), PtRu/AO-MWCNTs (b) PtRu/C (c) in 0.5M H_2SO_4+1M CH_3OH saturated by N_2 [92].

Fig. 2.25 illustrates a representative CV curve recorded at a scan rate of 50mV/s in the aqueous solution of 0.5M H_2SO_4+1M CH_3OH for three kinds of electrocatalyst . The CV voltammogram shows an anodic peak at 0.64V during the forward sweep and one at 0.4V during the reverse scan [92]. The former peak corresponds to methanol oxidation (MOR) process, while the latter one is associated with the removal of adsorbed carbonaceous species (CO_{ad}). The onset potential of methanol oxidation for (a) shows an obvious negative shift compared with (b) and (c). In principle, the onset potential of the forward peak is closely related to the breaking of C-H bonds and subsequent oxidation of CO_{ad} intermediates on Ru-OH sites. It is also noted that the current density of the forward peak density (I_f) for (a) is significantly higher than that for (b) and (c). Therefore, the lower onset potential and higher I_f are strong evidence for the superior catalytic activity of (a) towards MOR.

Moreover, the ratio of forward anodic peak current (I_f) to backward anodic peak current (I_b), (I_f/I_b), is known as an important index to evaluate catalyst tolerance to carbonaceous species. A larger (I_f/I_b) indicates more effective removal of the poisoning species on the electrode surface. The (I_f/I_b) ratio is 1.24, 1.18, 1.06 for (a), (b) and (c), respectively, suggesting the highest tolerance of (a) towards catalyst poisoning [92].

2.3.3.3 CO-Stripping

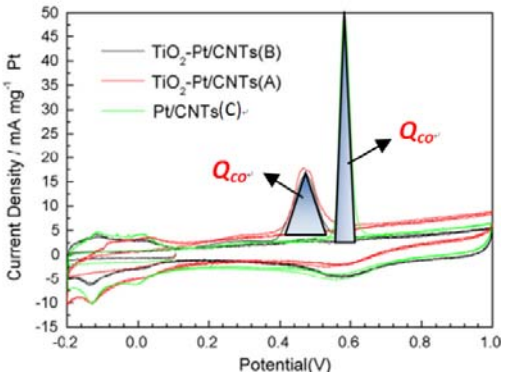

Fig. 2.26 CO-stripping voltammograms of (A) TiO_2-Pt/CNT (B) TiO_2-Pt/CNT after heat-treatment and (C) Pt/CNTs [84].

Because the CO species are the main poisoning intermediate, a good electrocatalyst should have excellent CO oxidation ability, which can be measured using CO stripping test. For a typical CO stripping test, carbon monoxide was first adsorbed onto the catalyst by bubbling it in supporting electrolyte at a given voltage. Then the dissolved CO was purged with N_2 and the potential was subsequently cycled to oxidize the CO as below (Fig. 2.26).

$$Pt - CO + H_2O \leftrightarrow Pt + CO_2 + 2e^- + 2H^+ \quad (21)$$

It is evidently seen that peak potentials of CO oxidation on catalyst A and B are much lower than on catalyst C and the onset potentials for A and B shift remarkably towards the negative direction [84]. These results imply CO species are more readily removed on the surface of former two catalysts, in other words, catalyst A and B may have very enhanced CO tolerance during the electrocatalysis. According to the CO-stripping voltammograms in Fig.2.26, we can also estimate the ECSA using the following equation:

$$ECSA = \frac{Q_{CO}}{420\mu C cm^{-2} \times M_{Pt}} \quad (22)$$

where 420μC·cm^{-2} is the charge for monolayer CO adsorption on Pt, Q_{CO} can be obtained by integrating the area under the CO desorption peak (Fig. 2.26 (b)).

2.3.3.4 Durability Test

2.3.3.4.1 Chronoamperogram

In order to investigate the long-term catalytic performance of electrocatalyst, a chronoamperometric curve was generally plotted at a fixed potential. Fig.2.27 shows a chronoamperogram for bimetallic PtM/CNTs (M=Fe, Co, Ni) catalyst in 1M H_2SO_4 + 0.5M CH_3OH [176]. At the initial stage, the potentiostatic current may decay rapidly due to the double layer charging. After a short period, a gradual current degradation was observed, which is associated with the accumulation of intermediate species such as CO_{ads} on the electrode surface. The current density will eventually reach a steady state, while the long time current decay may be due to the adsorption of SO_4^{2-} anions that blocks the methanol oxidation reaction. It is clearly seen that PtCo/CNT exhibited the lowest current degradation rate and thus highest stability towards methanol oxidation.

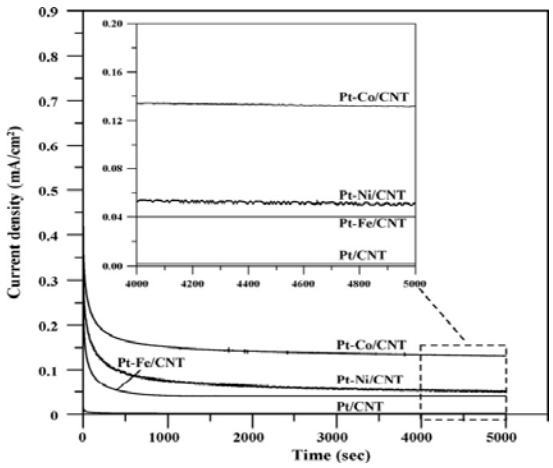

Fig. 2.27 Current – time curves for methanol oxidation at 0.45Vfor carbon supported PtM bimetallic electrocatalysts [176].

2.3.3.4.2 ADT test

The best and reliable method to test the durability of a fuel cell is to run the fuel cell directly, hour by hour, at the desired conditions, which is nevertheless costly in both time and materials. So accelerated durability test (ADT) methods including CV cycling, high temperature and low humidity operation are developed in recent years. Normally, ADTs are carried out under more "stressful" conditions compared to actual use conditions to expedite performance degradation process. It was reported that the dynamic oxidation could accelerate the corrosion process and closely resemble the real operating condition of PEMFC. ADT based on the carbon oxidization was thus

carried out to investigate the durability of electrocatalyst [160]. As illustrated in Fig. 2.29(a), the activity loss mainly occurred in the first 10 oxidation cycles. After 100 oxidation cycles, the Pt/VXC72R catalyst lost more than 80% of its activity, whereas the Pt/CNT catalyst remained at 50% activity.

The long-term electrochemical stability of Pt/C catalyst can also be evaluated in the terms of current density loss [93] or ECSA degradation after repeated potential sweeping [115, 116, 160]. As shown in the Fig. 2.28 (b), the initial value of I_f is 440, 480, 910g/A for catalyst a, b, c, respectively. After 1000 cycles, 59% and 63% of its maximum value remains for a and c. By contrast, I_f degraded very slowly for catalyst b and only 17% I_f decay was observed [93].

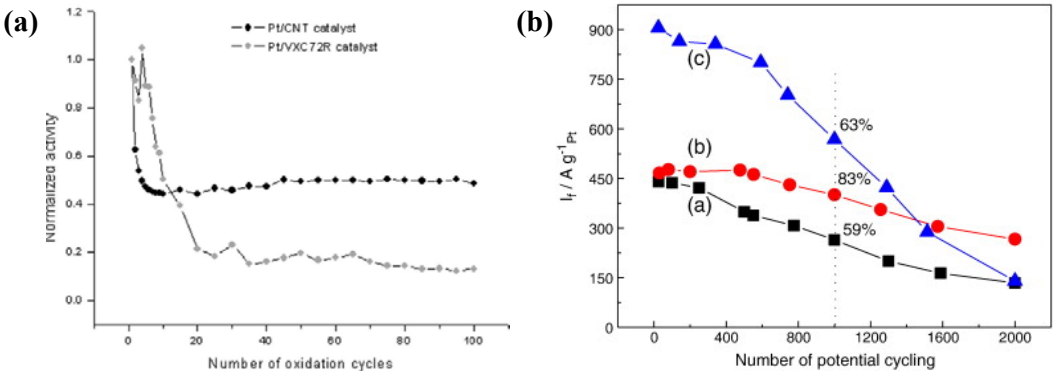

Fig. 2.28 (a) The first 10 oxidation cycles for Pt/CNT and Pt/VXC72R catalysts between oxidation potentials of 0.6 and 1.8 V [160] and (b) Methanol oxidation forward peak current (I_f) for PtRu/CNTs, MnO_2/PtRu/CNTs, and PtRu/MnO_2/CNTs during the repeated potential cycling [93].

2.3.3.5 Electrochemical impedance spectrum (EIS)

Besides ECSA, the interfacial charge (electron and ion) transfer is of significant importance for the electrode reaction, which can be examined by EIS. EIS spectra are plotted either in Bode or Nyquist form. In a Bode plot, the amplitude and phase of the impedance are plotted as a function of frequency (*f*), while in a Nyquist plot the imaginary part of impedance (Z_{im}) is plotted against the real part (Z_{real}) at each frequency. As shown in Fig.2.29, Randles equivalent circuit is conventionally adopted to fit the impedance behavior of fuel cell [109,127,163,177]. In this mode, the high-frequency (HF) intercept is related to ohmic resistance of the fuel cell stack (R_Ω),

the HF semicircle can be assigned to a combination of the double-layer capacitance in the porous Pt/C catalyst layer (C_{dl}) and the charge transfer resistance (R_{CT}). C_{dl} can be substituted by constant phase element (CPE). The impedance of CPE can be expressed by [163]

$$Z_{CPE} = A/(j\omega)^n \quad (23)$$

where A is a frequency independent constant, ω is angular frequency ($\omega=2\pi f$), n is adjustment parameter, $j=\sqrt{-1}$. The straight line in the low frequency (LF) region corresponds to mass transport limitation which can be clarified by applying Warburg diffusion element (W) for semi-infinite diffusion (Fig. 2.30a).

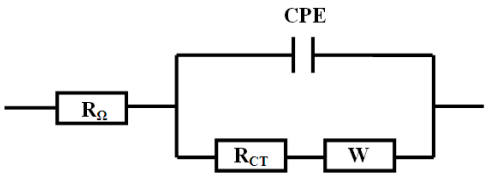

Fig 2.29 Equivalent circuit of CNT modified GCE electrode in 0.5M H_2SO_4 [127]

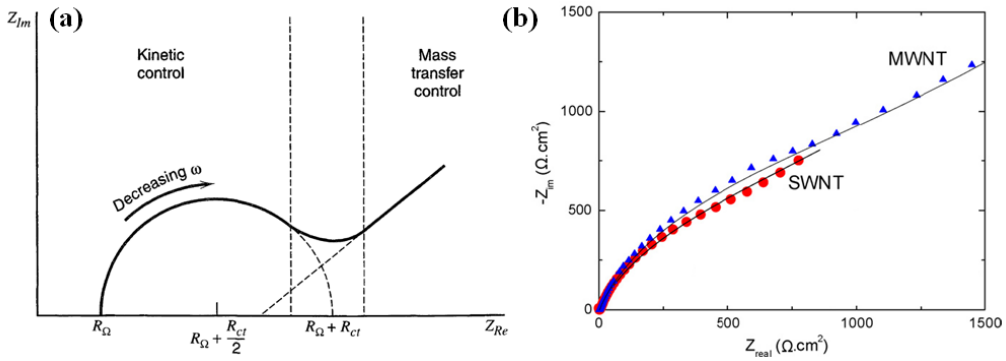

Fig. 2.30 (a) Impedance plot for an electrochemical system (Regions of mass-transfer and kinetic control are found at low and high frequencies, respectively) [178]. (b) Complex plane plots of electrochemical impedance spectroscopy of Pt electrodes at 0.6V in 0.5M H_2SO_4 [127].

As shown in a typical Nyquist plots (Fig. 2.30 b), a depressed semi-circle in the HF region is ascribed to the charge transfer at the carbon/electrolyte interface. According to the EIS fitted results, the SWNT/Nafion electrode displayed a higher value of W and lower value of R_{CT} in comparison with MWCNTs/Nafion electrode, which indicates that a rapid mass diffusion and charge transfer processes take place at

the electrode/electrolyte interface [127].

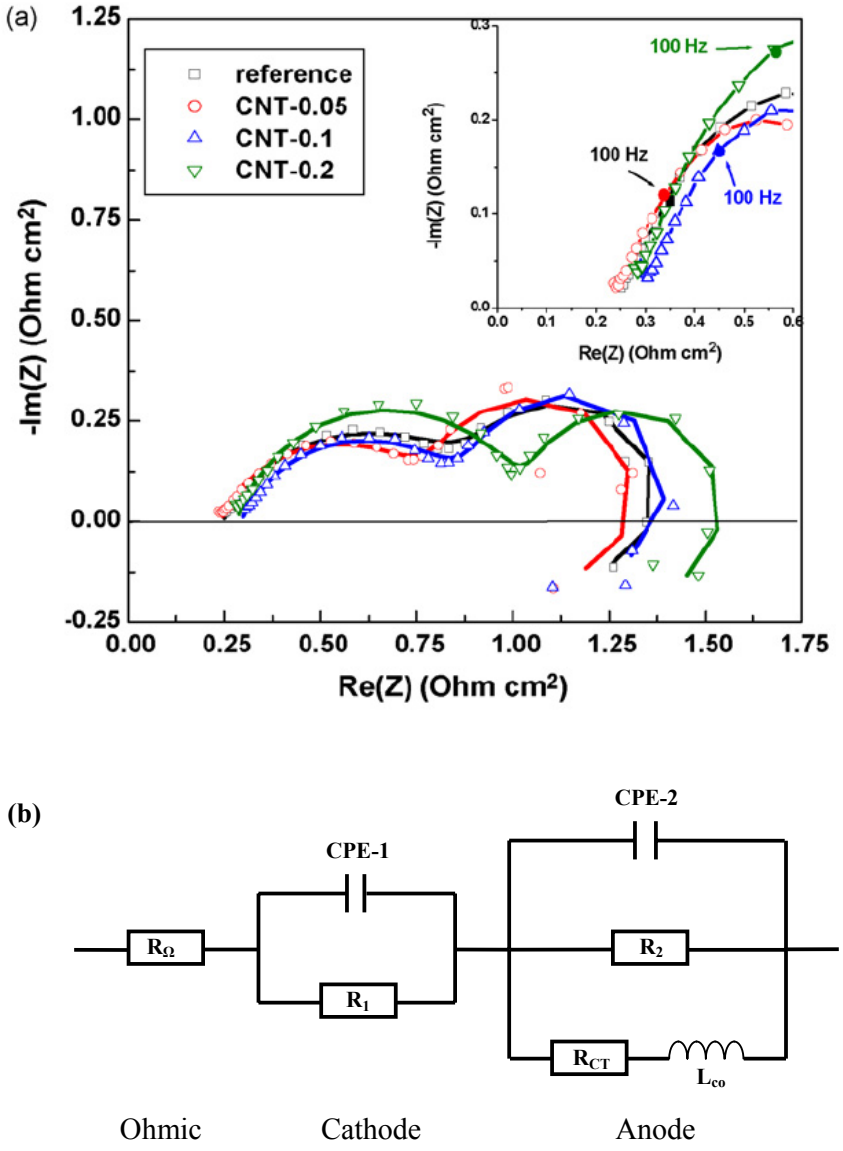

Fig. 2.31 (a) EIS curves for modified Membrane-electrode-assembly by introducing CNTs in cathode structure (T=50^0C, 3M CH_3OH, i=150mA/cm^2). (b) Equivalent circuit for MEA. (L_{co} is the inductance due to the slow relaxation of CO_{ads} covered on anode catalyst)[179].

In the case of the MEA of DMFCs, the overall impedance curve has two semicircles and one loop [179, 180], which can be simulated using the equivalent circuit in Fig. 2.31(b). The corresponding LF and HF arcs in complex impedance plane are attributed to the charge transfer resistance of the anode and cathode

reactions, respectively. Because methanol oxidation involves the release of six electrons, the kinetics of MOR is slower than ORR and the impedance associated with MOR is expected at LF region. The inductive loop at LF region reveals a phase shift between current and voltage, which is caused mainly by the sluggish CO_{ads} desorption on the surface of electrocatalyst [179].

2.3.3.6. Polarization curve

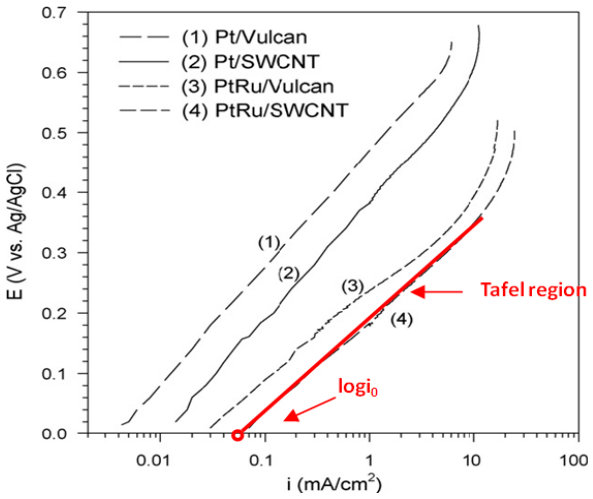

Fig 2.32 Tafel plots for methanol oxidation on various kinds of carbon supported catalyst in 1M H_2SO_4 + 2M CH_3OH at a scan rate of 10mV/s [117].

Tafel plots can be used to determine the exchange current density (i_0), which is a direct measure of the charge-transfer kinetics across the interface under equilibrium conditions [117, 130, 181, 182]. An electrochemical system with a large exchange current density has fast kinetics and can respond rapidly to a change in potential. Otherwise, the system has a sluggish electron transfer rate. As shown in the Fig 2.32, the linear Tafel region is obtained at the onset part of polarization curve under high overpotential (η), and both the Tafel slope (b) and i_0 can be identified using the following equation.

$$\eta = a - b\log i, \quad a = \frac{2.3RT}{\alpha nF}\log i_0, \qquad b = \frac{2.3RT}{\alpha nF} \tag{24}$$

Where α is anodic transfer coefficient, n is the number of electrons transferred, F is faradic constant 96487C/mol, the linear segment extrapolate to an intercept of log i_0

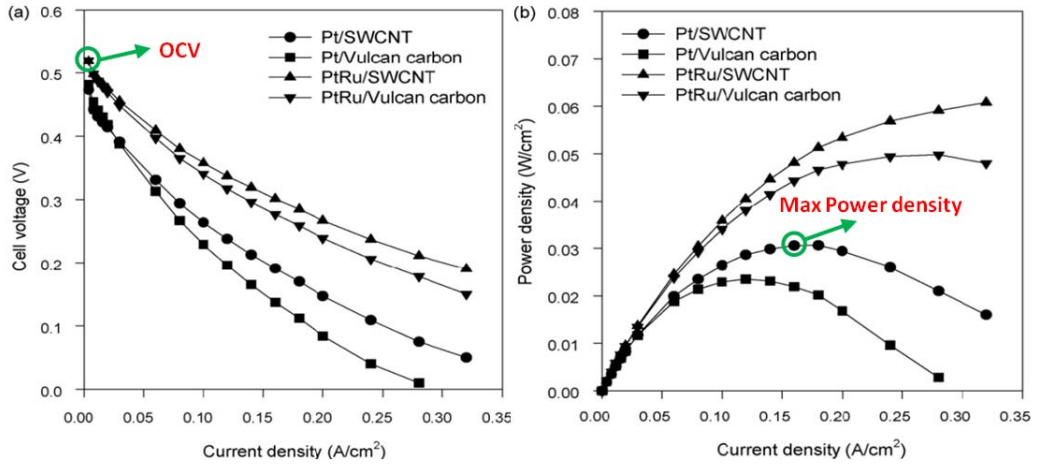

Fig. 2.33 Polarization(I-V) curves and power density (I-P) curves of single cell at 80 degree C. Anode: Pt on various carbon (4 mg cm^{-2}), 2M CH_3OH 2ml min^{-1}; Cathode: Pt/C(E-TEK) (3 mg cm^{-2}), O_2 500cm^3 min^{-1}[117].

Cell potential plotted as a function of current density under a set of operating conditions, known as galvanostatic polarization I-V curve, is the standard electrochemical technique for evaluating the performance of fuel cell. By measuring I-V curve, the effects of catalyst composition, the types of catalyst support, temperature, humidity, the flow rate of reactant on the cell performance can be characterized and compared systematically. Since power density is the product of current density and voltage (P=I*V), the I-V curve is often converted to I-P curve. As depicted in Fig. 2.33, open circuit voltage (OCV) and maximum attainable power density are the key parameters that can be obtained from I-V and I-P curve. It is shown that SWCNT supported bimetallic PtRu catalyst has high value of OCV and peak power density which suggests its superior fuel cell performance when compared with Pt/SWCNTs and commercial Pt/C [117]. Moreover, a typical I-V curve can be further divided into three regions including activation polarization (region I), the ohmic polarization (region II), and concentration polarization or mass transfer polarization (region III). At low current densities (region I), the potential drops sharply due to the sluggish kinetics of ORR [183]. At intermediate current density (region II), the voltage loss is caused by the electronic and ionic resistance through the electrode. In this region, the voltage decreases linearly with current density, while the activation overpotential reaches a steady value [184]. At high current density

(region III), the cell performance drops dramatically which is attributed to the mass transport limitation in the porous catalyst and GDL layers [185]. To date, numerous models have been established to clarify the polarization behavior of fuel cell. Normally, the relationship between voltage (E_{cell}) and current density (i) at low and intermediate current density region can be described by the empirical equation developed by Sirinivasan et al.[186, 187].

$$E_{cell} = E_0 - blog(i) - Ri \quad (25)$$

$$E_0 = E_r + blogi_0 \quad (26)$$

Er is reversible potential of the cell, i_0 and b are the exchange current density and Tafel slope for ORR, respectively. R in the third terms is the overall resistance of polymer membrane and other electrode components accountable for the linear potential loss, which dominate the intermediate current density region. If take into account of the concenctration overpotential, then the polarization curve over the entire current density range can be semi-empirically expressed in a form as [188]:

$$E_{cell} = E_0 - blog(i) - Ri - mexp(ni) \quad (27)$$

where m and n represents parameters characterizing mass transport effects.

2.4 The influence of nanostructured carbon support on the dispersion and catalytic performance of Pt-based electrocatalysts

Carbon materials have significant impact on the properties of supported noble metal catalysts in terms of the shape, size, distribution, alloyed degree, etc. Moreover, the carbon substrate may also affect the catalytic performance including the mass transfer kinetics, electronic and ionic conductivity, electrochemical active area, and long-term catalytic stability. In order to optimize the fuel cell performance, a great deal of effort has been concentrated on the novel carbon substrate.

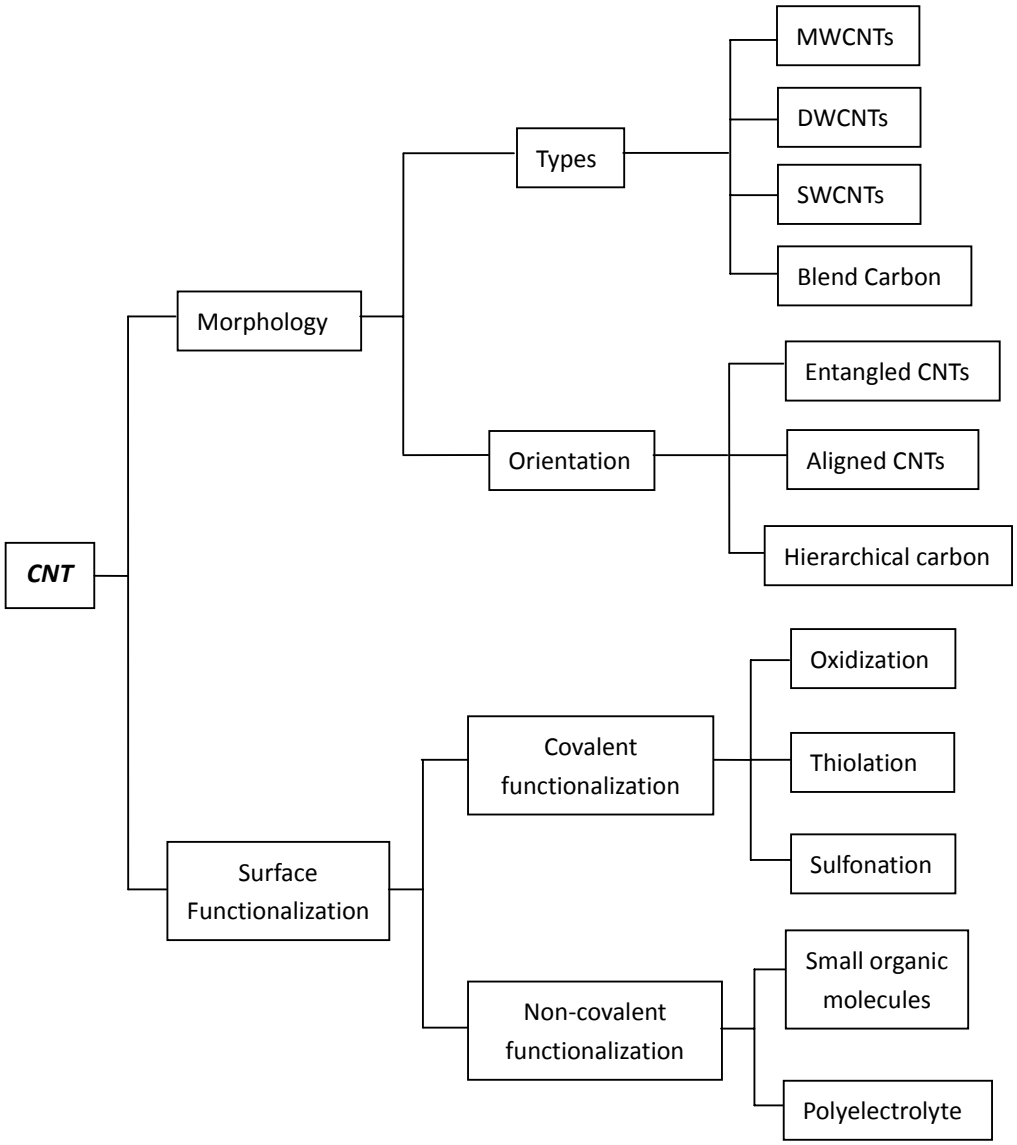

Fig. 2.34 The influence of carbon support on the catalytic performance of Pt-based electrocatalyst.

2.4.1 The effect of morphology

2.4.1.1 The influence of different types of CNTs

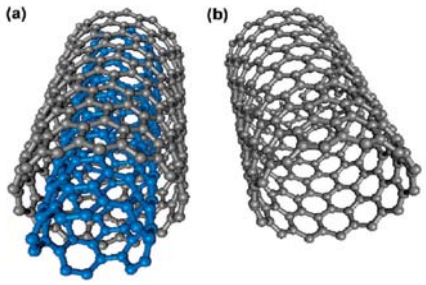

Fig. 2.35 Structure representation of MWCNTs and SWCNTs.

In general, CNTs can be classified as single-walled carbon nano tubes (SWCNTs, 0.7<d<2nm) or multi-walled CNTs (MWCNTs, 1.4<d<150nm). As shown in Fig. 2.35, SWCNTs consist of a single layer of graphene sheet seamlessly rolled-up into a cylindrical tube, while the MWCNTs comprise of coaxially disposed multiple concentric tubes separated by a span of 0.34nm [189]. At present, different types of CNTs including MWCNTs [33, 63, 141, 136], double-walled CNTs (DWCNTs) [71, 74, 169] and SWCNTs [41, 48, 61, 69, 79, 81, 117, 127, 132, 190] are employed as catalyst support for fuel cell.

Li et al. investigated the electrocatalytic performance of PtRu NPs supported on MWCNTs with different lengths and diameters [142]. They noted that the diameter of MWCNTs played a critical role on the MOR catalytic activity. The higher specific activity of PtRu/MWCNTs with large diameter is mainly associated with the rapid electron conduction and high PtRu alloying degree.

One thorough investigation on MWCNTs and SWCNTs supported anode catalyst has been conducted by Wu et al. [127]. Compared with Pt/MWCNTs, superior electrochemical performance of Pt/SWCNTs is evidenced by a slightly lower onset potential and dramatically higher MOR current density. CO stripping voltammograms also confirmed a higher CO-tolerance for Pt/SWCNTs. According to the authors, sound graphitic crystallinity, rich oxygen-containing functional groups and highly mesoporous 3D structure may account for the catalytic activity enhancement.

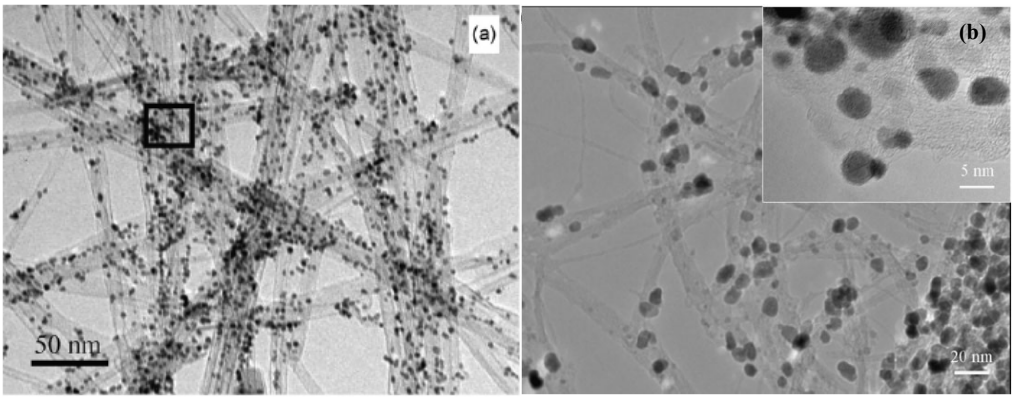

Fig 2.36 TEM images of (a)Pt NPs on DWNTs [69] and (b)Pt NPs on SWNTs[126]

Recently, DWCNTs has emerged as an effective Pt catalyst supporting material.

For instance, Yan's research group prepared MWCNTs and DWCNTs supported PtRu nanocomposite using EG reduction method [71]. TEM observation revealed a minor aggregation of PtRu NPs on MWCNTs, whereas a uniform coverage on DWCNTs because of the larger specific surface area of DWCNTs over MWCNTs (Fig. 2.36(a)). The PtRu/DWNTs exhibited excellent catalytic stability towards oxygen reduction reaction (ORR) examined by ADT tests [74]. The remarkable enhancement of power density was also reported by Li and coworkers using PtRu/DWCNTs as DMFC anode catalyst when compared to PtRu/MWCNTs, PtRu/SWCNTs and PtRu/C [71].

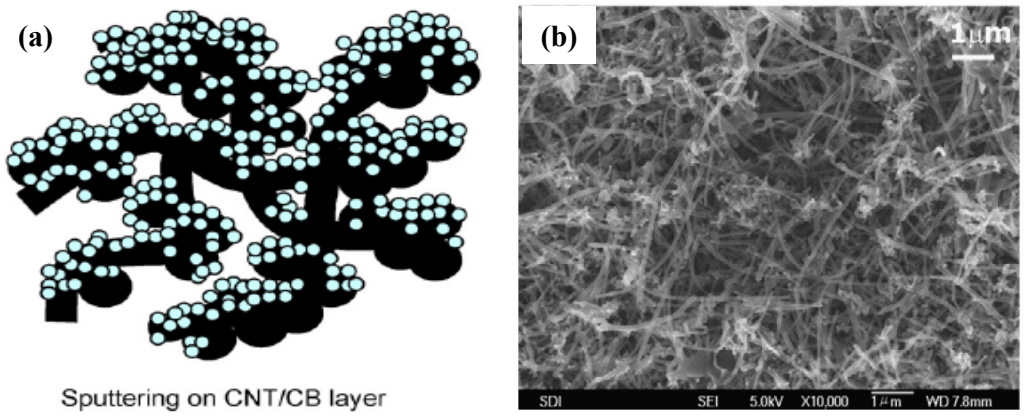

Fig. 2.37 (a)Schematic illustration of Pt-sputtered electrode based on a blend of CB and CNTs. (b)SEM micrographs of the surface of carbon layers (CNT content 50wt%), [157].

To expand two-dimensional Pt/Carbon black thin film structure to 3D porous morphology, Kim et al. proposed a feasible construction by blending spherical carbon black with filamentous MWCNTs [157]. In this new configuration, carbon black spheres are expected to fill into the porous CNTs network, thereby increasing the surface roughness and the accommodation capacity of Pt NPs (Fig. 2.37). ECSA measurements and morphology studies verified the excellent mass-transport property of this novel electrode material. Moreover, Shaijumon et al. studied the effect of blending ratio on the PEMFC performance and proposed an optimum ratio of 1:1. [41]. Similar results were also reached by using a mixture of 50wt% Pt/SWCNTs and 50wt% Pt/CB as both the anode and cathode for PEMFC [54].

2.1.4.2 The effect of CNT alignment

Previous studies on the electrochemical properties of Pt/CNTs nanocomposite suggested that oriented CNTs microstructure may give rise to enhanced catalytic performance [27, 45, 65, 126]. A simple filtration method has been developed to prepare a partially aligned hydrophobic Pt/CNTs composite film [65]. PEMFC using oriented Pt/CNTs cathode provided higher single-cell performance than using carbon black and disordered CNT-film as catalyst support. The increase in PEMFC power density is probably due to the following reason: (i) faster electrons transfer along the tubes than across the tubes. (ii) improved gas permeability and diffusion is expected within the oriented CNT film. (iii) hydrophobic property of ordered CNTs array may facilitate water removal and the mass transportation in the fuel cell compartment.

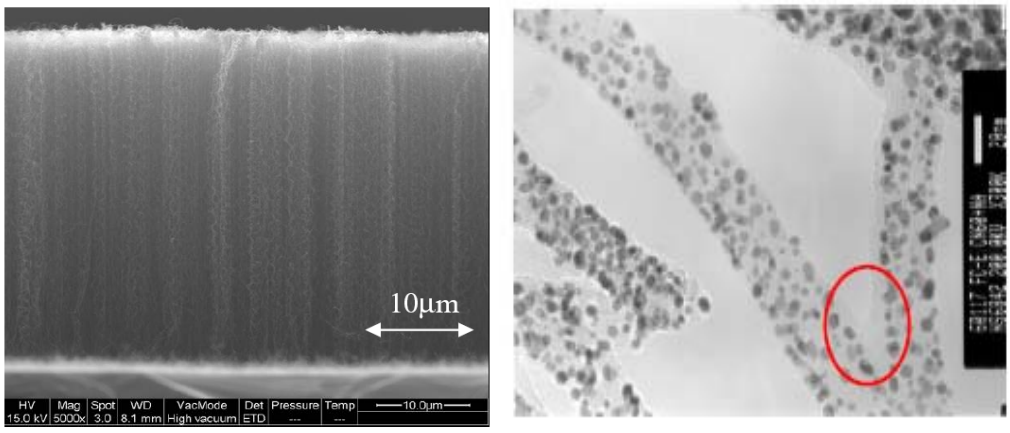

Fig. 2.38 Cross-sectional SEM view and TEM images of aligned Pt/CNTs electrode, the Nafion film covering Pt/CNTs is marked by the red circle [27].

Besides, well-aligned CNTs films were reported to form on the titanium or silicon substrate (Fig. 2.38), followed by the decoration of Pt NPs through either the potential-step or sputtering deposition [27, 126]. Compared with Pt/tangled-CNT and Pt/C, remarkably higher electrocatalytic activity is observed on Pt/aligned-CNT electrode. The obtained higher electron and proton conductivity as well as the current density were likely to be derived from the continuous and direct path within the vertically oriented CNTs.

In an attempt by Ahn et. al, anodic aluminum oxide (AAO) template-directed method was adopted to fabricate 3D PtRu/CNT electrodes for MOR [45]. The cyclic voltammetric studies indicated that the anodic current density of the electrode was ten

times as high as that of PtRu thin-films. Further chronoamperometric test suggested that the highly ordered PtRu/CNT electrode had much slower current degradation rate in comparison with PtRu thin-film. The superior MOR catalytic activity and increased electrochemical stability can be explained in terms of the high specific surface area and uniform distribution of PtRu NPs. This 3D nanostructured electrode with larger electrode/electrolyte contact area and enhanced Pt utilization efficiency could serve as a promising anode for micro-fuel cells.

Directly growth of CNTs on gas diffusion layer has been explored as a novel feasible MEA design to increase the utilization of Pt [15, 111, 163, 191-194]. Earlier attempts to fabricate hierarchically structured carbon hybrid were conducted by S.Désilets's group [191-193]. In a typical procedure, fuel cell backing materials such as carbon cloth (CC) or carbon paper (CP) were first pretreated with ethanol and then immersed into a solution containing sulfonic acid–silicate intermediate (Fig. 2.39a). This surface treatment allows the ion exchange of H^+ for Co^{2+} and Ni^{2+}. Catalytic synthesis of MWCNTs on carbon fiber matrix was carried out by an ohmic heating process, where the Co-Ni particles served as the catalyst and the CNTs growth followed a tip-growth mechanism. Besides, it has been demonstrated that Pt^{2+} can also be attached onto the synthesized CNTs through ion-exchange process. Heat treatment of the adsorbed Pt precursor in an atmosphere of hydrogen and argon yielded ultrafine Pt particles (1.2 ± 0.3nm) located on the external surface of the CNTs (Fig. 2.39b) [194].

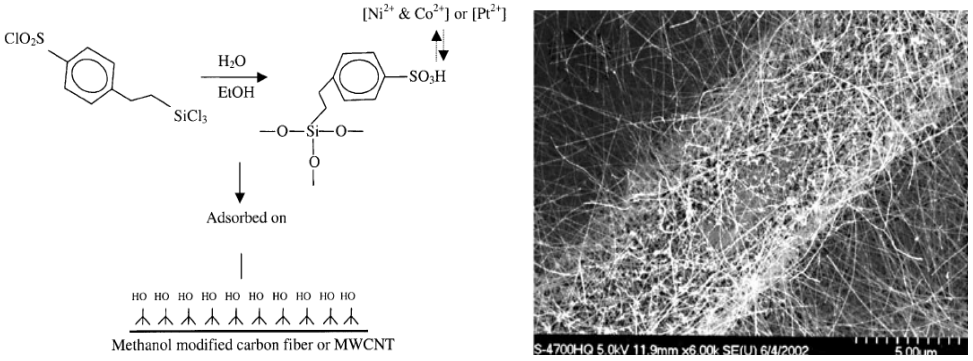

(a) (b)

Fig. 2.39 (a)The surface treatment of carbon fiber with silane derivative and methanol (b) SEM images of CNTs grown on carbon fiber[194].

In another example, microporous CNTs layer was in-situ prepared on carbon paper substrate via a CVD method using a mixture of xylenes and ferrocene as the carbon source and catalyst, respectively [111]. Prior to the deposition of Pt, the in situ synthesized CNTs/CP was initially treated with citric acid to improve the wetting property and was further modified with silane derivative to anchor the noble metal ions. In the ensuing step, Pt NPs with a size range of 1-2nm were homogeneously distributed on MWCNTs/CP via a chemical reduction route. Electrocatalytic activity of the hierarchical Pt/MWCNTs/CP was then assessed by PEMFC testing. The single cell exhibited a high peak power density of 600 and 800mWcm^{-2} with low Pt loadings of 0.3 and 0.5mg cm^{-2}.

Although the MWCNTs have been proven to firmly adhere onto the gas diffusion layer (CC, CP) via the abovementioned methods, electrical contact could be blocked due to the presence of organosilane. To ensure more electrons are accessible to the external circuit of fuel cell, Wang et al. electrodeposited cobalt on CP for CNTs growth [15]. Pt NPs (c.a. 25nm) were subsequently deposited on the CNT/CP composite film. Cyclic voltammetry verified a good electrical contact between MWCNTs and the carbon substrate. Even though the PEMFC performance of the novel MEA design is still lower than the conventional PEMFC, an improved PEMFC performance is expected once the Pt particle size and the yield of CNTs is optimized.

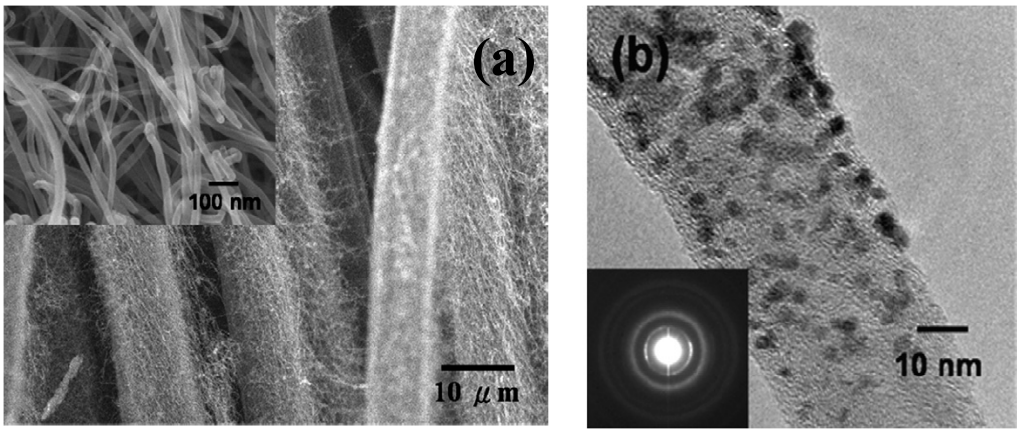

Fig. 2.40 (a) HRSEM showing the CNTs directly grown on carbon cloth.(b) TEM images of PtRu electrocatalysts on the CNTs/CC composite electrode[163].

Hierarchical structured CNTs/CC hybrid was also synthesized by microwave

plasma-enhanced CVD using $CH_4/H_2/N_2$ as precursors [163]. The cyclic voltammetry and AC impedance measurements revealed a fast electron transport and a low resistance of charge transfer on CNTs/CC. Well-dispersed PtRu catalyst with a low loading of 0.4mg cm^{-2} was then sputtered onto the hierarchy nanocarbon support. Microstructure analysis (Fig. 2.40) showed that the thin electrocatalyst layer was very uniform and had good interfacial contact with the proton exchange membrane.

2.4.2 The effect of CNTs surface modification

2.4.2.1 Covalent modification of CNTs

It is generally recognized that the inherently hydrophobic and inert nature of CNTs is unfavorable for the high dispersion of nanoparticles. Hence, it is essential to activate the graphitic structure of CNTs by introducing desirable functional groups with good affinity for metal NPs.

2.4.2.1.1 Oxidation of CNTs

Typically, the aromatic conjugate ring structure of CNTs are oxidized under harsh acidic condition to generate functional groups such as hydroxyl (-OH), carboxyl (-COOH) and carbonyl (-C=O) (Fig.2.41). And a strong chemical interaction is expected to occur between these functional groups and the catalyst metal ions for the high dispersion of NPs in the following step [195].

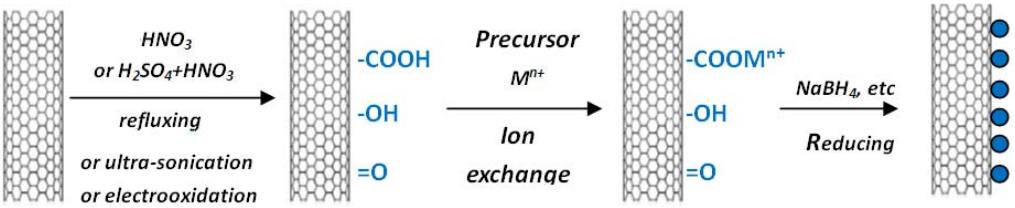

Fig. 2.41 Schematics of synthetic route for anchoring Pt NPs on oxidized-CNT.

For example, Yu et al. refluxed the CNTs in a mixture of HNO_3 + H_2SO_4 to introduce a high density of surface functional groups [196]. Once the Pt^{2+} ions are injected into the reaction system, they may attach onto the functional groups through ion exchange or coordination interaction. Further reduction of these adsorbed precursors yielded well-dispersed Pt NPs on CNTs.

In a method by Chen et al., Pt/CNTs nanohybird was prepared by spontaneous reduction of $PtCl_6^{2-}$ ion as a result of direct redox reactions between $PtCl_6^{2-}$ and

oxygen-containing functional groups at defect sites of CNTs [131]. It has been found that CNTs with high density of defects, which are generated by chemical and electrochemical oxidation treatment, can lead to a more reactive surface than the pristine CNTs. Good dispersion and low agglomeration of the Pt–Ru particles was achieved independent of the Pt–Ru loading. In addition to that, they also came up with a bifunctional mechanism between Pt nanoparticles and oxygen-containing functional groups on CNT, which is responsible for the inhibition of surface poisoning and the increase in long-term cycle stability.

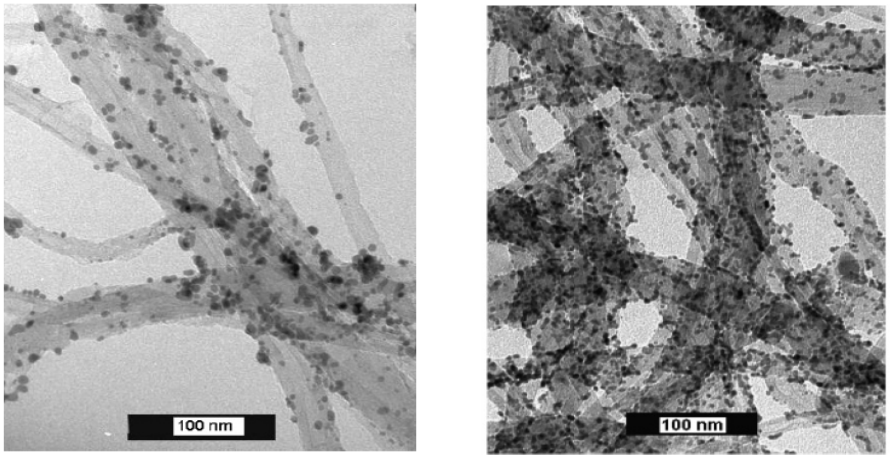

(a) (b)

Fig. 2.42 TEM images of (a) Pt NPs deposited on refluxed CNTs (b) sonochemically treated CNTs (20wt% Pt loading)[64].

With the purpose to increase functional groups on CNTs, a sonochemical-assisted oxidation method was developed by Xing [64]. In a typical process, the purified CNTs were ultrasonicated in a mixture of 8M HNO_3 + 8M H_2SO_4 at 60^{o}C for 2h. The prolonged and repeated ultrasonic treatments can effectively break the CNT aggregates and introduce uniform surface functional groups during the refluxing process. It was asserted that much better dispersion of Pt could be obtained on the sonochemical treated CNTs than on the CNTs treated with conventional refluxing procedures (Fig. 2.42).

By heating the CNTs in a quartz reactor with flowing air, Yoo and coworkers successfully opened the tube ends and intentionally introduced surface defects on the CNTs [31]. Three types of catalysts including the PtRu/defective CNTs,

PtRu/defect-free CNTs and PtRu/fishbone-type CNTs with similar metal loading were prepared by impregnation method using platinum(II) acetylacetonate and ruthenium(III) acetylacetonate as PtRu precursors. Unlike the results reported previously, they argued that the Pt–Ru/defect-free CNTs exhibited the highest catalytic activity in terms of methanol oxidation reaction (MOR) and DMFC performance as the anode. CO stripping voltammograms also revealed its lowest CO oxidation potential among other Pt–Ru catalysts.

2.4.2.1.2 Thiolation of CNTs

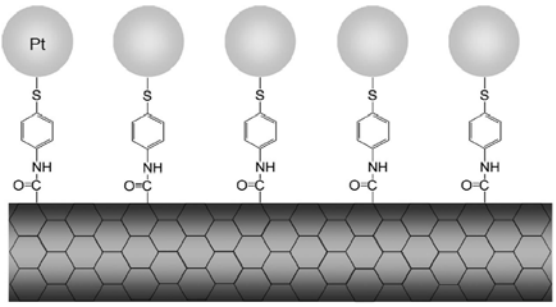

Fig. 2.43 Schematic illustration of Pt NPs supported on thiolated MWCNTs [197]

In addition to the conventional oxidation strategy, thiolation [197, 199] of MWCNT were also reported to achieve highly dispersed Pt NPs. In a method by Kim et al. [197], the thiol group was generated on the CNTs using organic synthetic route based on the formation of amide bond (Fig. 2.43). Extended X-ray analysis fine structure (EXAPFs) and XPS investigation clarified that high dispersion of Pt NPs (1.5nm) could be attributed to the effect of surface thiol groups as anchorage centers, protecting against the agglomeration among Pt NPs. In general, the interaction between metal surface and thiol groups and the formation of Pt-S bond can be written as:

$$RSH + M_n^0 \rightarrow RS^-M^+M_{n-1}^0 + \frac{1}{2}H_2 \quad (28)$$

which enables the change in the electronic state of metal surfaces [198]. These thiolated MWCNTs supported Pt NPs provided enhanced and stable electrocatalytic activity in both methanol oxidation and oxygen reduction reactions.

2.4.2.1.3 Sulfonation of CNTs

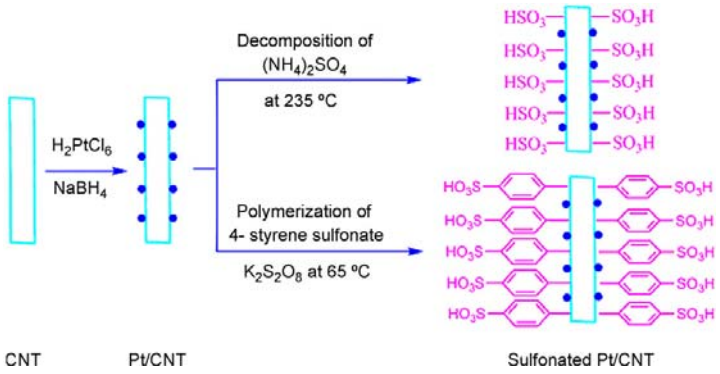

Fig. 2.44 Schematic illustration of two sulfonation routes for Pt/CNT catalysts: (a) decomposition of ammonia sulfonate (b) in situ radical polymerization of 4-styrenesulfonate [8].

Du et al. [8] reported two post-treatment procedures to graft the sulfonic acid groups on the as-prepared Pt/CNT catalysts by either thermal decomposition of $(NH_4)_2SO_4$ or radical polymerization of 4-styrenesulfonate (Fig. 2.44). They claimed that the second sulfonation approach could yield better performance than that with the unsulfonated counterpart, mainly because of the easier access with protons and well dispersed distribution of the sulfonated Pt/CNT catalysts. Half-cell study indicated that there existed an optimal sulfonation degree around 8.2wt%, while the excessive sulfonation of the catalyst may exert an adverse effect on the fuel cell performance.

2.4.4.2 Noncovalent modification of CNTs

The covalent modification methods realized improved dispersion of NPs, but they inevitably generate surface defects and cause severe structural damage on the CNTs. As a result, it may lead to the degradation of electrical conductivity and corrosion resistance of CNTs. To circumvent these negative effects, substantial efforts have been devoted to noncovalent functionalization of CNTs. As a versatile strategy, it not only preserves the intrinsic structure of CNTs, but achieves the tailored properties of the hybrid material [52, 200].

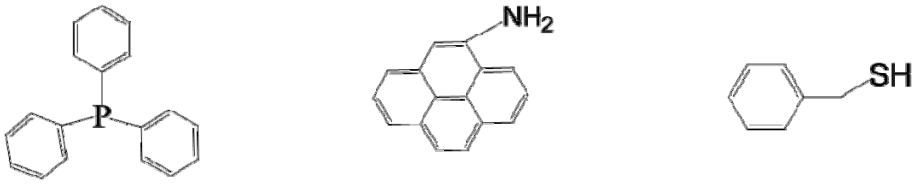

Fig. 2.45 Molecular Formula of (a) triphenylphosphine (b) 1-amninopyrene (c) benzyl

mercaptan

2.4.4.2.1 Noncovalent modification of CNTs with small molecules

Surfactants, particularly aromatic small molecule such as triphenylphosphine (PPh_3) [66], 1-amninopyrene (1-AP) [52, 83] and benzyl mercaptan [73, 165, 197] (Fig. 2.45) have been employed as bifunctional interlinker to immobilize well-dispersed Pt or PtRu nanoclusters on CNTs. For example, Yang et al [165] reported an efficient route to modify CNTs with benzyl mercaptan, where the benzene moieties were strongly adsorbed on the CNTs through π-π stacking interaction, while the mercaptan group could coordinate with Pt NPs and increase the interaction between Pt and CNTs. Further cyclic voltammetric investigation revealed that the as-prepared Pt/CNT composites showed higher electrocatalytic activity and enhanced CO tolerance in comparison with Pt/XC and Pt/CNT [73, 197]. In a similar manner, 1-AP molecule with a pyrenyl group and an amino group is reported to be irreversibly adsorbed onto hydrophobic sidewalls of MWCNTs [52, 83]. Under slight acidic condition, the surfaces of modified MWCNTs become positively charged, which facilitate the self-assembly of $PtCl_6^{2-}$ and Ru^{3+} precursors through electrostatic interaction [83]. TEM images shows that bimetallic PtRu nanoclusters with mean particle size of 2nm were evenly deposited onto 1-AP functionalized MWCNTs by a microwave-assisted polyol process. The obtained 1-AP functionalized MWCNTs supported PtRu electrocatalyst exhibited larger electrochemical surface area, higher catalytic activity and enhanced stability for methanol oxidation than those on acid-oxidized MWCNTs and XC-72 carbon.

However, the ligand and capping agent as insulators or electron tunneling barriers may poison the catalyst surface and decrease the electrocatalytic activity. Hence, they are normally removed through a thermal decomposition process, which is fairly difficult to perform while still retaining the particle's size and shape [201].

2.4.4.2.1 Noncovalent modification of CNTs with polyelectrolyte

Recently, noncovalent functionalization of CNTs with polyelectrolyte have been extensively investigated and exploited as catalyst supports for fuel cell. By using polymer wrapping technique, positively charged poly (diallyldimethylammonium

chloride) (PDDA) [57, 80] and negatively charged poly (sodium 4-styrenesulfonate) (PSS) [69] were adsorbed on the surface of CNTs, respectively (Fig. 2.46). Controllable decoration of Pt NPs was achieved using either PDDA or PSS modified CNT as building block. In addition, a novel route towards the self-assembly of cetyltrimethylammonium bromide (CTAB) stabilized Pt nanocubics on PSS-modified CNTs has been demonstrated via electrostatic interaction [11].

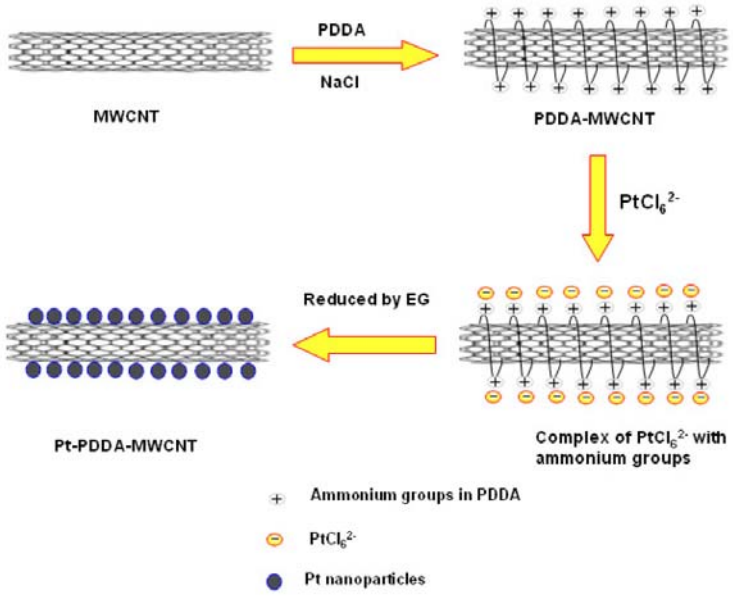

Fig. 2.46 In-situ synthesis of Pt NPs on PDDA-functionalized MWCNTs [80]

Polyethyleneimine (PEI), as a cationic surfactant, has been reported to achieve the surface functionalization of noble metal NPs [202]. For example, Bai et al. presented a clean and efficient route to synthesize monodispersed Pt NPs through UV photoreduction method, where PEI served both as a reducing agent and capping agent [151]. Moreover, the amino-rich PEI chain is known to be effectively attached on the sidewalls of CNTs via physisorption [203]. Construction of one-dimensional CNT/metal NPs (metal=Au, Pt, Pd, Ag) heterogeneous nanostructures has been realized by means of chemical reduction of PEI-meditated noble metal precursors [55, 203, 204].

2.5 The promoting effect of coupling secondary metal element on electrocatalysis

One of the disadvantages of using pure Pt electrocatalyst is that the catalytic

performance may suffer from the carbon monoxide poisoning during the electrooxidation of small organic molecules [17, 18]. In the pursuit of more stable catalytic performance, Pt based binary catalyst have been proven as promising anode candidates for DMFCs and DEFCs.

2.5.1 PtRu binary catalyst for methanol oxidation

The mechanism of methanol oxidation on the Pt surface has been extensively studied for decades, the primary process of which involves the following steps [205]: (1) methanol adsorption (2) C-H bond activation (methanol dissociation) (3) water adsorption (4) water activation (5) CO oxidation. The formation of Pt-OH by water is a key step for the oxidative removal of adsorbed CO. Unfortunately, high potential up to 0.7V (vs RHE) is required to generate OH species on Pt surface to effectively oxidize CO.

$$\mathrm{Pt} + \mathrm{CH_3OH} \rightarrow \mathrm{Pt} - (\mathrm{CH_3OH})_{\mathrm{ads}} \tag{29}$$

$$\mathrm{Pt} - (\mathrm{CH_3OH})_{\mathrm{ads}} \rightarrow \mathrm{Pt} - (\mathrm{CH_3O})_{\mathrm{ads}} + \mathrm{H^+} + \mathrm{e^-} \tag{30}$$

$$\mathrm{Pt} - (\mathrm{CH_3O})_{\mathrm{ads}} \rightarrow \mathrm{Pt} - (\mathrm{CH_2O})_{\mathrm{ads}} + \mathrm{H^+} + \mathrm{e^-} \tag{31}$$

$$\mathrm{Pt} - (\mathrm{CH_2O})_{\mathrm{ads}} \rightarrow \mathrm{Pt} - (\mathrm{CHO})_{\mathrm{ads}} + \mathrm{H^+} + \mathrm{e^-} \tag{32}$$

$$\mathrm{Pt} - (\mathrm{CHO})_{\mathrm{ads}} \rightarrow \mathrm{Pt} - (\mathrm{CO})_{\mathrm{ads}} + \mathrm{H^+} + \mathrm{e^-} \tag{33}$$

Because incorporation of second metal element can provide oxygenated species at lower potentials, binary Pt-based alloys including PtRu, PtSn, PtW, PtMo, etc., have been investigated towards methanol oxidation [206]. Among them, PtRu seems to be the most active and the state-of-the art anode catalyst for DMFCs.

Table. 2.3 Summary of the reported Pt–Ru/C catalysts synthesized by different preparation routes of the impregnation method [114]

Catalyst	Precursor/reducing agent	Particle size (nm)	Activity	Measurement protocol
20t% $Pt_{75}Ru_{25}$	H_2PtCl_6, $RuCl_3$/HCOOH	2–5	300 mA cm^{-2} at 400 mV, 1 mg cm^{-2}	A single DMFC, 2 M CH_3OH, O_2, 70 °C
20% $Pt_{50}Ru_{50}$	H_2PtCl_6, $RuCl_3$/$NaBH_4$	3.7 ± 1.0	4 mA cm^{-2} at 200 mV (vs. SCE)	CV (vitreous carbon) 1 M H_2SO_4 + 2 M CH_3OH, RT
30% $Pt_{67}Ru_{33}$	H_2PtCl_6, $RuCl_3$/H_2	1.5 ± 0.5	65 mA mg^{-1} at 400 mV (vs. RHE), 0.25 mg cm^{-2}	Polarization (glassy carbon) 0.5 M H_2SO_4 + 2 M CH_3OH, 60 °C
50% $Pt_{50}Ru_{50}$	$Na_6Pt(SO_3)_4$, $Na_6Ru(SO_3)_4$/H_2	~2	60 mA mg^{-1} at 400 mV (vs. RHE), 2 mg cm^{-2}	Polarization (carbon paper) 1 M H_2SO_4 + 1.5 M CH_3OH, 65 °C
30% $Pt_{50}Ru_{50}$	$Pt(NH_3)_2(NO_2)_2$, $RuNO(NO_3)_x$/H_2 + N_2	3.1 ± 0.5	8 mA mg^{-1} at 400 mV (vs. RHE), 0.06 mg cm^{-2}	Polarization (glassy carbon), 0.5 M H_2SO_4 + 1 M CH_3OH, 60 °C
50% $Pt_{50}Ru_{50}$	$[Pt(CO)_2]_x$, $Ru_3(CO)_{12}$/none	2.5 ± 0.45	85 mA mg^{-1} at −200 mV (vs. MMS), 1 mg cm^{-2}	Polarization (carbon paper) 1 M H_2SO_4 + 1.5 M CH_3OH, 65 °C
30% $Pt_{50}Ru_{50}$	(η-C_2H_4)(Cl)Pt(μ-Cl)$_2$ Ru(Cl)(η^3: η-2,7-dimethyloctadienediyl)/H_2	3.5–5.4	120 mA cm^{-2} at 400 mV, 2.43 mg cm^{-2}	A single DMFC, 1 M CH_3OH, air, 90 °C

Table. 2.4 Summary of the reported Pt–Ru/C catalysts synthesized by different preparation routes of the colloidal method [114]

Catalyst	Precursor	Reducing agent/stabilizer	Particle size (nm)	Activity	Measurement protocol
30% $Pt_{50}Ru_{50}$	H_2PtCl_6, $RuCl_3$	H_2O_2 + H_2/none	3–4	200 mA cm^{-2} at 400 mV (vs. RHE), 2 mg cm^{-2}	Polarization (gas diffusion electrode) 1.5 M H_2SO_4 + 2 M CH_3OH (vapor), 60 °C
20% $Pt_{50}Ru_{50}$	$PtCl_2$, $RuCl_3$	$NOct_4[BEt_3H]$/itself	1.5 ± 0.4	20 mA mg^{-1} at 400 mV (vs. RHE), 0.014 mg cm^{-2}	Potentiostatic (glassy carbon) 0.5 M H_2SO_4 + 2 M CH_3OH, 60 °C
20% $Pt_{50}Ru_{50}$	$Pt(acac)_2$, $Ru(acac)_3$	$Al(CH_3)_3$/itself	1.5 ± 0.5	27 mA mg^{-1} at 400 mV (vs. RHE), 0.014 mg cm^{-2}	Potentiostatic (glassy carbon) 0.5 M H_2SO_4 + 2 M CH_3OH, 60 °C
30% $Pt_{50}Ru_{50}$	$Pt(dba)_2$, Ru(COD)(COT)	$(C_8H_{17})_4NDCTA$/itself	<2	18 mA mg^{-1} at 400 mV (vs. RHE), 0.007 mg cm^{-2}	Potentiostatic (glassy carbon) 0.5 M H_2SO_4 + 0.5 M CH_3OH, 60 °C
27% $Pt_{67}Ru_{33}$	H_2PtCl_6, $RuCl_3$	1-Propanol/PVP	2–3.2	220 mA mg^{-1} at 400 mV, 0.27 mg cm^{-2}	A single DMFC, 1.5 M CH_3OH, O_2, 80 °C
20% $Pt_{50}Ru_{50}$	H_2PtCl_6, $RuCl_3$	Ethylene glycol/itself	3–6	1.1 mA at 400 mV (vs. SCE), 46% decay after 1 h	Chronoamperometry (vitreous carbon) 1 M H_2SO_4 + 2 M CH_3OH, RT
30% $Pt_{67}Ru_{33}$	H_2PtCl_6, $RuCl_3$	Ethylene glycol/itself	2.0 ± 0.3	300 mA cm^{-2} at 400 mV, 2 mg cm^{-2}	A single DMFC, 1.0 M CH_3OH, O_2, 90 °C

Studies of the PtRu alloy as electrocatalyst for MOR can be traced back to 1960s when binary PtRu and PtMo were found to have enhanced catalytic MOR performance than pure Pt black under acidic condition [207]. Early research work mainly focused on the bulk Pt alloy catalyst for MOR. In 1987, the carbon supported highly dispersed PtRu bimetallic catalyst was reported [208]. Since then, the optimization of PtRu/C through preparation procedures and composition control became a hot subject of numerous studies. The catalytic activity of PtRu/C catalyst, correlated to the properties of both alloy and support, strongly depends on the choice of the precursors, the deposition techniques, the supports, the electrode fabrication techniques, and so forth. The common criteria for a high-performance Pt-Ru/C catalyst are: i) narrow size distribution; ii) uniform composition; iii) a fully alloyed

degree; and iv) high dispersion on the carbon support. Based on these criteria, the cost-effective preparation techniques via impregnation and colloidal routes have been developed and show promising results through distinguishable synthetic procedures and conditions, as listed in Table.2.3 and Table.2.4 [113].

According to a bifunctional mechanism [209, 210], the chemisorption of oxygenated species happens much more easily on Ru sites rather than Pt sites during MOR. Water dissociation occurs on Ru sites with the formation of $Ru(OH)_{ads}$ species at a potential as low as 0.2 V vs. RHE, while methanol dehydrogenation occurs on Pt sites at a potential below 0.2 V vs. RHE. The active Pt sites dehydrogenate the chemisorbed methyl moiety in consecutive steps to yield Pt–CO_{ads} fragments, which can be effectively removed by the oxygen-containing species on the neighboring Ru atom [209, 210].

$$Ru + H_2O \rightarrow Ru - (H_2O)_{ads} \tag{34}$$

$$Ru - (H_2O)_{ads} \rightarrow Ru(OH)_{ads} + H^+ + e^- \tag{35}$$

$$Ru - (OH)_{ads} + Pt - (CO)_{ads} \rightarrow Pt + Ru + CO_2 + H^+ + e^- \tag{36}$$

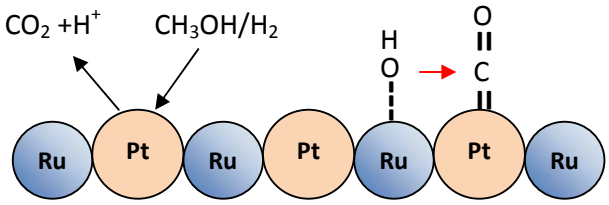

Fig. 2.47 Schematics of bifunctional mechanism [7]

In addition, a ligand (or electronic) effect may play synergistic role in enhancing the CO tolerance of the binary PtRu catalyst [211, 212]. Iwasita et al.[213] postulated that CO is less strongly adsorbed on PtRu alloy electrode through a reduction in the back π bonding from Pt to the CO π* orbital. The reduction in π back-bonding will also lead to a higher positive charge on the carbon atom, rendering it more liable to nucleophilic attack by water, and permitting CO oxidation at lower potentials. Nevertheless, the consequences of the ligand effect and the bifunctional mechanism for CO oxidation on PtRu alloy have been debated extensively in the literature. Further investigation by Lu using CV, temperature programmed desorption (TPD) as

well as radioactive labeling revealed that ligand effect only played a minor role in improvement of CO tolerance as compared with bifunctional mechanism [214].

Another promoting effect referred to OH spillover was also suggested to explain MOR enhancement on PtRu and PtSn. Davies et al. [215] and Stamenkovic et al. [216] proposed that the OH species formed on Ru or Sn might spillover onto the neighboring Pt sites and facilitate CO oxidation. Even though OH is preferentially adsorbed on Ru or Sn than on Pt, the situation may be altered in the presence of water. Molecular dynamics calculations provided evidence that OH species formed on Ru could easily attract hydrogen from a water molecule on a neighboring Pt atom, leading to the effective transfer of OH to Pt site [217].

Besides mechanism study, numerous research studies have been devoted to optimize the composition of carbon supported PtRu catalysts towards MOR. And the current consensus has been reached that the optimum atomic ratio of Pt/Ru is 1:1[19, 218].

2.5.2 PtSn binary catalyst for ethanol oxidation

Table. 2.5 DEFCs performance with different anode catalyst [219].

Catalyst	Open circuit potential(mV)	Maximum power density
Pt	547	10.85
PtRu(1:1)	677	28.54
PtSn(1:1)	811	52.22
PtRuW(1:1:1)	698	38.54
PtRuMo(1:1:1)	720	31.19

Conversely to methanol oxidation, PtSn/C exhibited better performance than PtRu/C towards ethanol oxidation. As shown in Table 1, the DEFCs with PtSn anode catalyst showed larger OCV and higher power density than that with PtRu catalyst [219]. Earlier research work by Lamy and coworkers verified that alloying Pt with second metal, Sn in particular, could significantly improve the ethanol oxidation kinetics and mitigate the CO poisoning phenomenon [20, 220, 221]. In several related studies, carbon supported PtSn with different Sn content has been prepared and investigated for ethanol electrooxidation. For instance, Zhou et al. found that Pt:Sn

with molar ratio ranged from 1:1 to 2:1 showed a superior performance[222], and very similar results were reported by Spinacé and coworkers [223].

Further studies on the the carbon supported Pt-Sn catalysts reveal that the relative amount of Pt-Sn alloy phase and SnO_2 is critical to the electrochemical activity of ethanol oxidation. Jang et al.[224] compared the catalytic activity of partially alloyed Pt-Sn catalyst with that of non-alloyed $PtSnO_x$ catalyst. According to the electrochemical test results, they deduced that the $PtSnO_x$ is more favorable for ethanol oxidation since SnO_2 can offer oxygen species conveniently to remove poisoning intermediates in the vicinity of Pt, while the unchanged the lattice structure is beneficial for chemiethanol adsorption. However, controversial results was reached by Colmenares et al.[225] who suggested that high alloying degree of PtSn is more appropriate for ethanol oxidation.

Regarding to the promoting effect of Sn, the universally accepted bifunctional mechanism and ligand effect can also be applied to explain the enhancement of catalytic performance as well as CO tolerance [226, 227]. Based on the bifunctional mechanism, Sn is able to activate water at lower potentials, which produce adsorbed oxygen-containing species to remove the adsorbed CO and therefore liberate Pt active site. Besides, the ligand effect has also been found to modify the electronic properties of Pt by donating large electron density. Chemisorption of CO on Pt involves the donation of an electron pair from the σ^* anti-bonding orbital of CO to unoccupied 5d-orbitals of Pt. X-ray adsorption studies validated that alloying Sn with Pt caused partial filling of Pt 5d bands, resulting in the decrease in the binding energy of CO bond on active Pt surface. Therefore, the weaker chemisorption of CO combined with the easier generation of OH species on Sn sites facilitate the CO oxidation and thus enhance the catalytic activity of EOR on PtSn alloy [228, 229].

Although great achievements have been made in exploring more active binary catalyst other than pure Pt in the last three decades, many unanswered questions are. The ideal composition and distribution of second element in Pt is a subject of debate. Another controversial issue is raised about the optimum oxidation state of Ru and Sn in the electrocatalyst system. Furthermore, the stability of PtRu and PtSn bimetallic

alloy is still a concern, since the Ru/Sn leaching during the fuel cell operation has been well documented in the literature [230].

Reference

[1] Litster, S.; Mclean, G. *J. Power Sources* **2004**, *130*, 61-76.

[2] Yu, X.; Ye, S. *J. Power Sources* **2007**, *172*, 133-144.

[3] Hepel, M.; Dela, I.; Hepel, T.; Luo, J.; Zhong, C.J. *Electrochim. Acta* **2007**, *52*, 5529.

[4] Yu, J.S.; Kang, S.; Yoon, S.B.; Chai, G. *J. Am.Chem. Soc.* **2002**, *124*, 9382.

[5] Xue, X.; Ge, J.; Tian, T.; Liu, C.; Xing, W.; Lu, T. *J. Power Sources* **2007**, *172*, 560-569.

[6] Lobato, J.; Canizares, P.; Rodrigo, M.A.; Linares, J.J. *Appl. Catal., B* **2009**, *91*, 269-274.

[7] Zhang, J.J. (ed.) PEM fuel cell electrocatalysts and catalysts layers, Springer, London, **2008**, Chap 10.

[8] Du, C. Y.; Zhao, T. S.; Liang, Z. X. *J. Power Sources*. **2008**, *176*, 9-15.

[9] M. M. Shaijumon, S. Ramaprabhu, *Appl. Phys. Lett.* **2006**, *88*, 253105.

[10] Jafri, R.I.; Ramaprabhu, S. *In. J. Hydrogen Energy* **2010**, *35*, 1339-1346.

[11] Liu, Z.; Lin, X.; Lee, J.Y.; Zhang, W.; Han, M.; Gan, L.M. *Langmuir* **2002**, *18*, 4054-4060.

[12] Bommersbach, P.; Chaker, M.; Mohamedi, M.; Guay, D. *J. Phys. Chem. C* **2008**, *112*, 14672-14681.

[13] Choi, W.C.; Woo, S.I.; Jeon, M.K.; Sohn, J.M.; Kim, M.R.; Jeon, H.J. *Adv. Mater.* **2005**, *17*, 446-451.

[14] Iijima, S. *Nature*, **1991**, *354*, 56-58.

[15] Wang, C.; Waje, M.; Wang, X.; Tang, J.M.; Haddon, R.T.C.; Yan, Y.S. *Nano Letters* **2004**, *4*, 345-348.

[16] Yang, W.; Wang, X.; Yang, F.; Yang, C.; Yang, X. *Adv. Mater.* **2008**, *20*, 2579-2587.

[17] Gottesfeld, S.; Pafford, J. *J. Electrochem. Soc.* **1988**, *135*, 2651-2652.

[18] Beden, B.; Lamy, C.; Bewick, A.; Kumimatsu, K.; *J Electroanal. Chem.* **1981**,

121, 343-347.

[19] Bock, C.; Paquet, C.; Couillard, M.; Botton, G.A.; MacDougall, B.R. *J. Am. Chem. Soc.* **2004**, *126*, 8028-8037.

[20] Godoi, D.R.M.; Perez, J.; Villullas, H.M. *J. Power Sources* **2010**, *195*, 3394-3401.

[21] Cui, Z.; Liu, C.; Liao, J.; Xing, W. *Electrochim. Acta* **2008**, *53*, 7807-7811.

[22] Shao, Y.; Kou, R.; Wang, J.; Kwak, J.H.; Viswanathan, V.; Wang, Y.; Liu, J.; Lin, Y. *ECS Transactions* **2008**, *16*, 361-366.

[23] Matsumori, H.; Takenaka, S.; Matsune, H.; Kishida, M. *Appl. Catal., A* **2010**, *373*, 176-185.

[24] de Miguel, S.R.; Roman-Martinez, M.C.; Jablonski, E. L.; Fierro, J.L.G.; Cazorla-Amor os, D.; Scelza O.A. *J. Catal.* **1999**, *184*, 514–525.

[25] Roman-Martinez, M.C.; Macia-Agullo, J.A.; Vilella, I.M.; Cazorla-Amoros, J. D.; Yamashita, H.; *J. Phys. Chem. C* **2007,** *111,* 4710-4716.

[26] Che, G.; Lakshmi, B.B.; Martin, C.R.; Fisher, E.R. *Langmuir* **1999**, *15*, 750-758.

[27] Hatanaka, T.; Nakanishi, H.; Matsumoto, S.; Morimoto, Y. *ECS Transactions* **2006,** *3*, 277-284.

[28] Vijayaraghavan, G.; Stevenson, K. J. *ECS Transactions* **2008,** *6*, 43-50.

[29] Matsumori, H.; Takenaka, S.; Matsune, H.; Kishida, M. *Transactions* **2009,** *25*, 689-696.

[30] Takenaka, S.; Matsumori, H.; Matsune, H.; Tanabe, E.; Kishida, M. *J. Electrochem. Soc.* **2008**, *155*, B929-B936.

[31] Yoo, E.; Okada, T.; Kizuka, T.; Nakamura, J. *J. Power Sources* **2008**, *180*, 221-226.

[32] Viswanathan, B. *Catal. Today* **2009**, *141*, 52-55.

[33] Lin, Y.; Cui, X.; Yen, C.H.; Wai, C.M. *Langmuir* **2005**, *21*, 11474-11479.

[34] Rajesh, B.; Thampi, K.R.; Bonard, J.-M.; Xanthopoulos, N.; Mathieu, H.J.; Viswanathan, B. *J. Phys. Chem. B* **2003**, *107*, 2701-2708.

[35] Joo, S.H.; Pak, C.; Kim, E.A.; Lee, Y.H.; Chang, H.; Seung, D.; Choi, Y.S.; Park, J.-B.; Kim, T.K. *J. Power Sources* **2008**, *180*, 63-70.

[36] Carmo, M.; Paganin, V.A.; Rosolen, J.M.; Gonzalez, E.R. *J. Power. Sources* **2005**, *142*, 169-176.

[37] Ocampo, A.L.; Miranda-Hernández, M.; Morgado, J.; Montoya, J.A.; Sebastian, P.J. *J. Power. Sources* **2006**, *160*, 915-924.

[38] Onoe, T.; Iwamoto, S.; Inoue, M. *Catal. Commun.* **2007**, *8*, 701-706.

[39] Li, X.; Hsing, L.-M. *Electrochim. Acta* **2006**, *51*, 5250-5258.

[40] Xu, J.; Hua, K.; Sun, G.; Wang, C.; Lv, X.; Wang, Y. *J. Electrochem. Commun.* **2006**, *8,* 982-986.

[41] M. M. Shaijumon, S. Ramaprabhu, *Appl. Phys. Lett.* **2006**, *88*, 253105.

[42] Prabhuram, J.; Zhao, T.S.; Liang, Z.X.; Chen, R. *Electrochim. Acta* **2007**, *52*, 2649-2656.

[43] Gao. G.; Yang, G.; Xu, M.; Wang, C.; Xu, C.; Li, H. *J. Power Sources* **2007**, *173*, 178-182.

[44] de Moraes, I.R.; Matsubara, E.Y.; Rosolen, J.M. *Electrochem. Solid-State Lett.* **2008**, *11*, K109-K112.

[45] Ahn, H.J.; Moon, W.J.; Seong, T.Y.; Wang, D. *Electrochem.Commun.* **2009**, *11*, 635-638.

[46] Yoo, E.J.; Takano, Y.; Nakamura, J. *ECS transaction*s **2009**, *25*, 899-905.

[47] Kauffman, D.R.; Tang, Y.; Kichambare, P.D.; Jackovitz, J.F.; Star, A. *Energy Fuels* **2010**, *24*, 1877-1881.

[48] Golikand, A.N.; Lohrasbi, E.; Maragheh, M.G.; Asgari, M. *J. Appl. Electrochem.* **2009**, *39*, 1443-1449.

[49] Huang, T.; Liu, J.; Li, R.; Cai, W.; Yu, A. *Electrochem.Commun.* **2009**, *11*, 643-646.

[50] Pang, H.L.; Lu, J.P.; Chen, J.H.; Huang, C.T.; Liu, B.; Zhang, X.H. *Electrochim. Acta* **2009**, *54*, 2610-2615.

[51] Zhou, Y.; Gao, Y.; Liu, Y.; Liu, J.; *J. Power Sources*. **2010**, *195*, 1605-1609.

[52] Li, X.; Liu, Y.; Fu, L.; Cao, L.; Wei, D.; Wang, Y.; *Adv. Funct. Mater* **2006**, *16,* 2431-2437.

[53] Kumar, M.K.; Ramaprabhu, S. *J. Phys. Chem.* B **2006**, *110*, 11291-11298.

[54] Reddy, A.L.M.; Ramaprabhu, S. *J. Phys. Chem. C* **2007**, *111*, 16138-16146.

[55] Hu, X.; Wang, T.; Wang, L.; Guo, S.; Dong, S. *Langmuir* **2007**, *23*, 6352-6357.

[56] Reddy, A.L.M.; Rajalakshmi, N.; Ramaprabhu, S. *Carbon* **2008**, *46*, 2-11.

[57] Du, N.; Zhang, H.; Wu, P.; Yu, J.; Yang, D. *J. Phys. Chem.* C **2009**, *113*, 17387 - 17391.

[58] Halder, A.; Sharma, S.; Hegde, M.S.; Ravishankar, N. *J. Phys. Chem. C* **2009**, *113*, 1466-1473.

[59] Guo, D.-J.; Qiu, X.-P.; Chen, L.-Q.; Zhu, W.-T. *Carbon* **2009**, *47*, 1680-1685.

[60] Wang, Y.; Ren, J.; Deng, K.; Gui, L.; Tang, Y. *Chem. Mater.* **2000**, *12*, 1622-1627.

[61] Lordi, V.; Yao, N.; Wei, J. *Chem. Mater.* **2001**, *13*, 733-737.

[62] Matsumoto, T.; Komatsu, T.; Nakano, H.; Arai, K.; Nagashima, Y.; Yoo, E.; Yamazaki, T.; Kijima, M.; Shimizu, H.; Takasawa, Y.; Nakamura, *Catal. Today* **2004**, *90*, 277-281.

[63] Li, W.; Liang, C.; Zhou, W.; Qiu, J.; Li, H.; Sun, G.; Xin, Q. *Carbon* **2004**, *42*, 436-439.

[64] Xing, Y. *J. Phys. Chem. B* **2004**, *108*, 19255-19259.

[65] Li, W.; Wang, X.; Chen, Z.; Waje, M.; Yan, Y. *Langmuir* **2005**, *21*, 9386-9389.

[66] Mu, Y.; Liang, H.; Hu, J.; Jiang, L.; Wan, L. *J. Phys. Chem. B* 2005, **109** 22212-22216.

[67] Liao, S.; Holmes, K.-A.; Tsaprailis, H.; Birss, V. I. *J. Am. Chem. Soc.* **2006**, *128*, 3504-3505.

[68] Wang, Y.; Xu, X.; Tian, Z.; Zong, Y.; Cheng, H.; Lin, C. *Chem. Eur. J.* **2006**, *12*, 2542-2549.

[69] Kongkanand, A.; Vinodgopal, K.; Kuwabata, S.; Kamat, P. V. *J. Phys. Chem.* B **2006**, *110*, 16185-16188.

[70] Jeng, K.-T.; Chien, C.-C.; Hsu, N.-Y.; Yen, S.-C.; Chiou, S.-D.; Lin, S.-H.; Huang, W.-M. *J. Power Sources* **2006**, *160*, 97-104.

[71] Li, W.; Wang, X.; Chen, Z.; Waje, M.; Yan, Y. *J. Phys. Chem. B* **2006**, *110*, 15353-15358.

[72] Cao, L,; Scheiba, F.; Roth, C.; Schweiger, F.; Cremers, C.; Stimming, U.; Fuess, H.; Chen, L.; Zhu, W.; Qiu, X. *Angew. Chem.* **2006**, *118*, 5441-5445.

[73] Yang, G.-W.; Gao, G.-Y.; Zhao, G.-Y.; Li, H.-L. *Carbon* **2007**, *45*, 3036-3041.

[74] Chen, Z.; Deng, W.; Wang, X.; Yan, Y. *ECS transaction*s **2007**, *11*, 1289-1299.

[75] Wang, J.; Xi, J.; Bai, Y.; Shen, Y.; Sun, J.; Chen, L.; Zhu, W.; Qiu, X. *J. Power Sources* **2007**, *164*, 555-560.

[76] Tang, J.M.; Jensen, K.; Waje, M.; Li, W.; Larsen, P.; Pauley, K.; Chen, Z.; Ramesh, P.; Itkis, M.E.; Yan, Y.; Haddon, R.C. *J. Phys. Chem. B* **2007**, *111*, 17901-17904.

[77] Jeng, K.-T.; Chien, C.-C.; Hsu, N.-Y.; Huang, W.-M.; Chiou, S.-D.; Lin, S.-H.; *J. Power Sources* **2007**, *164*, 33-41.

[78] Guo, J.; Sun, G.; Sun, S.; Yan, S.; Yang, W.; Qi, J.; Yan, Y.; Xin, Q. *J. Power Sources* **2007**, *168*, 299-306,

[79] Michel, M.; Taylor, A.; Sekol, R.; Podsiadlo, P.; Ho, P.; Kotov, N.; Thompson, L. *Adv. Mater.* **2007**, *19*, 3859-3864.

[80] Wang, S.; Jiang, S.P.; Wang, X. *Nanotechnology* **2008**, *19*, 265601.

[81] Shen, J.; Hu, Y.; Li, C.; Qin, C.; Ye, M. *Electrochim. Acta* **2008**, *53*, 7276-7280.

[82] Seo, M.H.; Choi, S.M.; Kim, H.J.; Kim, J.H.; Cho, B.K.; Kim, W.B. *J. Power Sources* **2008**, *179*, 81-86.

[83] Wang, S.; Wang, X.; Jiang, S.P. *Langmuir* **2008**, *24*, 10505-10512.

[84] Song, H.; Qiu, X.; Li, F. *Electrochim. Acta* **2008**, *53*, 3708-3713.

[85] Zhou, C.; Wang, H.; Peng, W.F.; Liang, J.; Yu, H.; Yang, J. *Langmuir* **2009**, *25*, 7711-7717.

[86] Wang, S.; Jiang, S.; White, T. J.; Guo, J.; Wang, X. *J. Phys. Chem. C* **2009**, *113*, 18935-18945.

[87] Jiang, S.; Ma, Y.; Jian, G.; Tao, H.; Wang, X.; Fan, Y.; Lu, Y.; Hu, Z.; Chen, Y. *Adv. Mater.* **2009**, *21*, 4953-4956.

[88] Han, D.M.; Guo, Z.P.; Zeng, R.; Kim, C.J.; Meng, Y.Z.; Liu, H.K. *In. J. Hydrogen Energy* **2009**, *34*, 2426-2434.

[89] Song, H.; Qiu, X.; Li, F. *Appl. Catal., A* **2009**, *364*, 1-7.

[90] Song, H.; Xiao, P.; Qiu, X.; Zhu, W.; *J. Power Sources* **2010**, *195*, 1610-1614.

[91] Chen, S.-L.; Lin, C.-T.; Chieng, C.-C.; Tseng, F.-G. *J. Power Sources* **2010**, *195*, 1640-1646.

[92] Zhao, Y.; Yang, X.; Tian, J.; Wang, F.; Zhan, L. *J. Power Sources* **2010**, *195*, 4634-4640.

[93] Zhou, C.; Peng, F.; Wang, H.; Yu, H.; Peng, C.; Yang, J. *Electrochem. Commun.* **2010**, *12,* 1210-1213.

[94] Li, W.; Liang, C.; Zhou, W.; Qiu, J.; Zhou, Z.; Sun, G.; Xin, Q. *J. Phys. Chem. B* **2003**, *107*, 6292-6299

[95] Selvaraj, V.; Alagar, M. *Electrochem. Commun.* **2007**, *9*, 1145-1153.

[96] Selvaraj, V.; Alagar, M. Kumar, K. S. *Appl. Catal., B* **2007**, *75*, 129-138.

[97] Selvaraj, V.; Alagar, M. *Nanotechnology* **2008**, *19*, 045504.

[98] Colmati, F.; Antolini, E.; Gonzalez. E.R. *Electrochim. Acta* **2005**, *50*, 5496-5503.

[99] Jung, Y.; Kim, S.; Park, S.-J.; Kim, J.M. *Colloids Surf., A* **2008**, *313-314*, 167-170.

[100] Wu, G.; Li, D.; Dai, C.; Wang, D.; Li, N. *Langmuir* **2008**, *24*, 3566-3575.

[101] Selvaraj, V.; Vinoba, M.; Alagar, M. *J. Colloid Interface Sci.* **2008**, *322*, 537-544.

[102] Xu, J.B.; Zhao, T.S.; *J. Power Sources* **2010**, *195*, 1071-1075.

[103] Geng, D.; Chen, L.; Lu, G. *J. Mol. Catal. A: Chem.* **2007**, *265*, 42-49.

[104] Wen, Z.; Ci, S.; Li, J. *J. Phys. Chem. C* **2009**, *113*, 13482-13487.

[105] Deivaraj, T.C.; Chen, W.; Lee, J.Y. *J. Mater. Chem.* **2003**, *13*, 2555-2560.

[106] Bera, P.; Gayen, A.; Hegde, M.S.; Lalla, N.P.; Spadaro, L.; Frusteri, F.; Arena, F. *J. Phys. Chem. B* **2003**, *107*, 6122-6130.

[107] Tu, H.-C.; Wang, W.-L.; Wan, C.-C.; Wang, Y.-Y. *J. Phys. Chem. B* **2006**, *110*, 15988-15993.

[108] Lee, C.L.; Ju, Y.C.; Chou, P.T.; Huang, Y.C.; Kuo, L.C.; Oung, J.C. *Electrochem. Commun.* **2005**, *7*, 453-458.

[109] Guo, S.; Dong, S.; Wang, E. *Adv. Mater.* **2009**, *21*, 1-4

[110] Saha, M.S.; Li, R.; Sun, X. *J. Power Sources* **2008**, *177*, 314-322.

[111]Kamavarama, V.; Veedub, V.; Kannana, A.M. *J. Power Sources* **2009**, *188*, 51-56.

[112]Tsuji, M.; Kubokawa, M.; Yano, R.; Miyamae, N.; Tsuji, T.; Jun, M.-S.; Hong, S.; Lim, S.; Yoon, S.-Ho.; Mochida, I. *Langmuir* **2007**, *23*, 387-390.

[113] Chien, C.-C.; Jeng, K.-T.; *Mater. Chem. Phys.* **2006**, *99*, 80-87.

[114] Liu, H.; Song, C.; Zhang, L.; Zhang, J.; Wang, H.; Wilkinson, D. P.; *J. Power Sources* **2006**, *155*, 95-110.

[115] Shao, Y.; Zhang, S.; Wang, C.; Nie, Z.; Liu, J.; Wang, Y.; Lin, Y. *J. Power Sources* **2010**, *195*, 4600-4605.

[116] Takasaki, F.; Noda, Z.; Masao, A.; Shiratori, Y.; Ito, K.; Sasaki, K. *ECS Transactions* **2009**, *25*,831-837.

[117] Liu, Z.; Ling, X. Y.; Guo, B.; Hong, L.; Lee, J. Y. *J. Power sources* **2007**, *167*, 272-280.

[118] Wang, J.; Yin, G.; Liu, H.; Li, R.; Flemming, R. L.; Sun, X. *J. Power Sources* **2009**, *194*, 668-673.

[119] Liu, Z.; Reed, D.; Kwon, G.; shamsuzzoha, M.; Nikoles, D. E. *J. Phys. Chem.* C **2007**, *111,* 14223-14229.

[120] Zhao, Y.; Fan, L.; Zhong, H.; Li, Y. *Microchim. Acta* **2007**, *158*, 327-334.

[121] Guo, D. J.; Li, H. L. *J. Electroanal. Chem.* **2004**, *573*, 197-202.

[122] Cui, H.-F.; Ye, J.-S.; Zhang, W.-E.; Wang, F.; Sheu, F.-S. *J. Electroanal. Chem.* **2005**, *577*, 295-302.

[123] Paoletti, C.; Cemmia, A.; Leonardo Giorgi, L.; Giorgi, R.; Pilloni, L.; Serra, E.; Pasquali, M. *J. Power Sources* **2008**, *183*, 84-91.

[124] He, Z.; Chen, J.; Liu, D.; Zhou, H.; Kuang, Y. *Diamond Relat. Mater.* **2004**, *13*, 1764-70.

[125] Zhao, Y.; Fan, L.; Zhong, H.; Li, Y.; Yang, S. *Ad*v. *Funct. Mater.* **2007**, *17*, 1537-1541.

[126] Tang, H.; Chen, J.; Yao, S.; Nie, L.; Kuang, Y.; Huang, Z.; Wang, D.; Wang, Z.; Ren, Z. *Mater. Chem. Phys.* **2005**, *92*, 548–553.

[127] Wu, G.; Xu, B. *J. Power Sources* **2007**, *174*, 148-158.

[128] Nagle, L.C.; Rohan, J.F. *J. Power Sources* **2008**, *185*, 411-418.

[129] Lim, T.W.; Chu, Y.; Bang, H.-K.; Choi, H.-U.; Cho, J.-S.; Kim, D.-L.; Kim, H.-J.; Han, M.K. *ECS Transactions* **2008**, *13*, 63-73.

[130] Pan, D.; Chen, J.; Tao, W.; Nie, L.; Yao, S.; *Langmuir* **2006,** *22,* 5872-5876.

[131] Chen, J.; Wang, M.; Liu, B.; Fan, Z.; Cui, K.; Kuang, Y.; *J. Phys. Chem. B* **2006**, *110*, 11775-11779.

[132] Girishkumar, G.; Rettker, M.; Underhile, R.; Binz, D.; Vinodgopal, K.; McGinn, P.; Kamat, P. *Langmuir* **2005,** *21,* 8487-8494.

[133] Hsieh, Y.-F.; Hsieh, Y-C.; Wu, P.-W.; Liao, C.-H.; Chang, Y.-M. *J. Electrochem. Soc.* **2010**, *157*, B39-B44.

[134] Liu, Z.; Gan, L. M.; Hong, L.; Chen, W.; Lee, J. Y. *J. Power. Sources* **2005**, *139*, 73-78.

[135] Chen, W.; Zhao, J.; Lee, J. Y.; Liu, Z. *Mater. Chem. Phys.* **2005**, *91*, 124-129.

[136] Yuan, H.; Song, H.; Qiu, X.; Zhu, W.; Chen, L. *Electrochem. Commun.* **2010**, *12*, 14-17.

[137] Liu, Z.; Lee, J.Y.; Chen, W.; Han, M.; Gan, L.M. *Langmuir* **2004**, *20*, 181-187.

[138] Liu, Z.; Guo, B.; Hong, L.; Lim, T.H. *Electrochem. Commun*. **2006**, *8*, 83-90.

[139] Ling, M.Z.; Zhu, Q.S. *Prog. Chem.* **1998**, *3*, 237–245.

[140] Fang, B.; Kim, J.H.; Kim, M.; Yu, J.-S. *Chem. Mater.* **2009**, *21,* 789–796.

[141] Chen, C.-C.; Chen, C.-F.; Chen, C.-M.; Chuang, F.-T. *Electrochem. Commun*. **2007**, *9*, 159-163.

[142] Li, J.; Liang, Y.; Liao, Q.; Zhu, X.; Tian, X. *Electrochim. Acta* **2009**, *54*, 1277-1285.

[143] Hwang, B.J.; Kumar, S.M.S.; Chen, C.-H.; Chang, R.-W.; Liu, D.-G.; Lee, J.-F. *J. Phys. Chem. C* **2008**, *112*, 2370-2377.

[144] Wang, H.; Sun, X.; Ye, Y.; Qiu, S. *J. Power Sources* **2006**, *161*, 839-842.

[145]Yang, D.-S.; Sim, K.-S.; Kwen, H.-D.; Choi, S.-H. *J. Nanomater.* **2011**, 134721.

[146] Oh, S.D.; So, B.K.; Choi, S.H.; Gopalan, A.; Lee, K.P.; Yoon, K.R.; Choi, I.S.; *Mater. Lett.* **2005**, *59*, 1121-1124.

[147] Choi, S.-H.; Gopalan, A.I.; Ryu, J.-H.; Lee, K. P. *Mater. Chem. Phys.* **2010**, *120*,

18–22.

[148] Ng, Y.H.; Ikeda, S.; Harada, T.; Park, S.; Sakata, T.; Mori, H.; Matsumura, M. *Chem. Mater.* **2008**, *20*, 1154-1160.

[149] Luo, X.; Imae, T. *J. Mater. Chem.* **2007**, 17, 567-571.

[150] Ozkaraoglu, E.; Tunc, I.; Suzer, S. *Polymer* **2009**, *50*, 462-466.

[151] Bai, L.; Zhu, H.; Thrasher, J.S.; Street, S.C. *ACS Appl. Mater. Interfaces* **2009**, *1*, 2304-2311.

[152] Nagao, D.; Shimazaki, Y.; Saeki, S.; Kobayashi, Y.; Konno, M.; *Colloids Surf., A* **2007**, *302*, 623-627.

[153] Mukerjee, S.; Srinivasan, S.; Appleby, A.H. *Electrochim. Acta* **1993**, *38*, 1661-1669.

[154] Hirano, S.; Kim, J.; Srinivasan, S. *Electrochim. Acta* **1997**, *42*, 1587-1593.

[155] Chen, C.C.; Chen, C.F.; Hsu, C.H.; Li, I.H.; *Diamond Relat. Mater.* **2005**, *14*, 770-773.

[156] Inoue, M.; Shingen, H.; Kitami, T.; Akamaru, S.; Taguchi, A.; Kawamoto, Y.; Tada, A.; Ohtawa, K.; Ohba, K.; Matsuyama, M.; Watanabe, K.; Tsubone, I.; Abe, T. *J. Phys. Chem. C* **2008**, *112*, 1479-1492.

[157] Kim, H.; Lee, J.; Kim, J. *J. Power Sources* **2008**, *180*, 191-194.

[158] Sun, C.-L.; Chen, L.-C.; Su, M.-C.; Hong, L.-S.; Chyan, O.; Hsu, C.-Y.; Chen, K.-H.; Chang, T.-F.; Chang, L. *Chem. Mater.* **2005**, *17*, 3749-3753.

[159] Tang, Z.; Poh, C. K.; Lee, K. K.; Tian, Z.; Chua, D. H. C.; Lin, J. *J. Power Sources* **2010**, *195*, 155-159.

[160] Tang, Z.; Ng, H.Y.; Lin, J.; Wee, A.T.S.; Chua, D.H.C. *J. Electrochem. Soc.* **2010**, *157*, B245-B250.

[161] Wakisaka, M.; Mitsui, S.; Hirose, Y.; Kawashima, K.; Uchida, H.; Watanabe, M. *J. Phys. Chem. B* **2006**, *110*, 23489-23496.

[162] Park, K.-W.; Han, S.-B.; Lee, J.-M. *Electrochem. Commun.* **2007**, *9*, 1578-1581.

[163] Wang, C.-H.; Du, H.-Y.; Tsai, Y.-T.; Chen, C.-P.; Huang, C.-J.; Chen, L.C.; Chen, K.H.; Shih, H.-C. *J. Power Sources* **2007**, *171*, 55-62.

[164] Irissou, E.; Laplante, F.; Garbarino, S.; Chaker, M.; Guay, D. *J. Phys. Chem. C* **2010**, *114*, 2192-2199.

[165] Yang, D.-Q.; Hennequin, B.; Sacher, E. *Chem. Mater*. **2006**, *18*, 5033-5038.

[166] Wang, S.-K.; Tseng, F.; Yeh, T.-K.; Chieng, C.-C.; *J. Power Sources* **2007**, *167*, 413-419.

[167] Kim, M.-S.; Fang, B.; Chaudhari, N.K.; Song, M.; Bae, T.-S.; Yu, J.-S. *Electrochim. Acta* **2010**, *55*, 4543-4550.

[168] Qu, L.; Dai, L.; Osawa, E.; *J. Am. Chem. Soc.* **2006**, *128*, 5523-5532.

[169] Wu, Z.P.; Xia, B.Y.; Wang, X.X.; Wang, J.N. *J. Power Sources* **2010**, *195*, 2143-2148.

[170] Zhu, J.; Cheng, F.; Tao, Z. Chen, J. *J. Phys. Chem. C* **2008**, *112*, 6337-6345.

[171] Du, H.; Li, B.; Kang, F.; Fu, R.; Zheng, Y. *Carbon* **2007**, *45*, 429–435.

[172] Salgado, J.R.C.; Antolini, E.; Gonzalez, E.R. *J. Phys. Chem. B* **2004**, *108*, 17767-17774.

[173] Qian, W.; Liu, T.; Wei, F.; Wang, Z.; Luo, G.; Yu, H.; Li, Z. *Carbon* **2003**, *41*, 2613.

[174] Woods, R. *J. Electroanal. Chem.* **1976**, *9*, 1.

[175] Wang, Z.B.; Yin, G.P.; Zhang, J.; Sun, Y.C.; Shi, P.F. *Electrochim. Acta* **2006**, *51*, 5691-5697.

[176] Hsieh, C.-T.; Lin, J.-Y. *J. Power Sources* **2009**, *188*, 347-352.

[177] Barisci, J.N.; Wallace, G.G.; Chattopadhyay, D.; Papadimitrakopolous, F.; Baughman, R.H. *J. Electrochem. Soc.* **2003**, *150*, E409-E415.

[178] Bard, A. J.; Faulkner, L. R. Electrochemical methods (2nd edition), Wiley, New York, 2001, Chap 10.

[179] Reshetenko, T.V.; Kim, H.-T.; Kweon, H.-J. *Electrochim. Acta* **2008**, *53*, 3043-3049.

[180] Liu, Z.; Hong, L.; Tay, S.W. *Mater. Chem. Phys.* **2007**, *105*, 222-228.

[181] Villers, D.; Sun, S. H.; Serventi, A.M.; Dodelet, J. P.; *J. Phys. Chem. B* **2006,** *110,* 25916-25925.

[182] Gojkovic, S.L.; Babic, B.M.; Radmilovic, V.R.; Krstajic, N.V. *J. Electroanal.*

Chem. **2010**, *639*, 161-166.

[183] Barbir F. PEM fuel cells: theory and practice. New York: Elsevier Academic Press, **2005**.

[184] Hirschenhofer, J.H.; Stauffer, D.B.; Engleman, R.R.; Klett, M.G. Fuel Cell Handbook (4^{th} edition). Reading PA: Parsons Corporation for U.S. Dept. of Energy, Office of Fossil Energy, Federal Energy Technology Center, **1998**.

[185] Ju, H.; Wang, C.Y. *J. Electrochem. Soc.* **2004**, *151*, A1954–A1960.

[186] Srinivasan, S.; Ticianelli, E.A.; Derouin, C.R.; Redondo, A. *J. Power Sources* **1988**, *22*, 359–375.

[187] Srinivasan, S.; Velew, O.A.; Parthasarathy, A.; Manko, D.J.; Appleby, A.J. *J Power Sources* **1991**, *36*, 299–320.

[188] Kim, J.; Lee, S.M.; Srinivasan, S. *J. Electrochem. Soc.* **1995**, *142*, 2670–2674.

[189] Iijima, S. *Nature* **1993**, *363*, 603-605.

[190] Taylor, A.D.; Michel, M.; Sekol, R.C.; Kizuka, J.M.; Kotov, N.A.; Thompson, L.T. *Adv. Funct. Mater.* **2008**, *18*, 3003–3009.

[191] Smiljanic, O.; Dellero, T.; Serventi, A.; Lebrun, G.; Stansfield, B.L.; Dodelet, J.P.; Trudeau, M.; Désilets, S.; *Chem. Phys. Lett.* **2001**, *342*, 503-509.

[192] Sun, X.; Stansfield, B.; Dodelet, J.P.; Désilets, S. *Chem. Phys. Lett.* **2002**, *363*, 415-421.

[193] Sun, X.; Li, R.; Stansfield, B.; Dodelet, J.P.; Désilets, S. *Chem. Phys. Lett.* **2004**, *394*, 266-270.

[194] Sun, X.; Li, R.; Villers, D.; Dodelet, J.P.; Désilets, S. *Chem. Phys. Lett.* **2003**, *379*, 99-104.

[195] Ebbesen, T.W.; Hirua, H.; Bisher, M.E.; Treacy, M.M. J.; Shreeve-Keyer, J.L. Haushalter, R.C. *Adv. Mater*. **1996**, *8*, 155-157.

[196] Yu, R.; Chen, L.; Liu, Q.; Tan, K.L.; Ng, S.C.; Chan, H.S.O.; Xiu, G.Q.; Hor, T.S.A. *Chem. Mater.* **1998**, *10*, 718-722.

[197] Kim, Y.-T.; Mitani, T. *J. Catal.* **2006**, *238*, 394-401.

[198] Wertheim, G.K.; Dicenzo, S.B.; Young, S.E. *Phys. Rev. Lett*. **1983**, *51*, 2310-2313.

[199] Kim, Y.-T.; Ohshima, K.; Higashiming, K.; Uruga, T.; Takata, M.; Suematsu, H.; Mitani, T. *Angew. Chem. Int. Ed.* **2006**, *45*, 407-411.

[200] Wei, G.; Pan, C.; Reichert, J.; Jandt, K.D.; *Carbon* **2010**, *48*, 645-653.

[201] Schmidt, T.J.; Noeske, M.; Gasteiger, H.A.; Behm, R.J.; Britz, P.; Brijoux, W.; Bonnemann, H. *Langmuir* **1997**, *13*, 2591-2595.

[202] Su, X.; Dong, S.; Wang, E. *Polymer* **2004**, *45*, 2181-2184.

[203] Hu, X.; Wang, T.; Qu, X.; Dong, S. *J. Phys. Chem. B* **2006**, *110*, 853-857.

[204] Li, J.; Yang, W.; Zhu, H.; Wang, X.; Yang, F.; Zhang, B.; Yang, X. *Talanta* **2009**, *79* 935-79939.

[205] Lamy, C.; Leger, J.M.; Srinivasan, S.; Bockris, J.O'M.; Conway, B.E.; White, R.E. Modern Aspects of Electrochemistry, **2001**, *34*, 53–118.

[206] Liu, H.; Song, C.; Zhang, L.; Zhang J.; Wang, H.; Wilkinson, D.P. *J. Power Sources* **2006**, *155*, 95-110.

[207] Bockris, J.O.M.; Wroblowa, H. *J. Electroanal. Chem.* **1964**, *7*, 428–451.

[208] Watanabe, M.; Uchida, M.; Motoo, S. *J. Electroanal. Chem. Interfacial Electrochem.* **1987**, *229*, 395–406.

[209] Watanabe, M.; Motoo, S. *J. Electroanal. Chem.* **1975**, *60*, 275-283.

[210] Watanabe, M.; Motoo, S. *J. Electroanal. Chem.* **1975**, *60*, 267-273.

[211] Iwasita, T.; F.C. Nart, W. Vielstich, *Ber. Bunserges. Phys. Chem.* **1990**, *94*, 1030.

[212] Frelink,T.; Visscher, W.; van Venn, J.A.R. *Langmuir* **1996**, *12*, 3702-3708.

[213] Iwasita, T.; Nart, F.C.; Vielstich, W. *Phys Chem Chem Phys* **1990**, 94, 1030–1034.

[214] Lu C, Rice C, Masel RI, Babu PK, Waszczuk P, Kim HS, et al. *J. Phys. Chem. B* **2002,** *106,* 9581-9589.

[215] Davies, J.C.; Hayden, B.E.; Pegg, D.J.; Rendall, M.E. Surf. Sci. **2002**, *496*, 110–120.

[216] Stamenkovic, V.R.; Arenz, M.; Lucas, C.A.; Gallagher, M.E.; Ross, P.N.; Markovic, N.M. *J. Am. Chem. Soc.* **2003**, *125*, 2736–2745.

[217] Desai, S.; Neurock, M.A. *Electrochim. Acta* **2003**, *48*, 3759-3773.

[218] Bock, C.; Blakely, M.A.; MacDougall, B. *Electrochim. Acta* **2005**, *50*, 2401-2414.

[219] Zhou, W.; Zhou, Z.; Song, S.; Li, W.; Sun, G.; Tsiakaras, P.; Xin, Q. *Appl. Catal. B* **2003**, 46, 273-285.

[220] Purgato, F.L.S.; Olivi, P.; Léger, J.-M.; de Andrade, A.R.; Tremiliosi-Filho, G.; Gonzalez, E.R.; Lamy, C.; Kokoh, K. B.; *J. Electroanal. Chem.* **2009**, *628*, 81-89.

[221] Hitmi, H.; Belgsir, E.M.; Léger, J.-M.; Lamy, C.; Lezna, R.O. *Electrochim. Acta* **1994**, *39*, 407-415.

[222] Zhou, W.J.; Song, S.Q.; Li, W.Z.; Zhou, Z.H.; Sun, G.Q.; Xin, Q.; Douvartzides, S.; Tsiakaras, P. *J. Power Sources* **2005***, 140*, 50-58.

[223] Spinacé, E.V.; Linardi, M.; Neto, A.O. *Electrochem. Commun.* **2005**, *7*, 365-369

[224] Jiang, L.; Sun, G.; Sun, S.; Liu, J.; Tang, S.; Li, H.; Zhou, B.; Xin, Q. *Electrochim. Acta* **2005**, *50*, 5384-5389.

[225] Colmenares, L.; Wang, H.;Yusys, Z.; Jiang, L.; Yan, S.; Sun, G.Q.; Behm, R.J. Electrochim. Acta, **2006**, *52*, 221.

[226] Delime, F.; Leger, J.M.; Lamy, C. *J. Appl. Electrochem.* **1999**, *29*, 1249-54.

[227] Vigier, F.; Coutanceau, C.; Hahn, F.; Belgsir, E.M.; Lamy, C. *J. Electroanal. Chem.* **2004**, *563*, 81-89.

[228] Antolini, E. *Appl. Catal. B* **2007**, *74*, 324–336.

[229] Antolini, E. *Appl. Catal. B* **2007**, *74*, 337–350.

[230] Antolini, E. *J. Power Sources* **2007**, *170*, 1-12.

CHAPTER III EXPERIMENTAL & CHARACTERIZATION

3.1 Materials

Multi-walled carbon nanotubes (MWCNTs, 95% purity, diameter=30nm-60nm) were obtained from Helix Material Solutions, Inc. Potassium tetrachloroplatinate (K_2PtCl_4, 98%), ruthenium chloride ($RuCl_3$, 98%), tin(II) chloride dihydrate ($SnCl_2 \cdot 2H_2O$, 98%), potassium bromide (KBr, IR grade), Nafion solution (5wt% in ethanol), ethylene glycol (EG, 99%) methanol (99%), and ethanol (99%) were purchased from Sigma-Aldrich. Polyethyleneimine (PEI 50wt% in water, Mw=60,000), sulfuric acid (98wt%) and nitric acid (69wt%) were obtained from Alfa Aesar. Pt/Vulcan XC-72 electrocatalyst with 20wt% metal loading was purchased from E-TEK (BASF). All the chemicals were used as received without further purification. Ultrapure Milli-Q water (resistivity>18.2 MΩ cm) was exclusively used for making aqueous solutions and rinsing procedures.

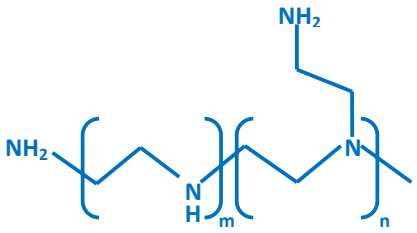

Fig. 3.1 Molecular structure of Polyethyleneimine (PEI).

3.2 Surface functionalization of MWCNTs

3.2.1 Oxidation of MWCNTs

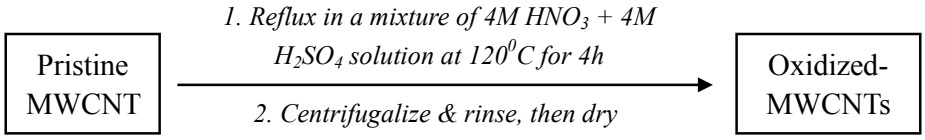

MWCNTs were oxidized using the conventional acid oxidization method [1]. 100mg of pristine MWCNTs were refluxed in a mixture of 4M H_2SO_4 and 4M HNO_3 solution using an oil bath under magnetic stirring. The temperature was elevated to 120°C and maintained for 4h. The obtained oxidized-MWNCTs (denoted as

O-MWCNTs) was washed with copious water, centrifugalized and then dried at 70°C overnight.

a	Hot plate and magnetic stirrer
b	Oil bath
c	Thermometer
d	Refluxing system
e	Exhaust adsorption

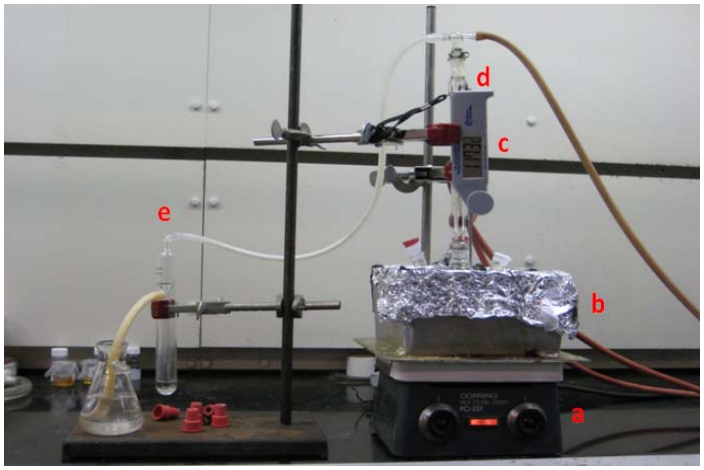

3.2.2 Non-covalent modification of CNT with PEI

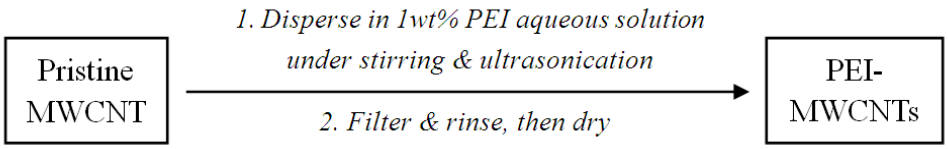

Non-covalent functionalization of MWCNTs by PEI was carried out through a procedure modified from previous publication [2]. Briefly, 100mg of MWCNTs was dispersed into 200ml 1wt% PEI aqueous solution, followed by ultrasonication for 3h and magnetic stirring for 12h. The PEI-MWCNTs suspension was then filtered with a 0.2μm nylon filter membrane and rinsed to remove excess PEI. The obtained PEI-MWCNTs nanocomposite was dried at 70°C overnight and collected for further use.

3.3 Synthesis of Pt-based electrocatalyst on MWCNTs

a	Temperature controller
b	Heating mantle
c	Thermocouple
d	Magnetic stirrer
e	Refluxing tube
f	Cooling water
g	Injection of metal precursors
h	N_2 feeding pipe
i	Exhaust adsorption + N_2 flow rate control

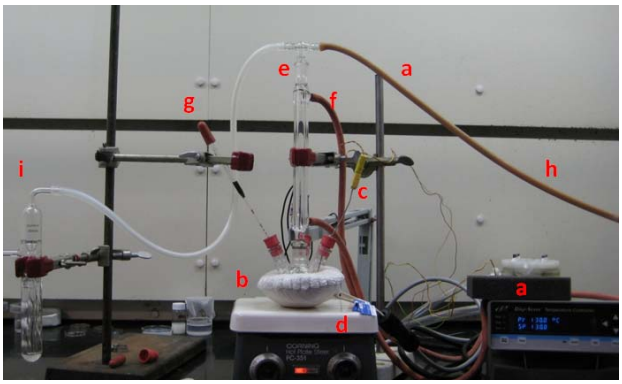

Fig. 3.3 Experimental setup for the synthesis of Pt-based electrocatalyst supported on PEI-MWCNTs

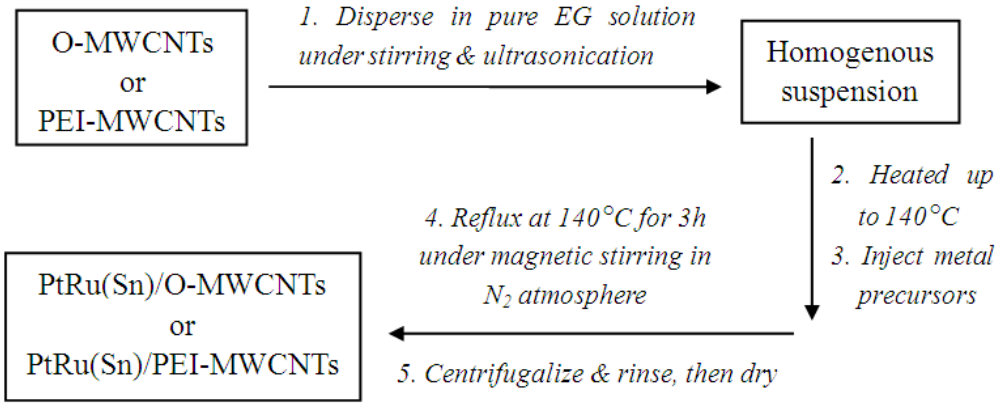

3.3.1 Synthesis of PEI-MWCNTs supported Pt NPs

Pt/PEI–MWCNTs catalyst was prepared by an in-situ polyol reduction method. The typical procedure is as follows. 80mg collected PEI-MWCNTs were dispersed in 100ml pure ethylene glycol (EG) solution with the aid of ultrasonication and vigorous agitation. Then the homogeneous suspension was heated up to 140°C using a heating

mantle. EG solution containing calculated amount of K_2PtCl_4 precursor was injected drop-wise to achieve the nominal Pt loading of 20wt%. A flow of ultra-high purity nitrogen was also introduced to the reaction system to isolate oxygen and to remove organic byproducts during the synthesis step. After refluxing for 3h at 140°C, the metal precursor is expected to be completely reduced by EG at the elevated temperature. Then the as-synthesized Pt/PEI-MWCNTs hybrid material was centrifugalized, rinsed repeatedly and dried overnight.

3.3.2 Preparation of MWCNTs supported bimetallic PtRu or PtSn electrocatalysts

PtRu/PEI–MWCNTs catalyst was prepared in a similar manner, where EG solution containing calculated amount of K_2PtCl_4 and $RuCl_3$ with a molar ratio of Pt:Ru=1:1 was added drop-wise to achieve the nominal PtRu loading of 10wt%, 30wt% and 50wt%, respectively. For the purpose of comparison, oxidized-MWCNTs supported PtRu nanocomposite (denoted as PtRu/O-MWCNTs) with Pt:Ru atomic ratio of 1:1 and 30wt% metal loading was prepared and collected [3]. In addition, (Pt:Sn=1:1 atom%) PtSn/PEI-MWCNTs nanocomposite with Pt nominal loading of 20wt% was also prepared by replacing the $RuCl_3$ with $SnCl_2$ during the synthesis step.

3.4 Characterization

3.4.1 Solubility in DI water

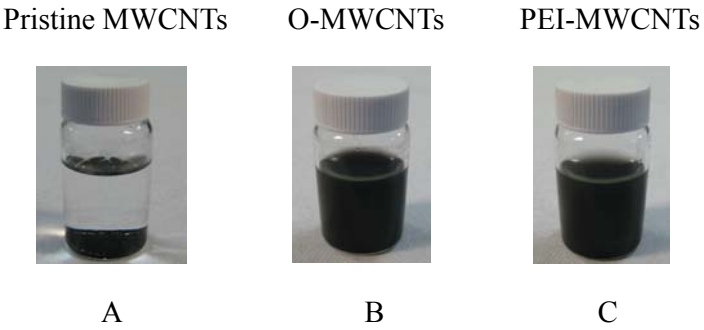

Fig. 3.4 Different MWCNTs samples dispersed in DI water (A) after 3 minutes (B) after 3 hours (C) after one days.

In order to confirm the surface functionalization of MWCNTs, the solubility of various types of MWCNTs in DI was examined. 10mg of MWCNTs, O-MWCNTs,

and PEI-MWCNTs samples were respectively dispersed in 15ml DI water using ultrasonic bath. It was found that the pristine MWCNTs precipitated rapidly within one minute due to the hydrophobic surface property and strong entanglement of MWCNTs bundles. By contrast, the oxidized MWCNTs specimen remained stable in DI after 3 hours, but they eventually aggregated together after one day. In the case of PEI-modified MWCNTs, the homogeneous black slurry kept stable for almost a week. This phenomenon implies that the hydrophilic PEI polymer chains might strongly adsorbed onto MWCNTs surface and resulted in substantial solubility enhancement. Meanwhile, the cationic PEI coating may also protect the MWCNTs against entanglement and aggregation.

3.4.2 Zeta-potential measurement

Zeta-potential measurement is widely employed to monitor the surface charge on nanoparticles. Low concentrated samples (0.01wt%) was first made by dispersing 10mg of MWCNTs, PEI-MWCNTs respectively in 100ml DI water through ultrasonic treatment. The pH value of the suspension was adjusted using either 0.01M NaOH or 0.01M HCl solution [4]. Then 2ml sample with different pH value was transferred into a green cell and placed into the Marvern Zetasizer Nano ZS90. The plot of zeta potential as a function of pH value was recorded and shown in Chapter IV, submitted paper #1, fig.2, page 90.

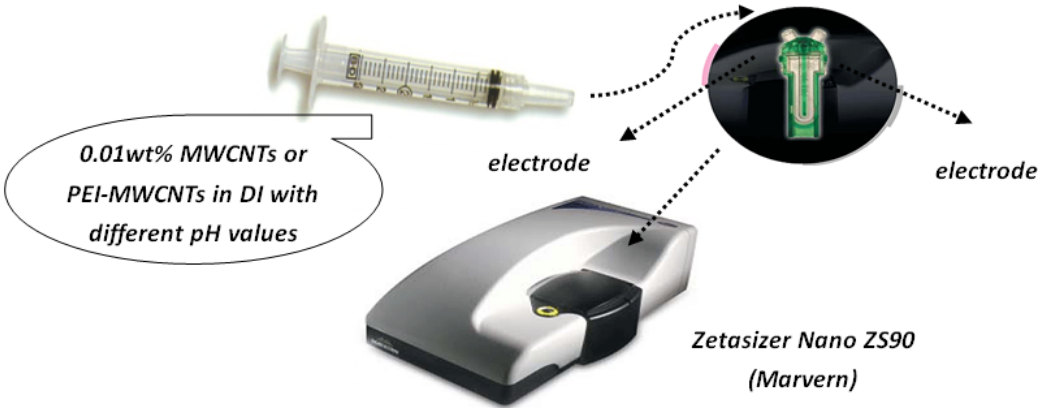

Fig. 3.5 Procedures for Zeta potential measurements

3.4.3 FTIR spectrum study

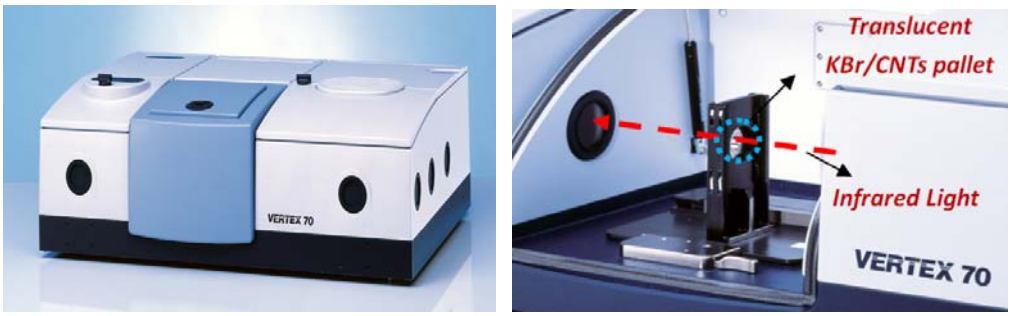

Fig. 3.6 VERTEX 70 FTIR spectrometer operating under transmission mode

Certain amount of pristine-MWCNTs or PEI-MWCNTs were mixed with IR grade KBr powder, and ground to fine powder using pestle and agate mortar. The obtained specimen containing approximate 0.5wt% CNTs was placed into a specific sample holder and pressed to a translucent thin pallet. The FTIR adsorption spectra was recorded on Brukeroptics Vetex70 spectrometer under transmission mode. The FTIR spectra of pristine MWCNTs and PEI-MWCNTs are shown and interpreted in Chapter 4, submitted paper #1, fig.3, page 91.

3.4.4 Electron microscopy observation

(a) (b)

Fig. 3.7 (a) JEOL 100CX TEM (b) JEOL 7000F SEM

The morphology of the nanocomposite was studied by a JEOL 7000F scanning electron microscope (SEM, field-emission gun) and JEOL 100CX transmission electron microscope (TEM, LaB_6 filament) operating at an accelerating voltage of 15kV and 100kV, respectively. The particle size and corresponding size distribution was analyzed using image J. The composition and catalyst loading are examined by Oxford energy dispersive X-ray (EDX) system equipped on SEM.

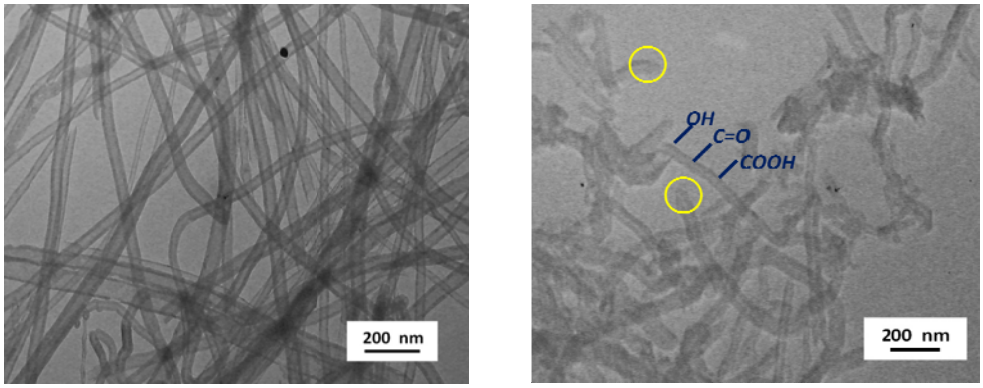

(a) (b)

Fig. 3.7 TEM images of (a) pristine MWCNTs and (b) oxidized-MWCNTs. (The opening tips were marked by yellow circles.)

As shown in Fig. 3.7, pristine MWCNTs have smooth surface and long, flexible morphology. By contrast, O-MWCNTs are typically shortened or truncated by refluxing in the mixture of acid. Moreover, the acid oxidation procedure may also open tube tips and introduced hydroxyl, carbonyl or carboxyl functional groups on the surface of MWCNTs.

The TEM images as well as the size distribution histograms of Pt-based nanoparticles supported on MWCNTs are shown in the chapter IV:.

Sample	TEM images	Size distribution histogram
30wt% PtRu/O-MWCNTs	Paper #1: fig.4a, Page 92	Paper #1: fig.4b, Page 92
30wt% PtRu/PEI-MWCNTs	Paper #1: fig.4c, Page 92	Paper #1: fig.4d, Page 92
10wt% PtRu/PEI-MWCNTs	Paper #1: fig.4e, Page 92	Paper #1: fig.4f, Page 92
50wt% PtRu/PEI-MWCNTs	Paper #1: fig.4g, Page 93	Paper #1: fig.4h, Page 93
20wt% Pt/Vulcan XC-72 Carbon (E-TEK)	Paper #2: fig.4a, Page 107	
20wt% Pt/PEI-MWCNTs	Paper #2: fig.4b, Page 107	Paper #2: fig.4c, Page107
PtSn/PEI-MWCNTs(Pt 20wt%, Pt:Sn=1:1atom%)	Paper #2: fig.4d, Page 107	Paper #2: fig.4e, Page107

All the SEM image and EDX spectrum are also demonstrated in the Chapter IV.

Sample	SEM image	EDX spectrum
Pristine MWCNTs	Paper #1: fig.5a Page 94	
30wt% PtRu/PEI-MWCNTs	Paper #1: fig.5b Page 94	Paper #1: fig.6 Page 94
20wt% Pt/XC-72 Carbon (E-TEK)	Paper #2: fig.5a Page 108	
20wt% Pt/PEI-MWCNTs	Paper #2: fig.5b Page 108	Paper #2: fig.6a Page 109
PtSn/PEI-MWCNTs(Pt 20wt%, Pt:Sn=1:1atom%)	Paper #2: fig.5c Page 108	Paper #2: fig.6b Page 109

3.4.5 X-ray diffraction patterns

Fig. 3.8 Rigaku Geigerflex X-ray diffractometer

The as-synthesized CNTs supported catalysts were ground to ultrafine powder using pestle and mortar. An approximate of 30mg powder was placed on a specimen sample holder and characterized using a Rigaku Geigerflex X-ray diffractometer. The operation condition is as follows: Cu Kα radiation, voltage 37.5kV, current 25mA, step size 0.05°/s. The XRD was calibrated using diffraction line (26.7°) of quartz before measurement.

The XRD patterns of pristine MWCNTs, 30wt% PtRu/O-MWCNTs and 30wt% PtRu/PEI-MWCNTs are shown in Chapter IV: submitted paper #1, fig.7, page 95.

The XRD patterns of 20wt% Pt/Vulcan XC-72 Carbon (E-TEK), 20wt% Pt/PEI-MWCNTs, PtSn/PEI-MWCNTs (Pt 20wt%, Pt : Sn= 1:1 atom%) are shown in Chapter IV: submitted paper #2, fig.7, page 109-110.

3.4.6 Electrochemical investigation

3.4.6.2 Catalyst ink preparation

20mg carbon supported Pt-based electrocatalyst was dispersed in 5ml of DI or ethanol via ultrasonic treatment for 3hr. And 3-5 drops of Nafion solution (5wt% in ethanol) were also added as binder.

3.4.6.1 GCE modification

Prior to the electrochemical investigation, the glassy carbon electrode (GCE) was polished to mirror finish and tested in a solution containing KNO_3+$K_3Fe(CN)_6$. If the potential difference between oxidation peak and reduction peak is less than 80mV, the GCE is ready for use. 7μl of the as-prepared catalyst ink was then applied onto the surface of GCE using a pipette. The catalyst loading on GCE could be further increased by repeatedly pipetting and drying. At last, a thin layer of Nafion film was coated onto the surface of catalyst modified GCE through casting one drop of 0.5wt% Nafion solution.

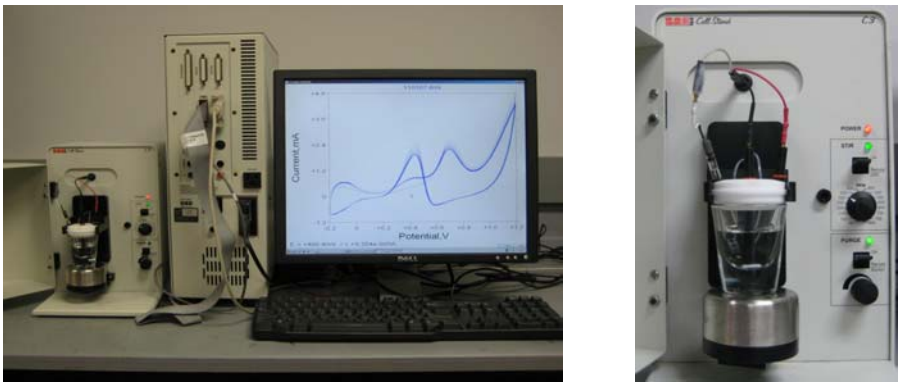

(a) (b)

Fig. 3.9 BASi 100B electrochemical analyzer and C3 Cell stand (red line: Pt wire auxiliary electrode, white line: Ag/AgCl reference electrode, black line: catalyst modified glassy carbon working electrode with a diameter of 3mm).

Electrochemical measurements were carried out on a BASi 100B electrochemical analyzer using conventional three-electrode cell, as shown in Fig. 3.9. The electrolyte solution was purged with ultra high purity N_2 prior to electrochemical investigation and all the experiment was conducted at room temperature.

3.4.6.2 ECSA measurement

The electrochemical active surface area (ECSA) was calculated using cyclic

voltammograms of the hydrogen adsorption and desorption on catalyst-modified GCE in the solution of 0.5M H_2SO_4 at a scan rate of 50mV/s. The ECSA of 30wt% PtRu/O-MWCNTs and PtRu/PEI-MWCNTs are calculated and compared in Chapter IV. submitted paper #1, fig.8, page 96-97. And the ECSA of 20wt% Pt/Vulcan XC-72 carbon (E-TEK), 20wt% Pt/PEI-MWCNTs, PtSn/PEI-MWCNTs (Pt 20wt%, Pt : Sn= 1:1 atom%) are estimated and analyzed in Chapter IV. submitted paper #2, fig. 8, page. 110.

3.4.6.3 MOR and EOR catalytic activity

The catalytic activities of different catalysts towards methanol oxidation (MOR) are characterized by cyclic voltammetry (CV) in 0.5M H_2SO_4 solution containing 1M methanol, the results of which are shown in Chapter IV. submitted paper #1, fig.9, page 97-98. The catalytic activities of different catalysts towards ethanol oxidation (EOR) are evaluated by cyclic voltammetry (CV) in 0.5M H_2SO_4 solution containing 1M ethanol. The corresponding results are shown in Chapter IV. submitted paper #2, fig.9, page 111.

3.4.6.4 Durability test

The durability of 20wt% Pt/Vulcan XC-72 carbon (E-TEK), 20wt% Pt/PEI-MWCNTs, and PtSn/PEI-MWCNTs (Pt 20wt%, Pt : Sn= 1:1 atom%) catalysts was evaluated by chronoamperogram. A typical chronoamperogram were recorded at fixed potential of 0.6V(vs. Ag/AgCl) for 600s in a solution of 0.5M H_2SO_4 containing 1M C_2H_5OH. The relevant information is provided in Chapter IV. submitted paper #2, fig.10, page 111-112.

Reference

[1] Li, W.; Liang, C.; Zhou, W.; Qiu, J.; Zhou, Z.; Sun, G.; Xin, Q. *J. Phys. Chem. B* **2003**, *107*, 6292-6299

[2] Li, J.; Yang, W.; Zhu, H.; Wang, X.; Yang, F.; Zhang, B.; Yang, X. *Talanta* **2009**, *79* 935-79939.

[3] Lordi, V.; Yao, N.; Wei, J. *Chem. Mater.* **2001**, *13*, 733-737.

[4] Wang, S.; Jiang, S.P.; Wang, X. *Nanotechnology* **2008**, *19*, 265601.

CHAPTER IV SUBMITTED MANUSCRIPTS

Paper #1

In-situ synthesis and characterization of polyethyleneimine-modified carbon nanotubes supported PtRu electrocatalyst for methanol oxidation

(submitted to *Materials Research Bulletin*)

ABSTRACT

In the present work, PtRu bimetallic nanoparticles were successfully synthesized on polyethyleneimine (PEI) functionalized multiwalled carbon nanotubes (MWCNTs) via an effective and facile polyol reduction approach. Noncovalent surface modification of MWCNTs with PEI was confirmed by FTIR and Zeta-potential measurements. The morphology, crystalline structure and composition of the hybrid material was characterized by transmission electron microscopy (TEM), scanning electron microscopy (SEM), X-ray powder diffraction (XRD) and energy dispersive X-ray spectroscopy (EDX), respectively. According to SEM and TEM observations, PtRu nanoparticles with narrow size distribution were homogeneously deposited on PEI-MWCNTs. Cyclic voltammetry tests demonstrated that the as-prepared PtRu/PEI-MWCNTs nanocomposite had a large electrochemical surface area and exhibited enhanced electrocatalytic activity towards methanol oxidation in comparison with oxidized-MWCNTs as catalyst support. PEI-functionalized CNTs, as useful building blocks for the assembly of Pt-based electrocatalyst, may have great potential for applications such as direct methanol fuel cell (DMFC).

KEYWORDS: A. Nanostructures; B. Chemical synthesis; C. Catalytic properties; D. Electrochemical properties

1. Introduction

Over the past decade, carbon nano tubes (CNTs) with large active surface area,

excellent electronic conductivity and high chemical stability have drawn considerable attention as an advanced supporting material for Pt-based catalyst [1-3]. Nevertheless, the surface of pristine CNT is chemically inert and hydrophobic, which is unfavorable for the deposition of metal nanoparticles (NPs) [4]. For this reason, CNTs are usually pretreated with concentrated acid to introduce hydroxyl and carboxyl functional groups. On the one hand, these functional groups can improve the solubility of the CNTs and provide preferential sites for the immobilization of noble metal catalyst [5]. On the other hand, this common modification method will disrupt the graphite structure of CNTs and result in the loss of electrical conductivity and the reduction of corrosion resistance [6].

With an attempt to overcome the disadvantages caused by acid treatment, substantial efforts have been devoted to noncovalent functionalization of CNTs. As a versatile strategy, noncovalent functionalization of CNTs not only preserves the intrinsic structure of CNTs, but achieves the tailored properties of the nanocomposites [7, 8]. Well-dispersed Pt nanoclusters on CNTs were prepared using bifunctional triphenylphosphine (PPh_3) or 1-amninopyrene (1-AP) as the interlinker, where the PPh_3 or 1-AP molecules were strongly adsorbed on the CNTs through noncovalent π-π stacking interaction [8, 9]. Positively charged poly (diallyldimethylammonium chloride) (PDDA) modified CNTs have also been explored as templates for the deposition of Pt NPs with high density [10, 11]. By using polymer wrapping technique, a controllable decoration of CNTs with poly (sodium 4-styrenesulfonate) (PSS) and Pt NPs in sequence was described by Kongkanand et al [12]. In addition, a novel route towards the self-assembly of cetyltrimethylammonium bromide (CTAB) stabilized Pt nanocubics on PSS-modified CNTs has also been demonstrated by means of electrostatic interaction [13].

Polyethyleneimine (PEI), as a polymeric surfactant, has been investigated to achieve surface functionalization of noble metal NPs. Sun et al. prepared PEI-protected gold NPs by heating a PEI/$HAuCl_4$ aqueous solution, where PEI served both as a reducing agent and capping agent [14]. Bai et al. presented a clean and efficient route to synthesize monodispersed Pt NPs via UV photoreduction of PEI

mediated-$PtCl_6^{2-}$ anions [15]. Moreover, the amino-rich cationic PEI is known to be effectively attached on the sidewalls of CNTs via physisorption [16]. Construction of one-dimensional CNT/metal NPs (metal=Au, Pt, Pd, Ag) heterogeneous nanostructures has been shown via chemical reduction of PEI-metal ion complexes adsorbed onto CNTs [16-18].

In the pursuit of higher electrocatalytic activity and more stable performance, CNT supported PtRu binary catalysts [19-21] have particularly been proven as the promising catalyst candidate for direct methanol fuel cell (DMFC). According to the bifunctional mechanism, the presence of Ru element could effectively modify the electronic nature of the Pt as well as remove the carbonaceous species to protect the Pt from being poisoned [22, 23]. To our knowledge, even though tremendous progress has been made to tailor the size and shape of Pt NPs on CNT, very little research work has been conducted to control the morphology of bimetallic NPs by noncovalent functionalizing the surface of CNT.

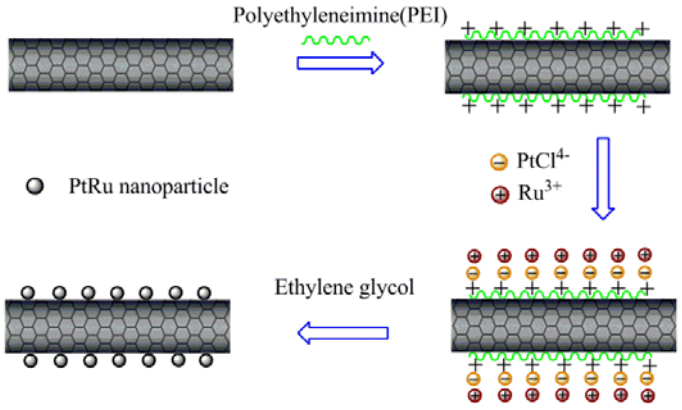

Fig.1. Schematic of the synthesis of PtRu electrocatalyst on PEI-functionalized MWCNTs.

Herein, we present a simple and efficient synthesis route to anchor bimetallic PtRu electrocatalyst on PEI modified CNTs with tunable size and well-defined shape. Fig.1 illustrates the scheme of the immobilization of PtRu NPs on PEI-MWCNTs. The physiochemical and electrochemical properties of the as-prepared nanocomposites were characterized by Zeta-potential, FTIR, SEM, TEM, XRD and

cyclic voltammetry.

2. Experimental

2.1. Materials

Multi-walled carbon nanotubes (MWCNTs, 95% purity, diameter=30nm-60nm) were obtained from Helix Material Solutions, Inc. Potassium tetrachloroplatinate (K_2PtCl_4, 98%), ruthenium chloride ($RuCl_3$, 98%), Nafion solution (5wt% in ethanol), ethylene glycol (EG, 99%) and methanol (99%) were purchased from Sigma-Aldrich. Polyethyleneimine (PEI 50wt% in water, Mw=60,000), sulfuric acid (98wt%) and nitric acid (69wt%) were obtained from Alfa Aesar. All the chemicals were used as received without further purification. Ultrapure Milli-Q water (resistivity>18.2 MΩ cm) was exclusively used for making aqueous solutions and rinsing procedures.

2.2. PEI and acid functionalization of MWCNTs.

Noncovalent functionalization of MWCNTs by PEI was carried out through a procedure adapted from literature [17, 18]. Briefly, 100mg of MWCNTs were dispersed in 200ml 1wt% PEI aqueous solution, followed by ultrasonication for 3h and magnetic stirring for 12h. Then the stable PEI-CNT suspension was filtered using a 0.2μm nylon filter membrane and rinsed to remove the excess PEI. MWCNTs were also functionalized by the conventional acid oxidization method in which 100mg of pristine MWCNTs was refluxed in a 4M H_2SO_4 and 4M HNO_3 mixture at 120°C for 4h [24]. The obtained oxidized-MWNCTs was washed with copious water, filtered and dried at 70°C overnight.

2.3. Synthesis of MWCNTs supported PtRu electrocatalysts

PtRu/PEI–MWCNTs catalyst was prepared by an in-situ polyol reduction method. The typical procedure is as follows: PEI-CNTs was dispersed in an EG solution under ultrasonic treatment and vigorous agitation, calculated amount of K_2PtCl_4 and $RuCl_3$ with a molar ratio of Pt:Ru=1:1 was added dropwise to achieve the nominal PtRu

loading of 10wt%, 30wt% and 50wt%, respectively. The mixture was heated to 140°C and maintained for 3h to completely reduce the metal precursors. A flow of ultra-high purity nitrogen was also introduced to the reaction system to isolate oxygen and to remove organic byproducts during the synthesis step. After the deposition of PtRu NPs, the as-synthesized PtRu/PEI-MWCNTs hybrid material was centrifugalized, rinsed repeatedly and dried overnight. For comparison purpose, oxidized-MWCNTs supported PtRu nanocomposite (denoted as PtRu/O-MWCNTs) with Pt:Ru atomic ratio of 1:1 and 30wt% metal loading was also prepared and collected [25].

2.4. Physiochemical characterization

To monitor the surface charge of MWCNTs, the zeta potential measurement was performed using a Marvern Zetasizer Nano ZS90. FTIR spectra were acquired by Brukeroptics Vetex70 spectrometer to further confirm the functionalization of MWCNTs with PEI. The morphology of the nanocomposite was studied by a JEOL 7000F scanning electron microscope (SEM) and JEOL 100CX (LaB_6 filament) transmission electron microscope (TEM) operating at an accelerating voltage of 100kV. The presence of noble metal NPs are detected by energy dispersive X-ray analysis (EDX) and the X-ray diffraction (XRD) patterns of the samples were recorded using a Rigaku Geigerflex X-ray diffractometer with Cu Kα radiation.

2.5. Electrochemical Analysis

Cyclic voltammetric measurements were carried out on a BASi 100B electrochemical analyzer with a conventional three-electrode cell. Glassy carbon electrode (GCE) (3mm in diameter) was used as the working electrode, on which a thin layer of Nafion-impregnated PtRu/MWCNTs catalyst was applied. The catalyst loading was fixed at 1mg/cm^2 for both the 30wt% PtRu/PEI-MWCNTs and 30wt% PtRu/O-MWCNTs modified GCE electrodes. Platinum wire served as the counter electrode and Ag/AgCl electrode was used as the reference electrode. The electrochemical active surface area (ECSA) was calculated using cyclic voltammograms of the nanocomposite catalyst in the solution of 0.5M H_2SO_4. The

electrocatalytic activity for the methanol oxidation was characterized by cyclic voltammetry (CV) in a solution of 1M CH_3OH + 0.5 M H_2SO_4. The electrolyte solution was deaerated with ultra high purity N_2 prior to the measurement and the entire experiment was conducted at room temperature.

3. Results and discussion

3.1. Zeta potential measurement of PEI-CNT nanocomposite

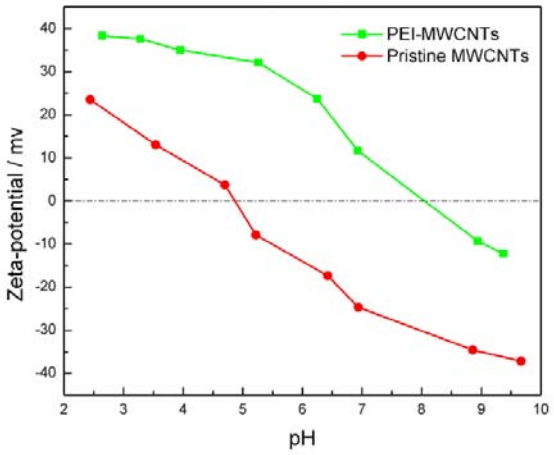

Fig.2. Zeta potential as a function of pH for pristine MWCNTs and PEI-MWCNTs.

Zeta potential is the electrical potential existing at the shear plane of a nanoparticle, which has been widely used to determine the surface charge at the electric double layer [11]. During the measurement, low concentration samples (0.01wt%) were dispersed in 1mM NaCl solutions to ensure the constant ionic strength. The pH of the suspension was adjusted by adding either HCl or NaOH [11, 26]. The zeta potential as a function of pH for pristine and PEI-treated CNTs is shown in Fig.2. The pristine CNT has a low isoelectric point (pH $_{IEP}$) at 4.9, whereas the pH_{IEP} moves to a more basic value at 8.1 after treated by PEI. This result indicates that the cationic PEI polymer chains are noncovalently attached onto the CNT surface. PEI are reported to form PEI-metal ion complexes with several metal compound such as K_2PdCl_4, K_2PtCl_4 [18], $AgNO_3$ [27], $CuCl_2$ [28], etc. Hence, it is hypothesized that the positively charged amine groups of PEI could act as the anchor sites for the $PtCl_4^{2-}$

anions and followed by the electrostatic attraction of Ru^{3+} cations. In-situ reduction of these noble metal precursors will facilitate the uniform dispersion of PtRu NPs on MWCNTs.

3.2. FTIR spectra analysis of PEI-functionalized MWCNTs

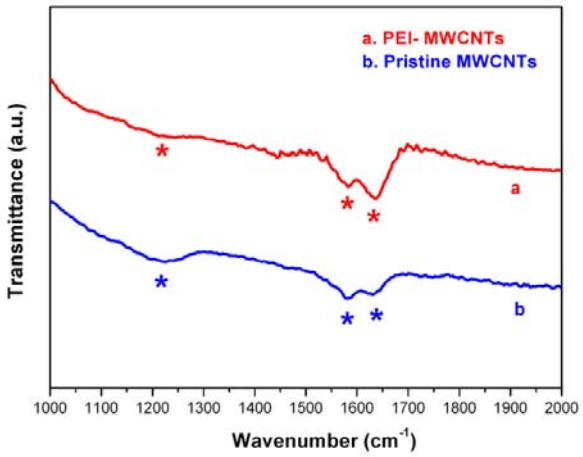

Fig.3. FTIR spectra of pristine MWCNTs and PEI-coated MWCNTs.

The FTIR spectra of pristine MWCNTs and PEI-MWCNTs are shown in Fig. 3. Three weak peaks at 1225 cm^{-1}, 1578 cm^{-1} and 1630 cm^{-1} (marked by blue asterisks) reveal the graphite structure of pristine MWCNTs [29]. By comparison, one sharper adsorption peak at 1637 cm^{-1} (marked by red asterisks) is identified on the spectrum of PEI-MWCNTs, which can be assigned to the bending vibration of N-H [26, 29, 30]. These results verify the successful noncovalent modification of MWCNTs with PEI.

3.3. Morphology of PtRu NPs decorated on PEI-MWCNTs and O-MWCNTs

(a)

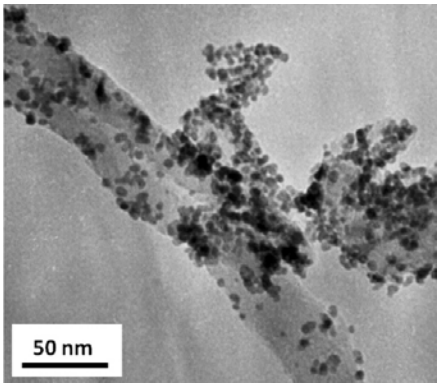
50 nm

(b)

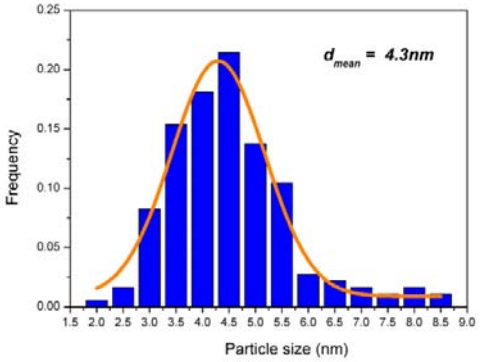
d_{mean} = 4.3nm
Frequency
Particle size (nm)

(c)

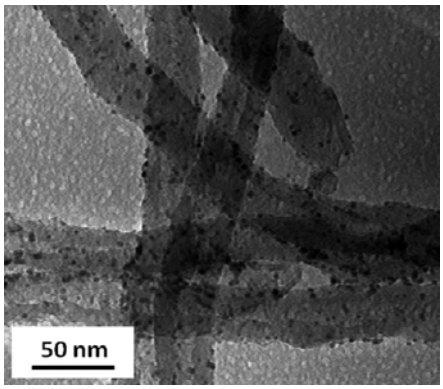
50 nm

(d)

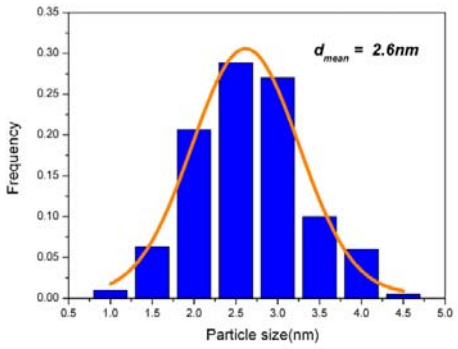
d_{mean} = 2.6nm
Frequency
Particle size(nm)

(e)

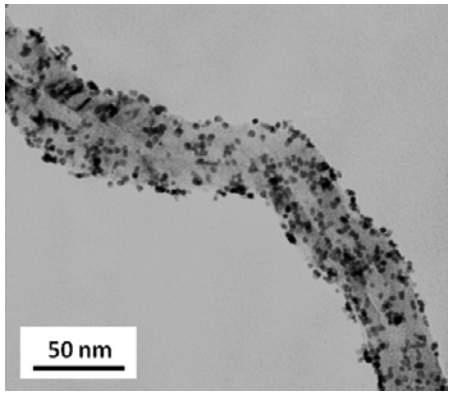
50 nm

(f)

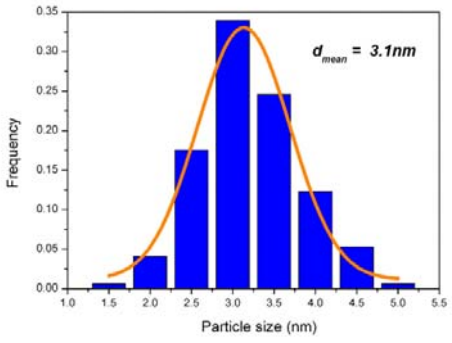
d_{mean} = 3.1nm
Frequency
Particle size (nm)

(g) (h)

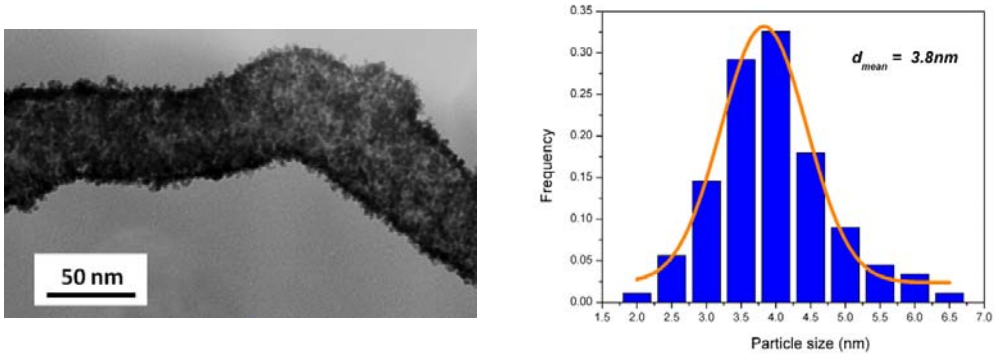

Fig.4. TEM images and the corresponding PtRu particle size distribution histograms of (a, b)30wt% PtRu/O-MWCNTs, (c, d)10wt% PtRu/PEI-MWCNTs, (e, f)30wt% PtRu/PEI-MWCNTs and (g, h)50wt% PtRu/PEI-MWCNTs.

Fig. 4 shows the representative TEM micrographs and the corresponding particle size distribution histograms of the as-prepared electrocatalysts. In the case of 30wt% PtRu/O-MWCNTs (Fig. 4a), the PtRu NPs are mainly distributed in the range of 2 to 8nm and the mean particle size is estimated to be 4.3 nm using Gaussian fit (Fig. 4b). Poor dispersion and obvious aggregation of PtRu nanocrystals on O-MWCNTs is observed, which is consistent with previous reports [11, 31, 32]. The formation of the agglomeration can be elucidated by the strong tendency of PtRu NPs to nucleate on the localized defect sites introduced by the harsh oxidation process. By contrast, PtRu NPs are homogeneously deposited on the external walls of PEI modified MWCNTs (Fig. 4c, Fig. 4e). The mean PtRu particle size is 2.6nm and 3.1nm for the PtRu/PEI-MWCNTs with 10wt% and 30wt% PtRu loading (Fig. 4d, Fig. 4f). The relatively small particle size and narrow size distribution is probably attributed to the presence of PEI coating, providing abundant adsorption sites for PtRu precursors, thereby realizing the uniform assembly of metal NPs. Moreover, PEI may also serve as an effective stabilizer to isolate the adjacent noble metal nanocrystals from coalescence [15, 33]. With the further increase of PtRu loading to 50wt%, PtRu NPs studded nanosheath structure is obtained (Fig. 4g). Even though the PtRu nanoclusters are almost completely interconnected with each other, the homogeneous coverage is

still maintained on PEI-MWCNTs.

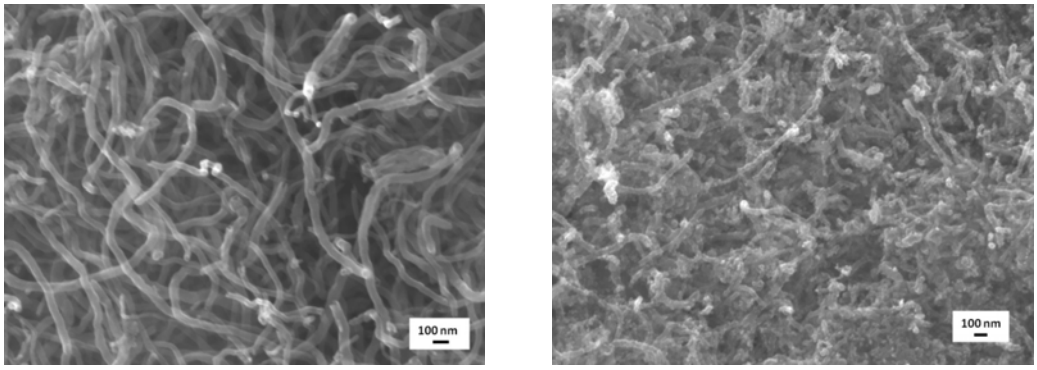

(a) (b)

Fig.5. SEM images of (a) pristine MWCNTs (b) 30wt% PtRu/PEI-MWCNTs.

As shown in the SEM images (Fig. 5b), PtRu NPs are evenly immobilized on PEI-MWCNTs. According to EDX analysis (Fig. 6), the atomic ratio of Pt to Ru is almost 1:1, while the total PtRu loading is approximate to 30wt%, which is close to the initial feed ratio. For the sample with 10wt% and 50wt% PtRu loading, we also obtain very consistent results. It is evident that the noble metal loading can be readily controlled by altering the concentration of the precursors.

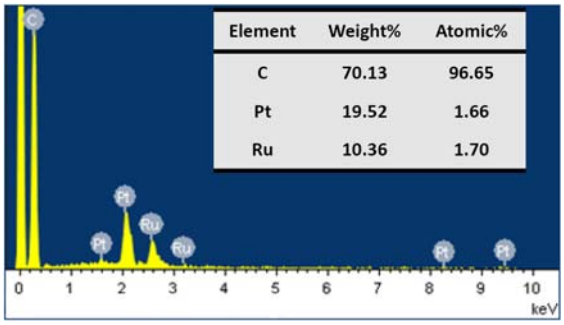

Fig.6. EDX spectrum of 30wt% PtRu/PEI-MWCNTs.

3.4. X-ray diffraction patterns of PtRu/MWCNTs nanocomposites

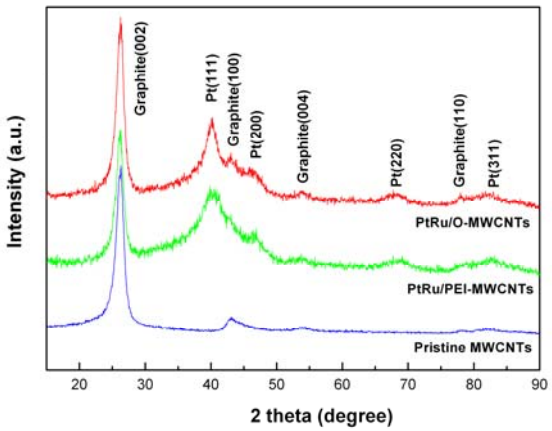

Fig.7. XRD patterns of pristine MWCNTs, 30wt% PtRu/PEI-MWCNTs and 30wt% PtRu/O-MWCNTs.

The X-ray diffractograms of pristine MWCNTs, PtRu/PEI-MWCNTs and PtRu/O-MWCNTs nanocomposites are shown in Fig. 7. The diffraction peaks at around 26.3°, 43.0°, 54.3°, 79.8° corresponds to (002), (100), (004), and (110) of the graphite structures of MWCNTs. The diffraction peaks for PtRu/O-MWCNTs at around 40.5°, 47.5°, 68.7°, 81.8° can be indexed to (111), (200), (220), and (311) crystalline planes of (face-centered cubic) f.c.c Pt, which shifted to high angle value with respect of pure f.c.c Pt (PDF card 4-802). This trend of peak displacements is also found for the PtRu/PEI-MWCNTs electrocatalyst with different PtRu loading, which implies the formation of PtRu alloy resulting from the incorporation of smaller Ru atoms into Pt phase [34, 35]. According to the Scherer equation:

$$d = \frac{0.9\lambda_{K\alpha}}{B_{2\theta}.Cos\theta} \qquad (1)$$

where d is the average particle size of PtRu NPs(nm), $\lambda_{K\alpha}$ is wavelength of X-Ray ($\lambda_{K\alpha}$= 0.15406nm), θ is the peak angle, and $B_{2\theta}$ is the full width half maximum in radians, the mean PtRu particle sizes are estimated to be 2.9, and 4.0 nm for 30wt% PtRu/PEI-MWCNTs and 30wt% PtRu/O-MWCNTs using the broadening of isolated (220) peak [36]. These results are in good agreement with TEM observations.

3.5. The electrochemical surface area of the nanocomposite electrocatalyst

The hydrogen electrosorption voltammograms for 30wt% PtRu/PEI-MWCNTs and 30wt% PtRu/O-MWCNTs electrocatalysts are shown in Fig. 8. The characteristic peak in the region of -0.2V to 0.1V can be attributed to atomic hydrogen adsorption on the Pt surface. And the ECSA for the catalysts can be estimated by the following equation:

$$ECSA = \frac{Q}{q^0 \times M_{Pt}} \tag{2}$$

where Q is the integrated area of the hydrogen desorption (μC), q^0 is the charge for monolayer hydrogen adsorption on Pt, q^0=210μC·cm^{-2}, a value generally admitted for polycrystalline Pt electrodes [37], M_{Pt} is the mass of the Pt loading.

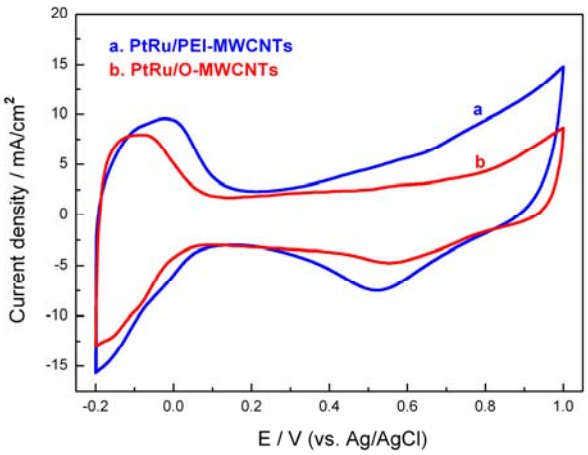

Fig.8. Cyclic voltammograms of PtRu (30wt% loading) supported on PEI-MWCNTs and O-MWCNTs in 0.5M H_2SO_4 at a scan rate of 50mV/s.

It is found that the PtRu/PEI-MWCNTs catalyst exhibit large ECSA around 81.7 m^2/g_{Pt} compared with 60.9 m^2/g_{Pt} for PtRu/O-MWCNTs. The larger ECSA of PtRu/PEI-MWCNTs implies more catalyst sites are accessible for electrochemical reactions, which can be attributed to the small particle size and high dispersion of PtRu NPs. Furthermore, it may also suggest that PEI coating on MWCNTs effectively prevent the PtRu nanoclusters from agglomeration and thus promote the electrocatalytic activity [15].

Since the ECSA alone cannot exactly represent the utilization efficiency of the

noble metal, it is also necessary to investigate how many surface atoms are contributing to the electrochemical reactions. Thus, the ratio of ECSA to the geometrical specific surface areas (S_{geom}) can be considered as an important indicator to evaluate the Pt utilization efficiency [38-39]. Here, the S_{geom} can be calculated by

$$S_{geom} = \frac{6000}{\rho d} \tag{3}$$

$$\rho_{PtRu} = X_{Pt}\rho_{Pt} + X_{Ru}\rho_{Ru} \tag{4}$$

where d (nm) is the mean particle diameter, ρ (g/cm^3) is the density of NPs, X is the weight fraction of metal, ρ_{Pt} = 21.4 g/cm^3, ρ_{Ru} = 12.3 g/cm^3 [38, 40].

For 30 wt% PtRu/O-MWCNTs, the S_{geom} and the utilization ratio is estimated to be 76.3 m^2/g and 79.8%, respectively. It is interesting to find that the S_{geom} is 105.8 m^2/g and the resulting utilization ratio is 77.2% for 30 wt% PtRu /PEI-MWCNTs. The similar utilization efficiency for both catalysts suggests that the methanol accessibility to the active sites of PtRu electrocatalyst will not be impeded by PEI coating on MWCNTs.

3.6. Electrocatalytic activity of PtRu/MWCNTs towards methanol oxidation

Fig. 9 illustrates the CV profiles of the electrocatalysts in 1M CH_3OH + 0.5 M H_2SO_4. In the forward sweep, the featured methanol oxidation peaks are observed at approximately 0.70V for 30wt% PtRu/PEI-MWCNTs and 30wt% PtRu/O-MWCNTs. In the reverse scan, the anodic peak at 0.47V is mainly associated with the removal of the residue carbonaceous species [41]. In principle, the onset potential of methanol oxidation is related to the breaking of C-H bonds and the subsequent removal of intermediates such as CO_{ads} by oxidation with OH_{ads} species supplied by Ru–OH sites [6, 42]. Hence, compared with 30wt% PtRu/O-MWCNTs, the relatively lower onset potential of methanol electrooxidation (MEO) indicates the MEO becomes more energetically favorable on the PtRu/PEI-MWCNTs nanocomposite.

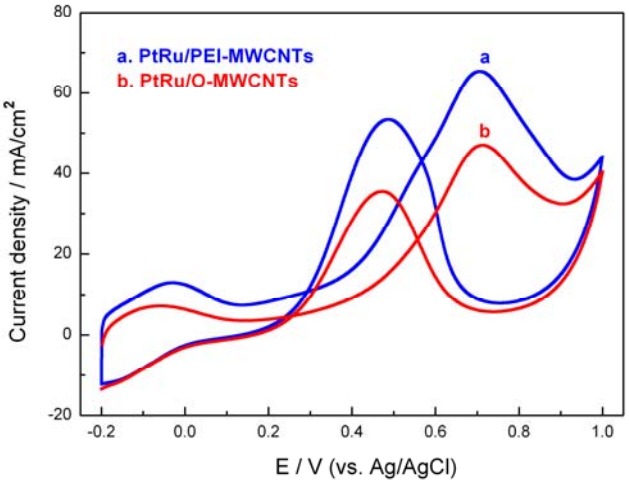

Fig.9. Cyclic voltammograms of PtRu (30wt% loading) supported on PEI-MWCNTs and O-MWCNTs in 0.5M H_2SO_4 + 1M CH_3OH at a scan rate of 50mV/s.

In addition, it is also worthwhile to note that the peak current density during the forward scan is 65.4mA/cm^2 for PtRu/PEI-MWCNTs, almost 1.4 times as large as that of PtRu/O-MWCNTs. The significant improvement in the catalytic activity for MEO is mostly likely due to the high ECSA of the former catalyst.

4. Conclusions

In summary, we presented an efficient and novel method to tether PtRu bimetallic NPs on the surface of PEI-modified MWNTs. Compared with the conventional acid-oxidization procedure, noncovalent functionalization of MWCNTs with PEI preserved the integrity of graphite structure and favored the uniform dispersion of PtRu NPs. The CV characterizations demonstrated that PtRu/PEI-MWCNTs nanocomposite exhibited superior electrocatalytic performance, which might be a promising anode catalyst for DMFCs.

References

[1] M.S. Saha, R. Li, X. Sun, J. Power Sources 177 (2008) 314.

[2] Y.J. Gu, W.T. Wong, Langmuir 22 (2006) 11447.

[3] N. Rajalakshmi, H. Ryu, M.M. Shaijumon, S. Ramaprabhu, J. Power Sources

140 (2005) 250.

[4] C.C. Chen, C.F. Chen, C.M. Chen, F.T. Chuang, Electrochem. Commun. 9 (2007) 159.

[5] Y. Wang, X. Xu, Z. Tian, Y. Zong, H. Cheng, C. Lin, Chem. Eur. J. 12 (2006) 2542.

[6] Y. Zhao, X. Yang, J. Tian, F. Wang, L. Zhan, J. Power Sources 195 (2010) 4634.

[7] G. Wei, C. Pan, J. Reichert, K.D. Jandt, Carbon 48 (2010) 645.

[8] X. Li, Y. Liu, L. Fu, L. Cao, D. Wei, Y. Wang, Adv. Funct. Mater 16 (2006) 2431.

[9] Y. Mu, H. Liang, J. Hu, L. Jiang, L. Wan, J. Phys. Chem. B 109 (2005) 22212.

[10] N. Du, H. Zhang, P. Wu, J. Yu, D. Yang, J. Phys. Chem. C 113 (2009) 17387.

[11] S. Wang, S.P. Jiang, X. Wang, Nanotechnology 19 (2008) 265601.

[12] A. Kongkanand, K. Vinodgopal, S. Kuwabata, P.V. Kamat, J. Phys. Chem. B 110 (2006) 16185.

[13] W. Yang, X. Wang, F. Yang, C. Yang, X. Yang, Adv. Mater. 20 (2008) 2579.

[14] X. Su, S. Dong, E. Wang, Polymer 45 (2004) 2181.

[15] L. Bai, H. Zhu, J.S. Thrasher, S.C. Street, ACS Appl. Mater. Interfaces 1 (2009) 2304.

[16] X. Hu, T. Wang, X. Qu, S. Dong, J. Phys. Chem. B 110 (2006) 853.

[17] X. Hu, T. Wang, L. Wang, S. Guo, S. Dong, Langmuir 23 (2007) 6352.

[18] J. Li, W. Yang, H. Zhu, X. Wang, F. Yang, B. Zhang, X. Yang, Talanta 79 (2009) 935.

[19] C. Bock, C. Paquet, M. Couillard, G.A. Botton, B.R. MacDougall, J. Am. Chem. Soc. 126 (2004) 8028.

[20] C. Bock, M.A. Blakely, B. MacDougall, Electrochim. Acta 50 (2005) 2401.

[21] M.K. Jeon, P.J. McGinn, J. Power Sources 188 (2009) 427.

[22] H.A. Gasteiger, N. Markovic, P. N. Ross Jr., E.J. Cairns, J. Phys. Chem. 97 (1993) 12020.

[23] T. Iwasita, F.C. Nart, W. Vielstich, Ber. Bunsen-Ges. Phys. Chem. 94 (1990) 1030.

[24] W. Li, C. Liang, W. Zhou, J. Qiu, Z. Zhou, G. Sun, Q. Xin, J. Phys. Chem. B 107 (2003) 6292.

[25] V. Lordi, N. Yao, J. Wei, Chem. Mater. 13 (2001) 733.

[26] L. Jiang, L. Gao, Carbon 41 (2003) 2923.

[27] J. Dai, M.L. Bruening, Nano lett. 2 (2002) 497.

[28] H.X. Wu, W.M. Cao, Y. Li, G. Liu, Y. Wen, H.F. Yang, S.P. Yang, Electrochim. Acta 55 (2010) 3734.

[29] G. Zou, H. Yang, M. Jain, H. Zhou, D. Williams, M. Zhou, T. McCleskey, A. Burrell, Q. Jia, Carbon 47 (2009) 933.

[30] N. Jia, Q. Lian, H. Shen, C. Wang, X. Li, Z. Yang, Nano lett. 7 (2007) 2976.

[31] S. Wang, X. Wang, S.P. Jiang, Langmuir 24 (2008) 10505.

[32] S. Guo, S. Dong, E. Wang, Adv. Mater. 21 (2009) 1.

[33] T. Li, Y. Du, E. Wang, Chem. Asian J. 3 (2008) 1942.

[34] E. Antolini, F. Cardellini, J. Alloys Compd. 315 (2001) 118.

[35] J. Guo, G. Sun, S. Sun, S. Yan, W. Yang, J. Qi, Y. Yan, Q. Xin, J. Power Sources 168 (2007) 299.

[36] G. Wu, B.Q. Xu, J. Power Sources 174 (2007) 148.

[37] R. Woods, J. Electroanal. Chem. 9 (1976) 1.

[38] C. Zhou, H. Wang, F. Peng, J. Liang, H. Yu, J. Yang, Langmuir 25 (2009) 7711.

[39] T. Thampan, S. Malhotra, J. Zhang, R. Datta, Catal. Today 67 (2001) 15.

[40] Z.B. Wang, G.P. Yin, J. Zhang, Y.C. Sun, P.F. Shi, Electrochim. Acta 51 (2006) 5691.

[41] A. Halder, S. Sharma, M.S. Hegde, N. Ravishankar, J. Phys. Chem. C 113 (2009) 1466.

[42] R. Chetty, S. Kundu, W. Xia, M. Bron, W. Schuhmann, V. Chirila, W. Brandl, T. Reinecke, M. Muhler, Electrochim. Acta 54 (2009) 4208.

Paper #2

An effective approach towards the immobilization of PtSn nanoparticles on noncovalent modified MWCNTs for ethanol electrooxidation

(submitted to *Electrochimica Acta*)

Abstract

In this article, we describe an effective method to tether Pt and PtSn nanoparticles on polyelectrolyte modified multi-walled carbon nanotubes (MWCNTs). By using a polymer wrapping technique, the positively charged polyethyleneimine (PEI) was attached onto CNTs for the purpose of providing preferential linking sites for metal precursors. Well-dispersed Pt and PtSn nanocrystals (2-5nm) were subsequently decorated on PEI-functionalized MWCNTs through the polyol reduction method. The successful non-covalent modification of MWCNTs was confirmed by FTIR and Zeta potential measurements. Characteristic peaks for Pt and Sn were observed on EDX spectrum, indicating c.a. 20wt% Pt loading and a desirable Pt:Sn atomic ratio of 1:1. Electrochemical analysis demonstrated that the as-synthesized PtSn/PEI-MWCNTs nanocomposite exhibited superior catalytic activity and higher poison tolerance for ethanol oxidation as compared to Pt/PEI-MWCNTs and commercial Pt/Vulcan XC-72 catalysts. The enhanced electrochemical performance can be attributed to the uniform dispersion of nanoparticles as well as the promoting effect of the Sn element. This modification and synthetic strategy could be further extended to develop a diversity of carbon supported Pt-based hybrid materials for the application of electrocatalysis.

Keywords: PEI; PtSn NPs; MWCNTs; Ethanol Oxidation

1. Introduction

Direct ethanol fuel cells (DEFCs) are attracting enormous research interest as an alternative power source for vehicles and portable electronic devices, due to its easy storage, high energy density, low toxicity and availability from biomass [1-3]. To date, carbon supported platinum is the most commonly used electrocatalyst for ethanol oxidation. However, the high cost and scarcity of Pt still hinder the commercialization of DEFCs [3]. It is well recognized that the catalytic activity and stability of the electrocatalyst is strongly dependant on its particle size and dispersion state of the noble metal on the carbon support. In the pursuit of improved Pt utilization, a variety of nanostructured carbon materials including carbon nano tubes (CNTs) [3-7], carbon nano fibers (CNFs) [8], carbon aero gel [9] and mesoporous carbon [10] have been extensively investigated as potential catalyst supports.

Among these novel carbon materials, CNTs have intriguing features such as large active surface area, excellent electronic conductivity and high chemical stability, hence they are considered to be one of the most promising candidates as Pt nanoparticles (NPs) support [4-7]. Since the pristine CNTs are chemically inert and hydrophobia, much research work has been dedicated to modify their surface in order to create better dispersion of Pt NPs. Recently, functionalization of CNTs through non-covalent attachment of polyelectrolyte has been developed to regulate the growth of Pt NPs with well-defined shape and tunable size. As a versatile strategy, polyelectrolyte modification not only preserves the intrinsic structure of CNTs, but also achieves the tailored properties of the nanocomposites [11]. For example, highly-dispersed Pt NPs were deposited on the sidewalls of positively charged poly (diallyldimethylammonium chloride) coated CNTs with high density [12, 13]. In addition, the amino-rich cationic Polyethyleneimine (PEI) has also been explored to be adsorbed on the CNTs for the size-controlled synthesis of Pt NPs [14, 15].

Apart from the high cost issue, the other major challenge that DEFCs faces so far, is the self-poisoning of Pt by intermediate species like CO. Previous research work on bimetallic catalyst system demonstrated that the incorporation of second metal, Sn in particular, could significantly mitigate the CO poisoning effect [16-18]. In several

related studies, carbon supported PtSn with different Sn content has also been prepared and investigated for ethanol electrooxidation. Zhou et al. found the catalytic performance of PtSn/C could be optimized by tuning the Pt:Sn molar ratio in a range from 1:1 to 2:1 [19, 20], which is similar to the results demonstrated by Spinacé and coworkers [21].

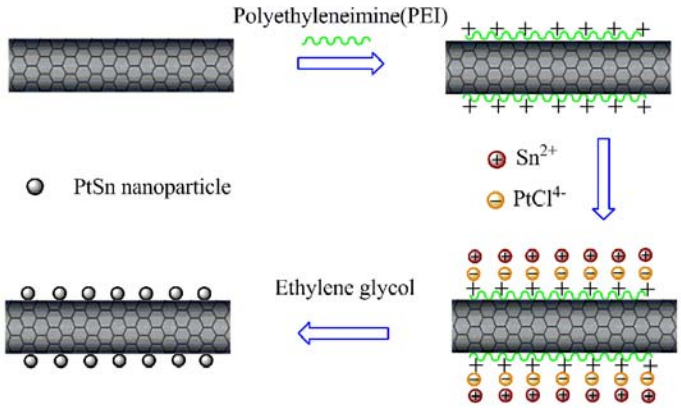

Fig.1. Schematic illustration showing the synthesis of PtSn electrocatalyst supported on PEI-functionalized MWCNTs.

With the goal of designing high-performance catalyst with enhanced Pt utilization as well as good CO tolerance, here we presented a facile and efficient synthetic route to anchor bimetallic PtSn electrocatalyst on PEI functionalized CNTs. Fig.1 illustrates the scheme of the noncovalent surface modification of MWCNTs and the subsequent immobilization of PtSn NPs. According to TEM and SEM observation, Pt and bimetallic PtSn nanocrystals were uniformly decorated on PEI-functionalized MWCNTs. The composition, crystalline structure and electrochemical properties of the hybrid materials were investigated by EDX, XRD, cyclic voltammetry and chronoamperometry.

2. Experimental

2.1. Materials

Multi-walled carbon nanotubes (MWCNTs, 95% purity, diameter=30nm-60nm) were obtained from Helix Material Solutions, Inc. Potassium tetrachloroplatinate (K_2PtCl_4, 98%), tin(II) chloride dihydrate ($SnCl_2{\cdot}2H_2O$, 98%), Nafion solution (5wt%

in ethanol), ethylene glycol (EG, 99%), and ethanol (99%) were purchased from Sigma-Aldrich. polyethyleneimine (PEI 50wt% in water, Mw=60,000), sulfuric acid (98wt%) were obtained from Alfa Aesar. Pt/Vulcan XC-72 electrocatalyst with 20wt% metal loading was purchased from E-TEK. All the chemicals were used as received without further purification. Ultrapure Milli-Q water (resistivity>18.2 MΩ cm) was exclusively used for making aqueous solutions and rinsing procedures.

2.2. Functionalization of MWCNTs with PEI

Non-covalent functionalization of MWCNTs by PEI was carried out through a procedure modified from a prior publication [14]. Briefly, 100mg of MWCNTs was dispersed into 200ml 1wt% PEI aqueous solution, followed by ultrasonication for 3h and magnetic stirring for 12h. The PEI-MWCNTs suspension was then filtered and rinsed to remove the excess PEI.

2.3. Synthesis of PEI-MWCNTs supported Pt and PtSn electrocatalysts

PtSn/PEI–MWCNTs nanocomposites were prepared by using a polyol reduction method described as follows: 100 mg PEI-CNTs was first suspended in an EG solution in an ultrasonic bath. An EG solution of K_2PtCl_4 and $SnCl_2$ with a atomic ratio of Pt:Sn=1:1 was added dropwise under vigorous agitation to achieve the nominal Pt loading of 20wt%. The metal precursors were completely reduced by refluxing the mixture at elevated temperature up to 140°C for 3h. And a flow of ultra-high purity nitrogen was introduced to the reaction system to isolate oxygen and to remove the organic byproducts. After centrifugation, washing, and drying at 70°C overnight, the PtSn/PEI-MWCNTs catalyst was obtained. For comparison purpose, the Pt/PEI-MWCNTs nanocomposite was also prepared in a similar manner, but in the absence of $SnCl_2$.

2.4 Physiochemical characterization

Zeta potential measurements were performed on a Marvern Zetasizer Nano ZS90. FTIR spectra were acquired using Brukeroptics Vetex70 spectrometer to further

confirm the functionalization of MWCNTs by PEI. The morphology of the PtRu/MWCNTs nanocomposite was studied by a JEOL 7000F scanning electron microscope (SEM) and JEOL 100CX transmission electron microscope (TEM). The average composition of the nanocomposites was evaluated using energy dispersive X-ray analysis (EDX). The X-ray diffraction (XRD) patterns of the samples were recorded using a Rigaku Geigerflex X-ray diffractometer with Cu Kα radiation.

2.5. Electrochemical analysis

Electrochemical measurements were carried out on a BASi 100B electrochemical analyzer using conventional three-electrode cell. A glassy carbon electrode (GCE) (3mm in diameter) was used as the working electrode, on which a thin layer of Nafion-impregnated catalyst with a fixed loading of 2mg/cm^2 was applied. A platinum wire served as the counter electrode and a Ag/AgCl electrode was used as the reference electrode. The electrochemical active surface area (ECSA) was calculated from the hydrogen desorption region of the voltammetric curve in 0.5M H_2SO_4 solution. The electrocatalytic activity for ethanol oxidation was characterized by cyclic voltammetry (CV) in 0.5M H_2SO_4 solution containing 1M C_2H_5OH. In order to evaluate the stability of the catalysts, chronoamperograms were also recorded at 0.6V for 600s. The electrolyte solution was deaerated with ultra high purity N_2 prior to the measurement and all the experiment was conducted at room temperature.

3. Results and discussion

3.1 Zeta potential measurement of PEI-MWCNTs nanocomposite

Zeta potentials as a function of pH for pristine and PEI-coated MWCNTs are presented in Fig.2. The sample of pristine MWCNTs is found to have a low initial isoelectric point (pH $_{IEP}$) at 4.9. After treated with PEI, the pH_{IEP} positively shift to a more basic value at 8.1, indicating that the cationic PEI polymer chains are noncovalently attached onto the MWCNTs [22]. Since PEI has been widely reported to form complexes with various metal compound, such as K_2PdCl_4, K_2PtCl_4[14], $AgNO_3$ [23], and $CuCl_2$[24], it is assumed that the positively charged amine groups of

PEI may act as anchor sites for the negatively charged $PtCl_4^{2-}$ anions and followed by the electrostatic attraction of Sn^{2+} cations. In-situ reduction of these metal precursors will favor the uniform assembly of Pt-based NPs on the surface of the PEI modified MWCNTs.

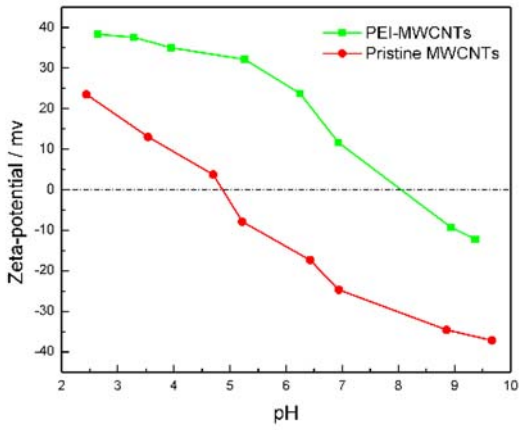

Fig.2. Zeta potential as a function of pH for pristine MWCNTs and PEI-MWCNTs

3.2 FTIR spectra of PEI-functionalized MWCNTs

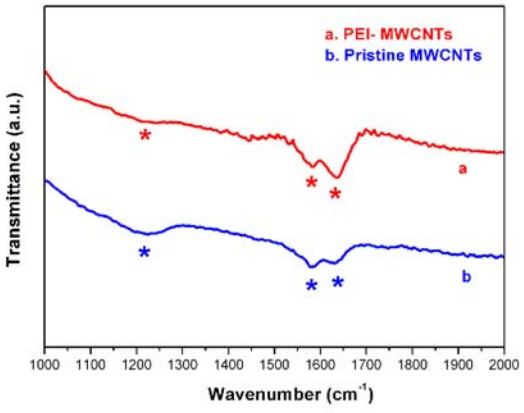

Fig.3. FTIR spectra of pristine MWCNTs and PEI-MWCNTs.

The FTIR spectra of pristine MWCNTs and PEI-MWCNTs are shown in Fig. 3. Three weak peaks at 1225 cm^{-1}, 1578 cm^{-1} and 1630 cm^{-1} (marked by blue asterisks) reveal the graphite structure of pristine MWCNTs [25]. By comparison, one relatively sharp adsorption peak at 1637 cm^{-1} (marked by red asterisks) is identified on the

spectrum of PEI-MWCNTs, which can be assigned to the bending vibration of N-H [22, 25, 26]. These results verify the successful noncovalent modification of MWCNTs with PEI.

3.3 Morphology and composition of the as-prepared catalysts

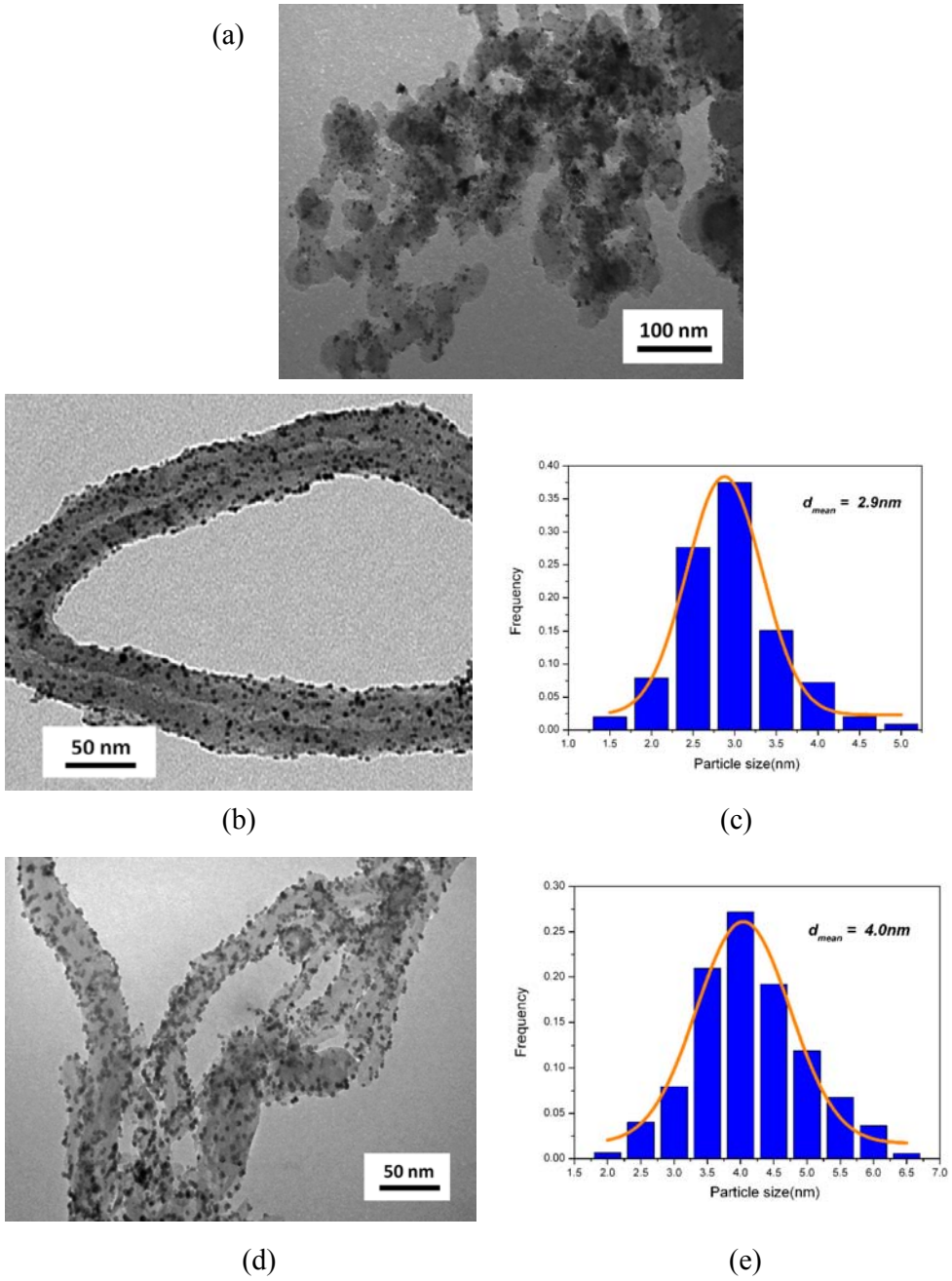

Fig.4. TEM images and the corresponding particle size distribution of (a) Pt/XC-72 (b, c) Pt/PEI-MWCNTs (d, e) PtSn/PEI-MWCNTs.

TEM images and particle size distribution histograms of various electrocatalysts are shown in Fig.4. In the case of Pt/PEI-MWCNTs and PtSn/PEI-MWCNTs nanocomposites, Pt and bimetallic PtSn NPs are homogeneously deposited on the external walls of PEI-MWCNTs (Fig.4b, 4d). The mean particle size is estimated to be 2.9 nm for the former and 4.0 nm for the latter using the Gaussian fit (Fig. 4c, 4e). The relatively small particle size and narrow size distribution is probably attributed to the presence of PEI coating on MWCNTs. These positively charged PEI molecules provide abundant adsorption sites for metal precursors and may also serve as a stabilizing reagent to isolate the adjacent nanocrystals from agglomeration [27, 28].

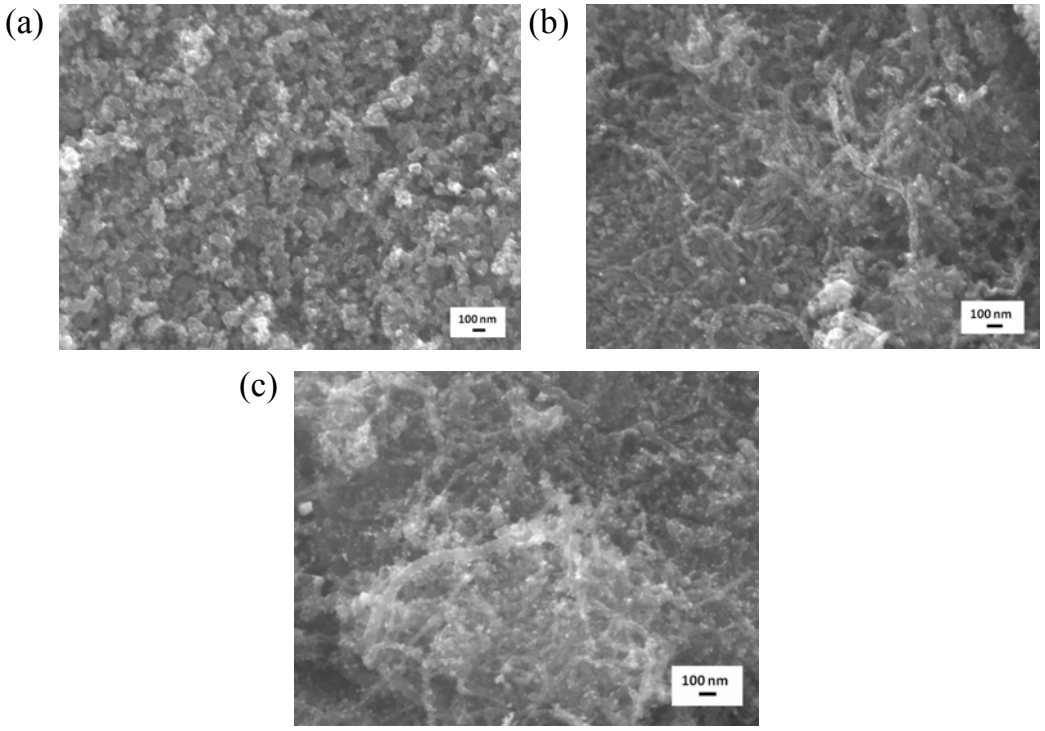

Fig.5. SEM images of (a) Pt/XC-72 (b) Pt/PEI-MWCNTs and (c) PtSn/PEI-MWCNTs

As depicted in Fig.5, the uniform coverage of Pt and PtSn NPs on PEI-MWCNTs are clearly shown through SEM observation. According to EDX analysis (Fig. 6a,), 20.3wt% and 21.4% Pt loading was obtained for Pt/PEI-MWCNTs and PtSn/PEI-MWCNTs, respectively. The average composition of PtSn/PEI-MWCNTs with a Pt:Sn atomic ratio of 46:54 is very close to the initial feeding ratio, implying that the metal precursors have been completely reduced and deposited on the surface of modified-MWCNTs.

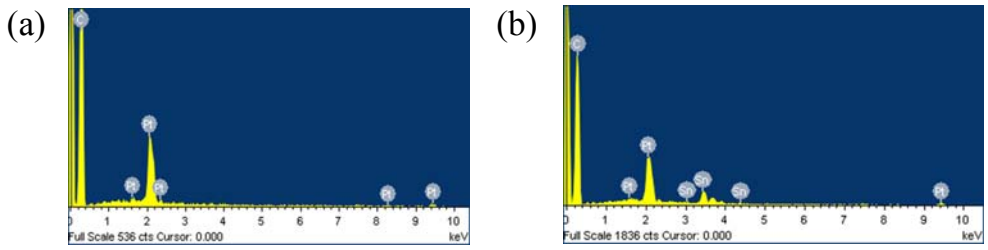

Fig.6. EDX spectra of (a) Pt/PEI-MWCNTs and (b) PtSn/PEI-MWCNTs.

3.4 XRD analysis

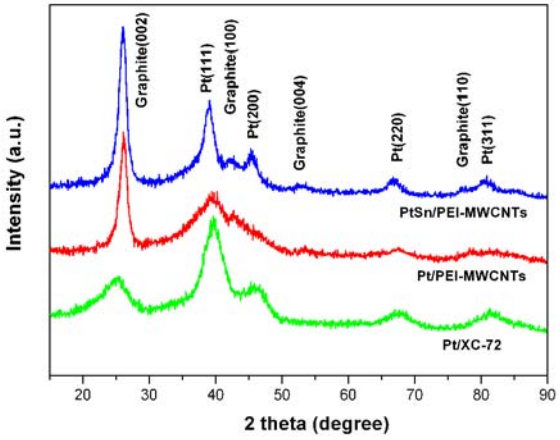

Fig.7. X-ray diffraction patterns of Pt/XC-72, Pt/PEI-MWCNTs and PtSn/PEI-MWCNTs.

The X-ray diffractograms of various catalysts are shown in Fig 6. The diffraction peaks at 26.3°, 43.0°, 54.3°, 79.8° corresponds to (002), (100), (004), and (110) of the graphite structures of MWCNTs and the peaks at around 40°, 47°, 68°, 81° can be indexed to (111), (200), (220), and (311) crystalline planes of Pt fcc structure for all the XRD patterns[29]. It is noted that the Pt diffraction peaks for PtSn/PEI-MWCNTs slightly shifted to lower 2θ angle values with respect to pure Pt (PDF card 4-802). This shift in peak indicates the formation of PtSn alloy, which is caused by the incorporation of Sn in fcc Pt phase [30, 31]. The average size of Pt and PtSn NPs can be calculated using Scherrer equation:

$$d = \frac{0.9\lambda_{K\alpha}}{B_{2\theta}.Cos\theta} \qquad (1)$$

where d is the average particle size (nm), $\lambda_{K\alpha}$ is wavelength of X-Ray ($\lambda_{K\alpha}$= 0.15406nm), θ is angle of Pt (220) peak, and $B_{2\theta}$ is the full width half maximum in radians[2, 30]. The mean particle size of Pt and PtSn NPs is estimated to be 3.1, 2.7, and 4.1 nm for Pt/XC-72, Pt/PEI-MWCNTs and PtSn/PEI-MWCNTs, respectively, which is consistent with TEM observation.

3.5 Electrochemical activity of the catalysts

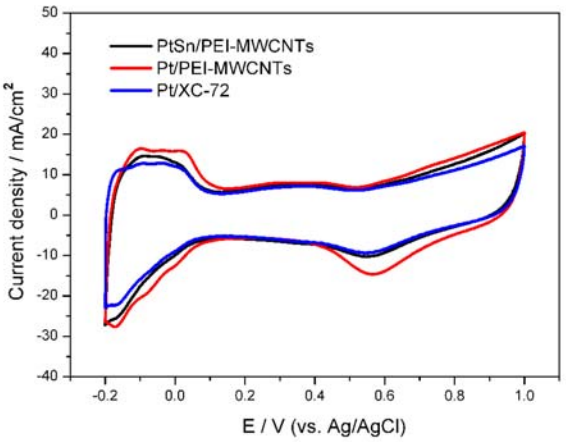

Fig.8. Cyclic voltammograms of Pt/XC72, Pt/PEI-MWCNTs and PtSn/PEI-MWCNTs catalysts in 0.5M H_2SO_4 at a scan rate of 50mV/s.

The hydrogen electrosorption voltammograms for various electrocatalysts are shown in Fig.8. The characteristic peak in the region of -0.2V to 0.1V is attributed to atomic hydrogen adsorption on the Pt surface and the ECSA for the catalysts can be estimated by the following equation:

$$ECSA = \frac{Q}{q^0 \times M_{Pt}} \tag{2}$$

where Q is the integrated area of the hydrogen desorption (μC), q^0 is the charge for monolayer hydrogen adsorption on Pt, q^0=210μC·cm^{-2}, a value generally admitted for polycrystalline Pt electrodes [32], M_{Pt} is the mass of the Pt loading. The Pt/PEI-MWCNTs catalyst exhibit the largest ECSA around 79.7 m^2/g_{Pt}, whereas the PtSn/PEI-MWCNTs has a slightly larger ECSA (64.8 m^2/g_{Pt}) than Pt/XC-72 (56.2 m^2/g_{Pt}). These results reveal that non-covalent modification of MWCNTs with PEI

facilitate the high dispersion of metal NPs and thus improve the electrochemical performance.

Fig.9 illustrates the CV profiles of ethanol oxidation on various electrocatalysts in 1M C_2H_5OH + 0.5 M H_2SO_4. In the forward sweep, the ethanol oxidation reaction (EOR) starts at 0.43V, 0.45V and 0.35V for Pt/XC-72, Pt/PEI-MWCNTs and PtSn/PEI-MWCNTs, respectively. The lower onset potential indicates that EOR becomes more energetically favorable on PtSn/PEI-MWCNTs than on the other catalysts. It is also worthwhile to note that the forward peak current density (I_f) are in the order of PtSn/PEI-MWCNTs (95.8 mA/cm^2) > Pt/PEI-MWCNTs (71.4 mA/cm^2) > Pt/XC-72 (50.8 mA/cm^2). Compared with Pt/XC-72, the higher I_f of Pt/PEI-MWCNTs can be elucidated by the fact that more catalyst sites are accessible for electrochemical reactions owing to the larger ECSA. Yet it is evident that the PtSn/PEI-MWCNTs outperform Pt/PEI-MWCNTs for EOR with a slight lower ECSA. Hence, the significant enhancement in the catalysis of EOR on the former electrocatalyst can be interpreted in terms of the promoting effect of Sn [29, 32].

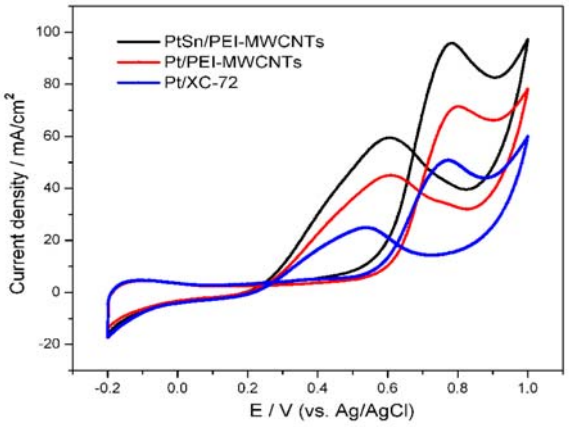

Fig.9. Cyclic voltammograms of Pt/Vulcan-XC72, Pt/PEI-MWCNTs and PtSn/PEI-MWCNTs catalysts in 0.5M H_2SO_4 + 1M C_2H_5OH at a scan rate of 50mV/s.

Fig.10 shows the current-time curves measured at a constant potential 0.6V in 1M C_2H_5OH + 0.5 M H_2SO_4. For all catalysts, the potential-static currents drop rapidly in the initial stage, and then reach a pseudosteady state after a period of c.a. 300s. The initial high current is associated with double-layer charging, while the current decay is

caused by the accumulation of poisonous carbonaceous intermediates on the electrode surface [33]. As seen in the chronoamperometric profile, PtSn/PEI-MWCNTs maintain the higher current density and lower current decay rate when compared with Pt/XC-72 and Pt/PEI-MWCNTs. The less pronounced current decline on PtSn/PEI-MWCNTs is indicative of its enhanced poisoning tolerance towards EOR. Based on the bifunctional mechanism, the second metal Sn activates water at lower potentials, which produces adsorbed oxygen-containing species to remove the adsorbed CO and therefore liberate Pt active site. In addition, the ligand effect may also occur to alter the electronic properties of Pt and in turn weaken the Pt-CO bond by introducing Sn element. [34, 35].

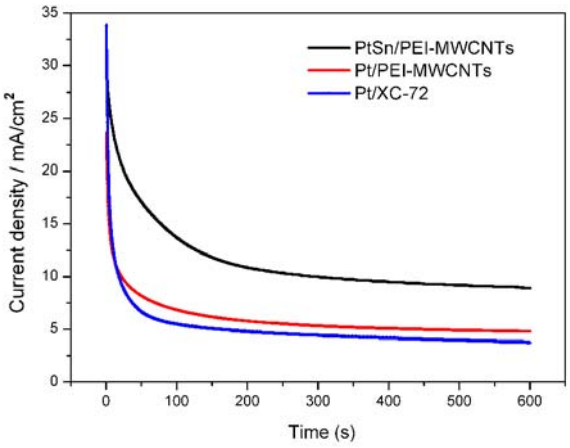

Fig.10. Chronoamperograms recorded at 0.6v vs Ag/AgCl for ethanol oxidation on Pt/Vulcan-XC72, Pt/PEI-MWCNTs and PtSn/PEI-MWCNTs catalysts in 0.5M H_2SO_4 + 1M C_2H_5OH.

4. Conclusions

In summary, small-sized Pt and bimetallic PtSn NPs were homogeneously decorated on noncovalent functionalized MWNTs via in-situ polyol reduction method. This polyelectrolyte modification strategy favored the high dispersion of metal NPs on CNTs, thereby can be extended for the assembly of a wealth of Pt-based hybrid materials. Electrochemical studies demonstrated that the as-synthesized

PtSn/PEI-MWCNTs nanocomposites displayed remarkable catalytic activity towards ethanol electrooxidation, suggesting its great potential for the application of direct ethanol fuel cell (DEFC).

Reference

[1] L. Cao, G. Sun, H. Li, Q. Xin, Electrochem. Commun. 9 (2007) 2541.

[2] D.R.M. Godoi, J. Perez, H.M. Villullas, J. Power Sources 195 (2010) 3394.

[3] H. Song, X. Qiu, F. Li, Appl. Catal. A: Gen. 364 (2009) 1.

[4] R.I. Jafri, S. Ramaprabhu, In. J. Hydrogen Energy 35 (2010) 1339.

[5] D.-J. Guo, X.-P. Qiu, L.-Q. Chen, W.-T. Zhu, Carbon 47(2009) 1680.

[6] G. Gao, G. Yang, M. Xu, C. Wang, C. Wang, C. Xu, H. Li, J. Power Sources 173 (2007) 178.

[7] H.L. Pang, J.P. Lu, J.H. Chen, C.T. Huang, B. Liu, X.H. Zhang, Electrochim. Acta 54 (2009) 2610.

[8] M. Tsuji, M. Kubokawa, R. Yano, N. Miyamae, T. Tsuji, M.-S. Jun, S. Hong, S. Lim, S.-H. Yoon, I. Mochida, Langmuir 23 (2007) 387.

[9] H. Du, B. Li, F. Kang, R. Fu, Y. Zeng, Carbon 45 (2007) 429.

[10] W.C. Choi, S.I. Woo, M.K. Jeon, J.M. Sohn, M.R. Kim, H.J. Jeon, Adv. Mater. 17 (2005) 446.

[11] X. Li, Y. Liu, L. Fu, L. Cao, D. Wei, Y. Wang, Adv. Funct. Mater 16 (2006) 2431.

[12] N. Du, H. Zhang, P. Wu, J. Yu, D. Yang, J. Phys. Chem. C 113 (2009) 17387.

[13] S. Wang, S.P. Jiang, X. Wang, Nanotechnology 19 (2008) 265601.

[14] J. Li, W. Yang, H. Zhu, X. Wang, F. Yang, B. Zhang, X. Yang, Talanta 79 (2009) 935.

[15] X. Hu, T. Wang, L. Wang, S. Guo, S. Dong, Langmuir 23 (2007) 6352.

[16] F.L.S. Purgato, P. Olivi, J.-M. Léger, A.R. de Andrade, G. Tremiliosi-Filho, E.R. Gonzalez, C. Lamy, K. B. Kokoh, J. Electroanal. Chem. 628 (2009) 81.

[17] H. Hitmi, E.M. Belgsir, J.-M. Léger, C. Lamy, R.O. lezna, Electrochim. Acta 39

(1994) 407.

[18] D.R.M. Godoi, J. Perez, H.M. Villullas, J. Power Sources 195 (2010) 3394.

[19] W.J. Zhou, S.Q. Song, W.Z. Li, Z.H. Zhou, G.Q. Sun, Q. Xin, S. Douvartzides, P. Tsiakaras, J. Power Sources 140 (2005) 50.

[20] W. Zhou, Z. Zhou, S. Song, W. Li, G. Sun, P. Tsiakaras, Q. Xin, Appl. Catal., B 46 (2003) 273

[21] E.V. Spinacé, M. Linardi, A.O. Neto, Electrochem. Commun. 7 (2005) 365.

[22] L. Jiang, L. Gao, Carbon 41 (2003) 2923.

[23] J. Dai, M.L. Bruening, Nano lett. 2 (2002) 497.

[24] H.X. Wu, W.M. Cao, Y. Li, G. Liu, Y. Wen, H.F. Yang, S.P. Yang, Electrochim. Acta 55 (2010) 3734.

[25] G. Zou, H. Yang, M. Jain, H. Zhou, D. Williams, M. Zhou, T. McCleskey, A. Burrell, Q. Jia, Carbon 47 (2009) 933.

[26] N. Jia, Q. Lian, H. Shen, C. Wang, X. Li, Z. Yang, Nano lett. 7 (2007) 2976.

[27] L. Bai, H. Zhu, J.S. Thrasher, S.C. Street, ACS Appl. Mater. Interfaces 1 (2009) 2304.

[28] T. Li, Y. Du, E. Wang, Chem. Asian J. 3 (2008) 1942.

[29] G. Li, P. G. Pickup, J. Power Sources 173 (2007) 121.

[30] E. Lee, I.-S. Park, A. Manthiram, J. Phys. Chem. C 114 (2010) 10634.

[31] W.J. Zhou, S.Q. Song, W.Z. Li, G.Q. Sun, Q. Xin, S. Kontou, K. Poulianitis, P. Tsiakaras, Solid State Ionics 175 (2004) 797.

[32] R. Woods, J. Electroanal. Chem. 9 (1976) 1.

[33] Z.-B. Wang, G.-P. Yin, J. Zhang, Y.-C. Sun, P.-F. Shi, J. Power Sources 160 (2006) 37.

[34] F. Delime, J.M. Leger, C.Lamy, J. Appl. Electrochem. 29 (1999) 1249.

[35] F. Vigier, C. Coutanceau, F. Hahn, E.M. Belgsir, C. Lamy, J. Electroanal. Chem. 563 (2004) 81.

CHAPTER V CONCLUSIONS AND FUTURE WORK

This study includes experimental investigations on the synthesis and characterization for nanostructured carbon supported Pt-based electrocatalysts. Based on the research results, the following conclusions have been drawn:

(i) Successful noncovalent modification of CNTs with cationic polyethyleneimine (PEI) was confirmed through Zeta potential measurements and FTIR spectrum analysis;

(ii) TEM and SEM observation verified the uniform dispersion of Pt, PtRu and PtSn on PEI-modified CNTs, which is probably due to the abundant anchoring sites provided by PEI as well as the stabilizing effect of PEI;

(iii) The loading and composition of the resulting products can be controlled to some extent by varying the experiment condition such as the precursor concentration;

(iv) Electrochemical investigation revealed that the as-prepared PtRu/PEI-CNTs exhibited large ECSA and excellent catalytic activity towards methanol oxidation when compared with PtRu supported on oxidized CNTs;

(v) Bimetallic PtSn/PEI-CNTs outperformed Pt/PEI-CNTs and commercial E-TEK Pt/C in terms of catalytic activity and stability for ethanol oxidation;

In summary, the proposed noncovalent surface functionalization as well as in-situ polyol reduction are proven to be efficient strategies for the fabrication of bimetallic Pt/C nanocomposite, and could be further extended to develop a broad range of nanostructured carbon supported Pt hybrid materials for enhanced electrocatalysis of small organic fuel molecules.

Potential future work may involve (i) comprehensive electrochemical study on the synthesized electrocatalyst based on polarization and CO-stripping technique; (ii) fabrication of hierarchal structural carbon supported electrocatalyst with large surface area and improved mass transfer property; (iii) exploration of Pt/SnO_2 hybrid as

alternative fuel cell catalysts with high corrosion resistance.

APPENDIX : ABBREVIATIONS

1-AP:	1-aminopyrene
ADT:	accelerated durability test
AE:	auxiliary electrode
CA:	chronoamperometry
CC:	carbon cloth
CNFs:	carbon nano fibers
CP:	carbon paper
CPE:	constant phase element
CV:	cyclic voltammetry
CVD:	chemical vapor deposition
DEFCs:	direct ethanol fuel cells
DMFCs:	direct methanol fuel cells
DWCNTs:	double-walled carbon nano tubes
EBD:	electron beam deposition
ECSA:	electrochemical surface area
EG:	ethylene glycol
EIS:	electrochemical impedance spectrum
GCE:	glassy carbon electrode
GDL:	gas diffusion layer
HOR:	hydrogen oxidation reaction
MEA:	membrane electrode assembly
MOR:	methanol oxidation reaction
NPs:	nanoparticles
OCV:	open circuit voltage
ORR:	oxygen reduction reaction
PDDA:	poly (diallyldimethylammonium chloride)

PEI:	polyethyleneimine
PEMFCs:	proton exchange membrane fuel cells
PLD:	pulsed laser deposition
PPh_3:	triphenylphosphine
PPy:	polypyrrole
PSS:	poly (sodium 4-styrenesulfonate)
PVD:	physical vapor deposition
PVP:	poly(N-vinyl-2-pyyrolidone)
RHE:	reversible hydrogen electrode
RE:	reference electrode
SWCNTs:	single-walled carbon nano tubes
SAED:	selected area electron diffraction
SDS:	sodium dodecyl sulfate
WE:	working electrode